Alloying a hard phase with a solid lubricant: an approach concept for hard, self-lubricating PVD coatings for tribological applications

Inauguraldissertation

zur
Erlangung der Würde eines Doktors der Philosophie

vorgelegt der
Philosophisch-Naturwissenschaftlichen Fakultät
der Universität Basel

von
Vladislav Spassov
aus Sofia (Bulgarien)

Neuchâtel, 2009

Genehmigt von der Philosophisch-Naturwissenschaftlichen Fakultät
auf Antrag von

Prof. Peter Oelhafen
Prof. Ernst Meyer

Neuchâtel, 30. 10. 2006

Dekan Prof. Hans-Peter Hauri

Abstract

Friction and wear are not desired for many applications. One way to diminish the wear of a component is to coat it by Physical Vapor Deposition (PVD) with a thin, wear resistant hard coating. This approach has proved very successful for the past decades. Although increasing the wear resistance and thus the lifetime of the coated components, almost all wear resistant coatings used in industry nowadays do not solve the problems associated with friction, e.g. excessive heating, high energy losses, etc. Lubrication with various liquid and solid lubricants has been known to be a good solution to these problems for millennia. However, nowadays environmental and technical requirements reduce more and more the fields of application of the above mentioned lubrication methods. Therefore, it would be very beneficial for industry if high hardness, wear resistance and lubricating properties can be all combined in a coating. Thus both friction and wear problems will be diminished without the need to use external lubrication. In this work an effort is made to design a group of such PVD coatings by mixing doping a hard, wear resistant phase (TiN) with a well-known solid lubricant (MoS_2). The mixing is made by sequential deposition of thin layers of both phases in order to realize a multilayer TiN/MoS_2 structure and by co-deposition of both components in order to realize mixed-phase $TiN+MoS_2$ coatings. The influence of the deposition conditions on the structure and the tribological and mechanical properties of the above mentioned coating architectures is studied. A conclusion about the feasibility of both concepts (multilayer and mixed coatings) is also made in this work.

I. Introduction

I.1. Friction, wear, lubrication and surface modification

Friction and its "son" – wear, both are phenomena that occur everywhere around us. They are intuitively accepted as inevitable. It is difficult to imagine our life without friction and wear. We could not have a grip at things and our cars would not brake without friction. Equally unable we would be to sharpen our knives without wear. Our everyday-life encounters with friction and wear help us to define and comprehend them intuitively. However these phenomena are extremely complex in nature. Their complexity is studied and described by a whole science called tribology. Therefore it is worth making a brief description of the most important tribological relations and factors that govern the complex and not yet fully understood world of friction and wear.

I.1.1. Friction

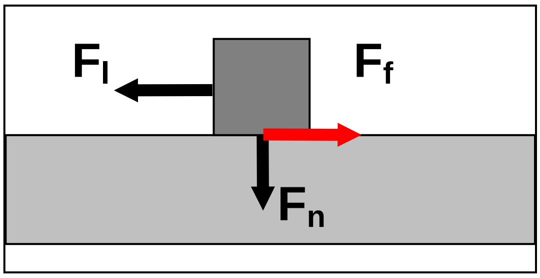

Fig. I.1. The friction force explanation

Let us consider the simple case of two bodies in contact as shown on Figure I.1. Here, the cube is pressed against the plane with a force $\mathbf{F_n}$ that is normal to both surfaces. In the same time, a gradually increasing lateral force $\mathbf{F_l}$ is applied to the cube. This force tends to slide it over the flat and is tangential to both surfaces. However the cube will not start sliding until $\mathbf{F_l}$ reaches a certain value. This is because a force $\mathbf{F_f}$, called friction force, opposes $\mathbf{F_l}$. The magnitude of $\mathbf{F_f}$ depends on the magnitude of $\mathbf{F_n}$ in the following manner:

$$F_f = \mu F_n \qquad (I.1)$$

where $\boldsymbol{\mu}$ is the so-called friction coefficient. Therefore, friction can be defined as a phenomenon that opposes sliding between two surfaces brought in contact to each other by a normal force. Although the relation between $\mathbf{F_f}$ and $\mathbf{F_n}$ is simple, $\boldsymbol{\mu}$ is a complex value and depends on many factors such as:

- Chemical and physical nature of the surfaces in contact;

- The presence of a third body or a fluid between them;
- Surface topography;
- Environment (temperature, atmosphere, radiation, etc.);
- In many cases – the normal force $\mathbf{F_n}$;
- Sliding velocity – the speed at which the two surfaces slide over each other can, for example, influence the temperature in the contact zone.

There are 3 components of the friction coefficient [1]:

- **Friction due to asperity interlocking and deformation**. Sliding surfaces can not be ideally smooth and always have asperities. When these asperities are brought to contact by $\mathbf{F_n}$, they interlock and oppose friction. Overcoming the interlocking by means of the deformation of the asperities contributes to the friction coefficient. This mechanism dominates the initial stages of sliding but can also contribute to value of the friction coefficient in the later stages in case new asperities are generated during sliding.

- **Friction due to ploughing of the wear particles created during friction**. Ploughing influences the friction coefficient most strongly the intermediate and late stages of sliding.

- **Friction due to adhesion of the sliding surfaces to each other**. Once the surfaces in contact have been activated by the friction (creation of dangling bonds, vacancies, revealing of pure reactive surfaces, etc.), adhesion between the sliding surfaces opposes the sliding thus contributing to the value of the friction coefficient.

In most tribological systems $\boldsymbol{\mu} < 1$. However, there are cases where the interactions (chemical and/or physical such as cold welding) between the two surfaces can increase μ to values greater than 1.

I.1.2. Wear

Wear is the removal of material from solid surfaces sliding relative to each other. The most common and widely accepted wear mechanisms are as follows:

- **Adhesive wear** – the sliding surfaces adhere strongly enough to each other that a very thin layer (usually – the asperities) of the softer one are removed from it and remain attached to the harder one.
- **Abrasive wear** – this type of wear occurs in sliding pairs where one of the materials is substantially harder than the other. Plastic flow of the softer material is responsible for the smoothening of its asperities and gradual removal of material atom by atom.
- **Fatigue and delamination wear** – cycling loading and unloading of the surface generates fatigue-induced cracks. After the crack onset, they propagate rapidly. Crack branching and merging lead to liberation and removal of material in the friction zone.
- **Chemical wear** – chemical reactions might be induced in the contact area by the chemical properties of the environment, the sliding materials or both. The combined effect of the sliding and the chemical reactions results in removal of material from the sliding surfaces.

As seen in (1), the amount of friction is defined by the friction coefficient. A widely adopted measure for the amount of wear is the so called wear rate **K**:

$$K = \frac{V}{F_n . s} \qquad (I.2)$$

where **V** is the volume of the material removed from the surface in question, $\mathbf{F_n}$ is the normal force as defined in eq. I.1 and **s** is the sliding distance. Formally, the dimension of the wear rate is $m^2.N^{-1}$. However, a much more instructive way of expressing **K** is in $m^3/(N.m)$. Such expression represents directly the physical meaning of **K** since the denominator has a dimension of energy. Hence **K** is the measure of the volumetric amount of removed material per unit energy input in the system. Typical values of K for many systems are in the range of 10^{-15} $m^3/(N.m)$ and less. Besides, in wear tests the volume of the removed material is in the range from zero to few mm^3. For these reasons, **K** is widely expressed in $mm^3/(N.m)$.

I.1.3. Lubrication

For many engineering applications such as bearings, gears, cutting tools and others friction and wear are unwanted. Lubrication is one of the most widely used means of their diminishing. There are two main groups of lubrication methods employed in industry: fluid pressure lubrication and surface film lubrication. The first method is based on the hydrodynamic phenomena that occur during sliding when a relatively thick (1-100 µm) layer of liquid lubricant is introduced between the sliding bodies. The pressure created in the lubricant layer keeps the surfaces of the sliding bodies entirely separated. In surface film lubrication the surfaces in contact are only partially kept apart from each other by very thin films attached to them by physical or chemical adsorbtion. Lubricant chemistry plays a very critical role in this lubrication mode. The second lubrication method is called surface film lubrication and has one very important subgroup that will be discussed in more detail. This is the so called solid lubrication which is realized by introducing a solid third body between the sliding surfaces. This solid body can be in the form of powder or a thin/thick film over one or both sliding surfaces. Clearly, not every solid possesses lubricating properties. Table I.1 gives a review of the most common types of lubricating solids.

Type	Lubrication Principle	Examples
Soft materials	Easy shearing and plastic deformation of the bulk material	Pb, In, Sn, Ag, Au, CaF_2, BaF_2, PbO, PbS, CdO
Lamellar solids	Easy shear of layered-lattice structure	Dichalcogenides: MoS_2, WS_2 and diselenides, ditellurides, graphite, BN_{hex}, graphite fluoride, Ag_xNbSe_2
Organic polymers	Polymers with low intermollecular bonding (cohesion) and low surface energy	PTFE, FEP, PFA, PTFCE, nylon, acetals, polyimides, metal soaps, waxes, solid fatty acids, esters
Chemical conversion layers	Surface oxides (reduce cold welding, shear) Porous surfaces (lubricant reservoir) Increased hardness	Oxide films Anodized surfaces Phosphated surfaces

Table I.1. Most common types of solid lubricants

Although solid lubrication is not an ideal solution for diminishing friction and wear, it offers many advantages over liquid lubrication. The most important of them, along with some disadvantages, are mentioned in Table I.1.

Advantages	Disadvantages
• Vacuum/clean room – no evaporation and contamination/loss of lubricant • Suitable for wide range of temperatures (from cryogenic to high) – no viscosity change, no freezing, evaporation or cracking; • Not flammable; • High load bearing capacity • High velocity lubrication– less friction dependence; • Maintenance - good for difficult access; • Ecological – minimal quantity; fluids pollute water + soil • Non-contaminating – e.g. food, textiles • Resistant to radiation – nuclear applications	• Poor thermal conductivity • Sensitive to atmosphere and humidity • Difficult or impossible to re-coat • No cooling effect, e.g. during metal working

Table I.2. Advantages and disadvantages of solid lubrication

From all types of solid lubricants mentioned in Table I.1, lamellar solids attract most industrial interest because compared to the other groups of solid lubricants, they have the following advantages:

- Wide range of operating temperatures. Soft metals and organic polymers harden and become brittle at cryogenic temperatures. This leads to loss of lubricating properties. Polymers can not withstand temperatures over 250 °C for long periods. Fluorides (such as CaF_2) are lubricants only at high temperatures.
- No need of special environment for providing lubrication. Unlike chemical conversion layers, lamellar solids need no chemical reaction of the sliding surfaces with each other and/or the environment.
- No radiation aging. Unlike organic polymers, lamellar solids are inorganic and hence do not suffer ageing when exposed to radiation.

The lubricating properties of lamellar solids and MoS_2 in particular will be discussed in more detail later in this work.

I.1.4. Surface modification and coatings deposition

Dramatic reduction of wear coefficient can be achieved by modifying the surface properties of the materials while preserving the useful properties of the bulk. It should be noted that wear reduction does not necessarily mean reduction of friction. Surface modification is another widely used method for diminishing wear. Two approaches are currently employed for improving the wear and friction properties of engineering surfaces. The first of them is surface hardening by means of various techniques such as ion implantation, laser-induced surface hardening processes, nitriding and spark hardening. Coating the surface with a layer of a well adherent wear resistant material is another method of choice for many applications and has been is gaining increasing popularity for almost 4 decades. Both surface modification and hard coatings have their advantages and application niches and both suffer some disadvantages. However, hard coatings are by far the most widely used means for wear reduction by modifying the surface properties. In the recent years approximately 80% of all metal working operations (drilling, cutting, turning, milling, etc.) are performed with coated tools [2]. Techniques including plasma and flame spraying, Chemical Vapor Deposition (CVD), Physical Vapor Deposition (PVD), electroplating, liquid salt electrolysis and others are within the arsenal of the modern coatings industry. Vapour deposition methods, however, have been most widely used in this field because they yield coatings with controllable and uniform thickness that meets even the tightest dimensional tolerances set by the machinery designers. Historically, the terms “PVD” and “CVD” were introduced by Powell et al. [3] in 1966 and represent the two deposition methods that are most widely commercialized and provide the vast majority of wear protective coating industry output.

Because of the relatively high temperatures needed in thermal CVD (800 °C and higher) the choice of cutting tool material to be coated was initially limited to only WC-Co and some other cemented carbides. Steels could not withstand such high temperatures without deformation, annealing and other undesired effects on their structure. By means of PVD dense coatings can be deposited even at room temperature although most commercial PVD coatings are deposited at temperatures above 200 °C. Non-toxic and inexpensive precursors are used and the deposition process is very suitable for automatic control and optimisation.

The first coated cutting tools were introduced to the marked in the late 1960s [4] although the first efforts on the topic published in periodicals became available in the middle of the 1970s [5], [6], [7], [8], [9], [10]. This, in turn, was a very strong basis for further development of wear protective coatings and towards the middle of the 1980s a significant amount of knowledge in the field was already accumulated [11]. Two main streams can be distinguished in the development of wear protective coatings :

- Hard coatings based ot TiN, TiC, Ti(C,N), (Ti,Al)N, (Ti,Al)(C,N), ZrN, CrN, Al_2O_3, diamond-like carbon (DLC) and others. These coatings posses high hardness (typically $HV_{0.5}$ above 20 GPa), low wear rate and relatively high friction coefficients.
- Solid lubricant coatings of soft metals, lamellar solids, some organic polymers and DLC, as listed in Table I.1. This group of coatings have low friction coefficient and their wear-diminishing properties are brought about by providing solid lubrication. Significant disadvantages of the coatings in this group, however, are their relatively low hardness and low wear rate compared to the hard coatings.

I.2. Goal of this work

Currently there is a big gap between the hard coatings and the solid lubricant coatings [12]. The only exception is DLC which has both high hardness (often exceeding $HV_{0.5}$ 60 GPa [13]) and low friction coefficient. The strong dependence of the tribological properties of DLC on the environment (especially on the presence of oxygen and water vapor in it), the significant stress levels in the coatings and the high wear rates when sliding against ferrous materials are the among the most serious disadvantages of the DLC coatings. Good overviews on the tribological properties of DLC are made in [14], [15], [16]. Despite the big amount of published effort on both hard and solid lubricant coatings, only in the recent decade research was published in the field of self-lubricating hard coatings. Methods other than vapour deposition have been also used [17], [18], [19], [20] but in this work only CVD and PVD coatings will be treated. The pioneering works of Bae et al. [21], [22], [23] were the first source in the field. His work was soon followed by others [24], [25], [26], [27], [28], [29], [30], [31], [32], [33], [34], [35], [36], [37], [38], [39] , [40], [41], [42], [43], [44], [45]. These publications represent almost all published effort in the field. Very little if no systematic study on the deposition conditions-structure-properties relation has been ever reported. The opposite approach is illustrated by the efforts of Fox et al. who improve the tribological properties of solid lubricant (MoS_2) coatings by doping them with Ti [46]. This is somewhat surprising since the development of a new type of coatings that combine the high hardness and low wear rate of the hard coatings with the low friction coefficient of the solid lubricant coatings would be beneficial for many applications by:

- Reducing or completely eliminating the need of fluid lubrication in metal working, bearings, linear guides, etc. Mineral and synthetic fluid lubricants bring increasing environment- and health-protection concerns.
- Increasing the lifetime and reliability of existing solid lubricant coatings in space and other high-tech applications. Solid lubricants are widely used in space exploration [47], [48] where reliability and long service life of the components and mechanisms are of critical importance.
- Increasing the lifetime of existing hard coatings in components and cutting tools. The high price of modern cutting tools, their difficult re-sharpening and the need to interrupt the cutting process in order to change the tool are very significant contributors to the overall price of the modern metal working.

This work aims at studying the concept of lowering the friction coefficient of a hard coating by means of adding a solid lubricant in its structure. In the scope of this work the hard coating should be considered the host (or "matrix") and the solid lubricant should be considered the dopant. Hence from this point on the solid lubricant doped hard coatings will be denoted as self-lubricating hard coatings. PVD will be used as a deposition method for the these coatings because of its advantages over other deposition methods such as CVD. The resulting PVD coatings should combine the high hardness and low wear rate typical for hard coatings ($HV_{0.5}$ 20 GPa and 10^{-6} $mm^3/(N.m)$, respectively [49]) with the low friction coefficient close to that of solid lubricant coatings. It should be pointed out clearly that this work does not aim at the development of a wear protective coating that in terms of wear resistance surpasses many or even any coatings reported in the literature. Since both wear resistance and friction coefficient strongly depend on the test set-up and conditions, any comparison of these values reported by authors who have used different test conditions and/or different testing equipment would be inconclusive and therefore useless. To prove or reject the above-mentioned concept, pure hard benchmark coating, a typical solid lubricant coating and self-lubricating hard analogues, all with identical thicknesses, will be deposited in the same deposition system on identical substrates at identical deposition conditions. Then their tribological and mechanical properties will be studied using identical testing condition and the same testing equipment. Friction coefficient of the self-lubricating hard

coating of a value between these of the benchmark hard coating and the benchmark solid lubricant coating and similar or lower wear rate of the self-lubricating hard coating compared to the hard benchmark coating will be the merit for assessing the prove of concept.

I.3. Approach

The study will be divided in the following sections:

Section 1. Definition of the materials for the hard phase and the solid lubricant

Section 2. Definition of the possible coating architectures of self-lubricating hard coatings

Section 3. Definition of the methods for deposition and deposition arrangement

Section 4. Definition of the methods for studying of the structure and the chemical composition of the coatings

Section 5. Definition of the methods for studying of the tribological and mechanical properties of the coatings and the coating-substrate composites

  Section 5.1. Characterization of the tribological properties

  Section 5.2. Characterization of the hardness

  Section 5.3. Characterisation of the adhesion

Section 6. Definition of the materials for the substrates and their surface finish

Section 7. Deposition of the benchmark coating as defined in WP 6

Section 8. Deposition, structural and tribological characterization of TiN/MoS_x multilayer coatings

Section 9. Deposition, structural and tribological characterization of co-deposited $TiN+MoS_x$ coatings

Section 10. Concluding remarks and recommendations for further studies

For the sake of simplicity, ease of reading and logical dividing, reference lists will be made after each chapter.

Reference List to Introduction

1. Suh, N. and Sin, H. *Wear* 55 1 **1981** 163-190

2. Rech, J., Kusiak, A., and Battaglia, J. *Surface and Coatings Technology* 186 **2004** 364-371

3. Powell, C., Oxley, J., and Blocher, J. *Vapor Deopsition* **1966 John Wiley andSons, Inc, New York**

4. Sproul, W. D. *Surface and Coatings Technology* 81 **1996** 1-7

5. Bunshah, R. *US Patent 3791852*

6. Nimmagadda, R. *Journal of Vacuum Science and Technology* 12 **1975** 815

7. Bunshah, R. *Thin Solid Films* 40 **1977** 169

8. Bunshah, R. *Thin Solid Films* 45 **1977** 453

9. Clarke, P. *Journal of Vacuum Science and Technology* 14 **1977** 141

10. Schiller, S. *Thin Solid Films* 64 **1979** 555

11. Sundgren, J. and Hentzell, H. *Journal of Vacuum Science and Technology A* 4 5 **1986** 2262-2279

12. Donnet, C and Erdemir, A. *Tribology Letters* 17 3 **2004** 389

13. Voevodin, A. and Donley, m. *Surface and Coatings Technology* 82 **1996** 199-213

14. Donnet, C *Surface and Coatings Technology* 100-101 **1998** 180-186

15. Grill, A. *Surface and Coatings Technology* 94-95 **1997** 507-513

16. Hauert, R. and Mueller, U. *Diamond and Related Materials* 12 **2003** 171-177

17. Krzanowski, J. E., Endrino, J. L., and Hirschman, K. *Surface Engineering 2002 - Synthesis, Characterization and Applications. Symposium (Mater. Res. Soc. Symposium Proceedings Vol. 750)* **2003** 273-278

18. Gadow, R. and Scherer, D. *Surface and Coatings Technology* 151-152 **2002** 471-477

19. Voyer, J. and Marple, B. R. *Surface and Coatings Technology* 127 2-3 **2000** 155-166

20. Straffelini, G., Colombo, D., and Molinari, A. *Wear* 236 **1999** 179-188

21. Bae, Y. W., Lee, W. Y., Besmann, T. M., Blau, P. J., More, K. L., and Braski, D. N. *Chemical Vapor Deposition of Refractory Metals and Ceramics III. Symposium* **1995** 231-236

22. Bae, Y. W., Lee, W. Y., Besmann, T. M., Yust, C. S., and Blau, P. J. *Materials Science & Engineering A (Structural Materials: Properties, Microstructure and Processing)* A209 1-2 **1996** 369-373

23. Bae, Y. W., Lee, W. Y., Yust, C. S., Blau, P. J., and Besmann, T. M. *Journal of the American Ceramic Society* 79 4 **1996** 819-824

24. Lee, W. Y. *Proceedings of the Thirteenth International Conference on Chemical Vapor Deposition* **1996** 629-636

25. Gilmore, R., Baker, M. A., Gibson, P. N., and Gissler, W. *Surface and Coatings Technology* 105 1-2 **1998** 45-50

26. Gilmore, R., Baker, M. A., Gibson, P. N., Gissler, W., Stoiber, M., Losbichler, P., and Mitterer, C. *Surface and Coatings Technology* 108-109 1-3 **1998** 345-351

27. Goller, R., Torri, P., Baker, M. A., Gilmore, R., and Gissler, W. *Surface and Coatings Technology* 120-121 **1999** 453-457

28. Hofmann, D., Schuessler, H., Bewilogua, K., Hübsch, H., and Lemke, J. *Surface and Coatings Technology* 73 **1995** 137-141

29. Guizhen, Xu, Zhongrong, Zhou, Jiajun, Liu, and Xiaohua, Ma *Wear* 225-229 1 **1999** 46-52

30. Voevodin, A. A., O'Neill, J. P., and Zabinski, J. S. *Surface and Coatings Technology* 116-119 **1999** 36-45

31. Keune, H., Lacom, W., Rossi, F., Stoffels, E., Stoffels, W. W., and Wahl, G. *Journal de Physique IV (Proceedings)* 10 **2000** 19-26

32. Efeoglu, I. *Surface and Coatings Technology* 200 **2005** 1724-1730

33. Chen, Ai, Zhang, Yong, Xiao, Hong, and Chen, Yue *Journal of Luoyang Institute of Technology* 22 2 **2001** 12-16

34. Feng, B., Cao, D., Meng, W., Rehn, L., Baldo, P., and Doll, G. *Thin Solid Films* 398-399 **2001** 210-216

35. Heinisch, C., Piplits, K., Kubel, F., Schintlmeister, A., Pfluger, E., and Hutter, H. *Applied Surface Science* 179 1-4 **2001** 269-274

36. Stuber, M., Leiste, H., Ulrich, S., Holleck, H., and Schild, D. *Surface and Coatings Technology* 150 2-3 **2002** 218-226

37. Voevodin, A. A., Fitz, T., Hu, J., and Zabinski, J. S. *Journal of Vacuum Science and Technology A* 20 4 **2002** 1434-1444

38. Cosemans, P., Zhu, X., Celis, J. P., and Van Stappen, M. *Surface and Coatings Technology* 174-175 **2003** 416-420

39. Huang, Y. Z., Stueber, M., Barna, P., and Rodenburg, J. M. *Chinese Journal of Nonferrous Metals* 14 spec. issue.3 **2004** 433-441

40. Spassov, V., Savan, A., Phani, A. R., Stueber, M., and Haefke, H. *Continuous Nanophase and Nanostructured Materials Symposium (Mater. Res. Soc. Symposium Proceedings Vol. 788)* **2004** 309-314

41. Audronis, M., Kelly, P., Arnell, R., Leyland, A., and Matthews, A. *Surface and Coatings Technology* 200 **2005** 1616-1623

42. Haider, J., Rahman, M., Corcoran, B., and Hashmi, M. S. J. *Surface and Coatings Technology* 200 **2005** 1080-1083

43. Rahman, M., Haider, J., Dowling, D. P., Duggan, P., and Hashmi, M. S. J. *Surface and Coatings Technology* 200 **2005** 1071-1075

44. Stueber, M., Barna, P. B., Simmonds, M. C., Albers, U., Leiste, H., Ziebert, C., Holleck, H., Kovacs, A., Hovsepian, P., and Gee, I. *Thin Solid Films* 493 **2005** 104-112

45. Xing-zhao, Ding, Zeng, X. T., and Goto, T. *Surface and Coatings Technology* 198 **2005** 432-436

46. Fox, V., Jones, A., Renevier, N. M., and Teer, D. G. *Surface and Coatings Technology* 125 **2000** 347-353

47. Donnet, C. *Surface and Coatings Technology* 80 **1996** 151-156

48. Roberts, E. W. *Thin Solid Films* vol.181 **1989** 461-473

49. Holmberg, K. and Matthews, A. *Coatings tribology* **1994 Elsevier**

Section 1. Definition of the materials for the hard phase and the solid lubricant

As mentioned earlier, the self-lubricating hard coatings that are the object of the current study consist of two components: a hard phase and a solid lubricant. Many wear protective coatings, both hard and solid lubricating, are used in the modern industry. However only one material should be selected from each of these two groups.

1.1. Hard phase

The ideal candidate for the role of the hard phase in the self-lubricating hard coatings that are the objective of this work would match the following requirements:

- Relatively simple crystalline lattice
- Relatively simple chemical composition, preferably a binary compound
- Good tribological properties such as high hardness and low wear rate
- Sufficiently high friction coefficient against many materials in order to be able to distinguish the effect of the solid lubricant when added to its structure
- To be well studied and widely used as a wear protective coating
- To allow doping with various elements in wide range of compositions
- To be relatively easy to deposit by PVD.

Titanium nitride (TiN) represents the first and most widely studied hard wear protective coating material. Since the late 1960s ample amount of published effort has been devoted to the study of the structure and properties of both PVD and CVD deposited TiN coatings because of the high hardness, low wear rate and good resistance towards oxidation of this material. Good reviews on the development, structure and properties of TiN coatings have been also made [1], [2], [3], [4], [5], [6], [7]. Further improvement of the tribological properties of TiN coatings has been carried out in the direction of alloying TiN with various elements and compounds. Ternary and quaternary coatings such as Ti(C,N), (Ti,Al)N and (Ti,Al)(C,N) have proved to be very useful in many applications [8], [9], [10], [11], [12]. A good overview on the development of (Ti,Al)N coatings is made by [13]. In all cases, however, these coatings are based on a TiN host lattice in which the other elements are dissolved to yield stable or metastable solid solutions. A typical example of stable solid solutions is the ternary Ti(C,N) system where perfect miscibility exists in the pseudo-binary phase diagram TiC-TiN [14]. Ternary nitrides containing Ti are well reviewed in [15]. In (Ti,Al)N there is a miscibility gap [16], [17], [18], [19], [20].

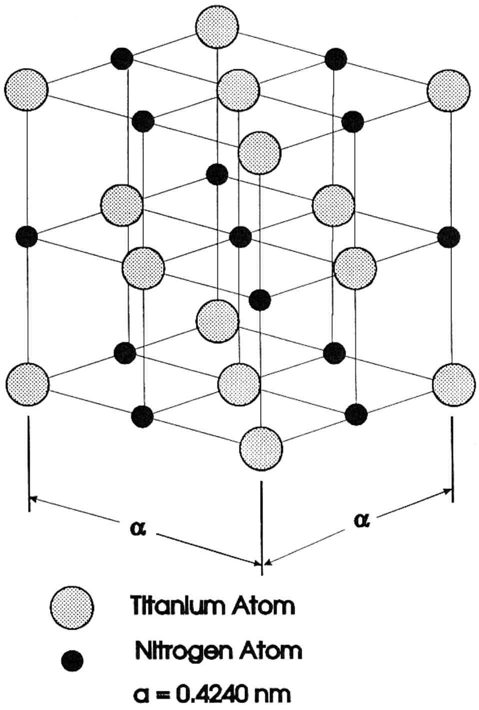

Fig. 1.1. Crystal structure of TiN

The hardness of bulk TiN is 18-21 GPa [15] and a simple NaCl-type face-centered cubic (fcc) crystal lattice as illustrated on Figure 1.1. This phase exists in a relatively broad range of compositions from $TiN_{0.6}$ to $TiN_{1.1}$ and belongs to the group of the so-called interstitial nitrides where the N atoms, being much smaller than the Ti atoms, nest in the interstices of the Ti sub-lattice. In substoichiometric $TiN_{<1}$ the N sublattice is deficient and in overstoichiometric $TiN_{>1}$ the Ti lattice is deficient. Significant concentration of vacancies in both sub-lattices also exist in stoichiometric TiN. The Ti-N phase diagram shown on Figure 1.2. The phase Ti_2N exists as a result of vacancy ordering at $TiN_{<0.6}$.

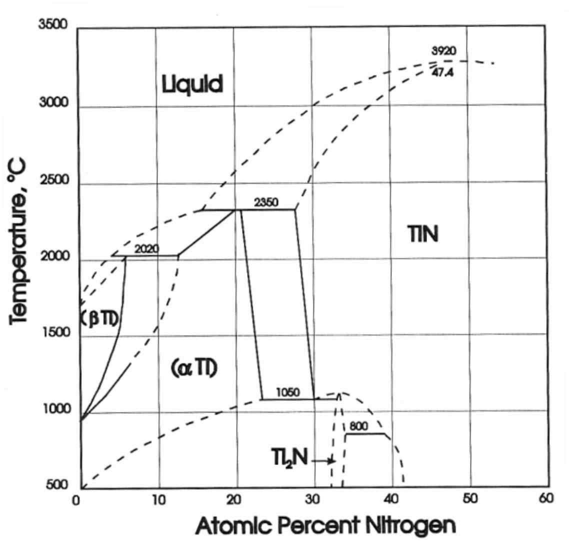

Fig. 1.2. Phase diagram of the system Ti-N

The reported friction coefficient of TiN against many materials varies in very wide range from 0.05 against sapphire in air [21] to 1.15 against chromium steel in air [22]. However, most authors that have studied TiN coatings tribology have reported values for the friction coefficient against various materials well above 0.3 [23].

From all these considerations it is apparent that TiN matches very well the requirements set. For this reason it was selected as the material for the hard phase in the self-lubricating hard coatings as well as a benchmark hard coating needed for proof of concept.

1.2. Solid lubricant

Analogically to the material for the hard phase, the material for the solid lubricant needs to satisfy the following requirements:

- Compatible with Ti and N
- Low friction coefficient
- Relatively simple and understood lubricating mechanism independent on the environment and the friction counterpart
- Easy to deposit by PVD
- Widely used and studied

Molybdenum disulfide (MoS_2) is a material that meets very well all these criteria. The first MoS_2 coating deposited by PVD was reported by Spalvins in 1969 [24]. This publication has triggered a lot of further studies of the deposition process conditions that govern the structure and the tribological properties of these coatings. Significant amount of knowledge has been accumulated by the researchers leading to the following conclusions:

- MoS_2 is compatible with Ti and N. Furthermore, Ti is intentionally used as a dopant of MoS_2 coatings in order to improve their tribological properties, as reported by many researchers [25], [26], [27], [28], [29], [30], [31], [32], [33], [34]. No report on the detrimental influence of N on the tribological properties of MoS_2 coatings could be found. A beneficial effect on nitrogen ion implantation on the tribological properties of sputter-deposited MoS_2 was reported by [35]. WS_2 is a solid lubricant very similar to MoS_2 in structure and chemical and tribological properties. Doping WS_2 with N has a beneficial effect on its tribological properties according to the studies of Nossa et al. [36], [37], [38].
- The friction coefficient of MoS2 coatings depends on the friction environment [39], [40], [41] and the structure of the coating [42], [43], [44], [40], [45], but is generally low with values in the range of 0.01-0.1.
- The lubrication mechanism of MoS_2 in general is described by Fleischauer [46] based on the electronic structure of MoS_2 and molecular orbitals theory. The lubrication

mechanism in MoS_2 coatings in particular is widely studied and relatively well understood [47], [48], [49], [50], [51], [52], [46], [53], [54].

- MoS_2 coatings are easy to deposit by PVD using sputtering from MoS_2 targets and there are many publications studying the effect on various deposition parameters on the structure and properties of the coatings deposited.

For all these reasons MoS_2 was chosen as the solid lubricant material in the scope of this work. Figure 1.3 shows the specific crystal structure of MoS_2 which is a layered hexagonal 2H type structure. It consists of S-Mo-S stacks layered upon each other. The Mo-S bonds inside the stacks are strong covalent while the S-S bonds between the stacks are week van der Waals type. The stacking is along the c-axis of the unit cell and the S-Mo-S stacks have (001) Miller indexes. The structure is strongly anisotropic and the week van der Waals bonds between the stacks are responsible for the lubricating properties of this type of structures since the stacks can easily slide relative to each other when shearing stress is applied on the crystal. The blue insert in Figure 1.3 denotes the plane of sliding which coincides with the plane with Miller indexes (002).

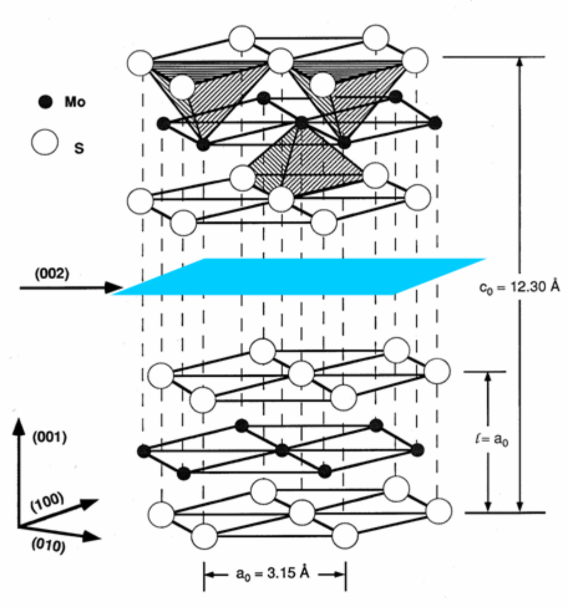

Fig. 1.3. Crystal structure of MoS_2

1.3. Summary of Section 1

TiN was chosen as the material for the hard phase and MoS_2 was chosen as the solid lubricant for combining in one self-lubricating hard coating. The influence of the coating architecture as well as the TiN/MoS_2 ratio on the structure and the tribological properties of the coatings will be studied.

Reference List to Section 1

1. Sundgren, J. *Thin Solid Films* 128 **1985** 21

2. Sundgren, J. E. and Hentzell, H. T. G. *Journal of Vacuum Science & Technology A (Vacuum, Surfaces, and Films)* 4 **1986** 2259-2279

3. Shanyong, Zhang and Weiguang, Zhu *Journal of Materials Processing Technology* 39 **1993** 165-177

4. Rebenne, H. E. and Bhat, D. G. *Surface and Coatings Technology* 63 **1994** 1-13

5. Chatterjee, S., Chandrashekhar, S., and Sudarshan, T. S. *Journal of Materials Science* 27 **1992** 3409-3423

6. Hultman, L., Engstrom, C., Birch, J., Johansson, M. P., Oden, M., Karlsson, L., and Ljungcrantz, H. *Zeitschrift fur Metallkunde* 90 **1999** 803-813

7. Hultman, L. *Vacuum* 57 **2000** 1-30

8. Horling, A., Hultman, L., Oden, M., Sjolen, J., and Karlsson, L. *Surface and Coatings Technology* 191 **2005** 384-392

9. Erkens, G., Cremer, R., Hamoudi, T., Bouzakis, K. D., Mirisidis, I., Hadjiyiannis, S., Skordaris, G., Asimakopoulos, A., Kombogiannis, S., Anastopoulos, J., and Efstathiou, K. *Surface and Coatings Technology* 177-178 **2004** 727-734

10. Lugscheider, E., Knotek, O., Barimani, C., Leyendecker, T., Lemmer, O., and Wenke, R. *Surface and Coatings Technology* 112 **1999** 146-151

11. Bull, S., Bhat, D., and Staia, M. *Surface and Coatings Technology* 163-164 **2003** 499-506

12. Bull, S., Bhat, D., and Staia, M. *Surface and Coatings Technology* 163-164 **2003** 507-514

13. PalDey, S. and Deevi, S. *Materials Science and Engineering A* A342 **2003** 58-79

14. Rudy, E. *Air-Force Materials Laboratory Report* AFML TR 65-2 Part V **1969**

15. Pierson, H. *Handbook of Refractory Carbides and Nitrides* **1996 Noyes Publications**

16. Kejun, Zeng and Schmid-Fetzer, R. *Thermodynamics of Alloy Formation. Proceedings Symposium held at the Annual Meeting of TMS* **1997** 275-294

17. Cremer, R., Witthaut, M., von Richthofen, A., and Neuschutz, D. *Fresenius' Journal of Analytical Chemistry* 361 **1998** 642-645

18. Cremer, R., Witthaut, M., and Neuschutz, D. *Value-Addition Metallurgy. Proceedings of an International Symposium Held at the TMS Annual Meeting* **1998** 249-258

19. Hultman, L., Engstrom, C., Birch, J., Johansson, M. P., Oden, M., Karlsson, L., and Ljungcrantz, H. *Zeitschrift für Metallkunde* 90 **1999** 803-813

20. Kimura, A., Hasegawa, H., Yamada, K., and Suzuki, T. *Journal of Materials Science Letters* 19 **2000** 601-602

21. Singer, I., Fayeulle, S., and Ehni, P. *Wear* 149 **1991** 375-394

22. Maillet, B., Celis, J., Roos, J., Stals, L., and van Stappen, M. *Wear* 142 **1991** 151-170

23. Holmberg, K. and Matthews, A. *Coatings tribology* **1994 Elsevier**

24. Spalvins, T *ASLE Transactions* 12 1 **1969** 36-43

25. Fox, V., Renevier, N., Teer, D., Hampshire, J., and Rigato, V. *Surface and Coatings Technology* 116-119 **1999** 492-497

26. Rigato, V., Maggioni, G., Boscarino, D., Sangaletti, L., Depero, L., Fox, V. C., Teer, D., and Santini, C. *Surface and Coatings Technology* vol.116-119 **1999** 176-183

27. Wang, D. Y., Chang, C. L., Chen, Z. Y., and Ho, W. Y. *Surface and Coatings Technology* 120-121 **1999** 629-635

28. Lingling Wu, Holloway, B, Prasad Beesabathina, Kalil, C, and Manos D *Surface and Coatings Technology* 130 **2000** 207-217

29. Renevier, N., Lobiondo, N., Fox, V. C., Teer, D. G., and Hampshire, J. *Surface and Coatings Technology* vol.123, no.1 **2000** 84-91

30. Rigato, V., Maggioni, G., Patelli, A, Boscarino, D, Renevier, N., and Teer, D. *Surface and Coatings Technology* 131 206 **2000** 210

31. Young, Hwan Ahn and Sun, Kyu Kim *Journal of the Korean Institute of Metals and Materials* vol.38, no.12 **2000** 1652-1656

32. Renevier, N., Hampfire, J, Fox, V., Witts, T, Allen, T, and Teer, D. *Surface and Coatings Technology* 142-144 **2001** 67-77

33. Renevier, N., Oosterling, H., Konig, U., Dautzenberg, H., Kim, B. J., Geppert, L., Koopmans, F. G. M., and Leopold, J. *Surface-and-Coatings-Technology* 172 **2003** 13-23

34. Sun, Kyu Kim, Young, Hwan Ahn, and Kwang Ho Kim *Surface and Coatings Technology* 169-170 **2003** 428-432

35. Huiwen, Liu and Xushou, Zhang *Thin Solid Films* vol.240, no.1-2 **1994** 97-100

36. Nossa, A. and Cavaleiro, A. *Surface and Coatings Technology* 142-144 984 **2001** 991

37. Nossa, A. and Cavaleiro, A. *Surface and Coatings Technology* 163-164 **2003** 552-560

38. Nossa, A. and Cavaleiro, A. *Journal of Materials Research* 19 8 **2004** 2356-2365

39. Christy, R. I. *Thin Solid Films* 73 2 **1980** 299-307

40. Aubert, A., Nabot, J. Ph, Ernoult, J., and Renaux, Ph *Surface and Coatings Technology* 41 1 **1990** 127-134

41. Menoud, C., Kocher, H., and Hintermann, H. E. *IPAT 85. 5th International Conference on Ion and Plasma Assisted Techniques* **1985** 277-282

42. Xiaoling, Zhang, Lauwerens, W., Stals, L., Jiawen, He, and Celis, J. P. *Journal of Materials Research* 16 **2001** 3567-3574

43. Spalvins, T. *ASLE Transactions* 19 4 **1976** 329-334

44. Fleischauer, P. D. *ASLE Transactions* 27 1 **1984** 82-88

45. Weise, G., Mattern, N., Hermann, H., Teresiak, A., Baecher, I., Brueckner, W., Bauer, H. D., Vinzelberg, H., Reiss, G., Kreissig, U., Maeder, M., and Markschlaeger, P. *Thin Solid Films* 298 1-2 **1997** 98-106

46. Fleischauer, P. D. *Thin Solid Films* 154 1-2 **1987** 309-322

47. Nozhenkov, M. V., Avilov, A. S., Voronin, N. A., Semenov, A. P., and Semiletov, S. A. *Physics, Chemistry and Mechanics of Surfaces* 3 8 **1985** 2438-2450

48. Spalvins, T. *Journal of Vacuum Science and Technology A* 5 2 **1987** 212-219

49. Grosseau-Poussard, J. L., Moine, P., and Villain, J. P. *Thin Solid Films* 224 1 **1993** 52-57

50. Spalvins, T. *Thin Solid Films* 96 1 **1982** 17-24

51. Spalvins, T. *Thin Solid Films* 73 **1980** 291-297

52. Nozhenkov, M. V., Voronin, N. A., Semenov, A. P., and Tovmasyan, Yu *Soviet Journal of Friction and Wear* 7 **1986** 14-18

53. Moser, J. and Levy, F. *Journal of Materials Research* 8 1 **1993** 206-213

54. Moser, J. and Levy, F. *Thin Solid Films* 228 1-2 **1993** 257-260

Section 2. Definition of the possible architectures of self-lubricating hard coatings

Possible combinations of a hard phase and a solid lubricant can have, in principle, the architectures shown on Figure 2.1.

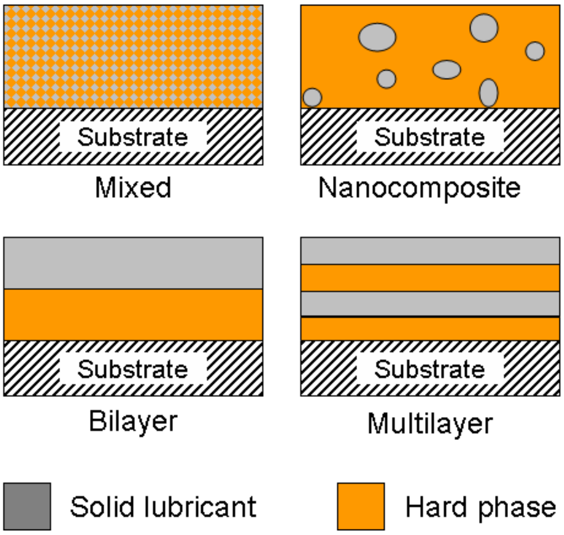

Fig. 2.1. Possible architectures of the self-lubricating coatings

2.1. Mixed and nanocomposite coating architectures

The mixed and the composite coating architectures are realised by the simultaneous deposition of the hard phase and the solid lubricant as shown on Figure 2.2. Such a deposition arrangement is often called co-deposition and this term will be adopted in this work. The vapour can be delivered to the substrate by using two or more sources pointing at the direction of the substrate or by using one composite source, containing both the hard phase and the solid lubricant. The content of both in the coating can be controlled by varying as follows

- For the case of sputtering from two or more sources: by controlling the sputter rate of every source which is made by varying the power supplied to the sources.
- For the case of sputtering from a composite source: by controlling the content of each component (hard phase and solid lubricant) in the source.

It is difficult to predict the resulting architecture of coatings obtained by co-deposition of a hard phase and a solid lubricant. This question is open at the present moment and will be clarified experimentally in this work. In the mixed coatings, the matrix and the dopant are mixed on atomic level. The resulting solid solution is monophase and can be amorphous or crystalline. In the composite coatings at least 2 phases can be distinguished. Clusters (mono-, polycrystalline or amorphous) of the solid lubricant some nanometers in size are uniformly dispersed within the hard phase matrix (amorphous or crystalline). Some solubility of the solid lubricant in the hard phase and vice versa is also be possible. The mechanism of solid lubrication in the nanocomposite coatings can be easily predicted. As the coating wears, there are always reservoirs of solid lubricant exposed at the surface of the wear track.

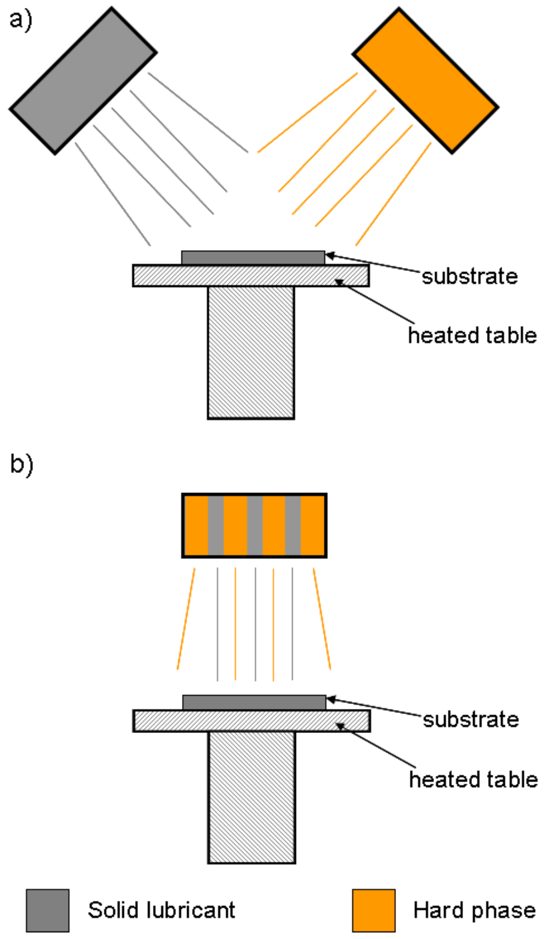

Fig. 2.2. Possible co-deposition arrangements: a) from multiple sources; b) from a mixed source

These reservoirs provide solid lubricant thus diminishing the friction. The lubrication mechanism of the mixed coatings, however, is difficult to predict. Furthermore, it is not even clear whether this structure, if obtained at all, will have any self-lubricating properties. This question will also be clarified in this work. Therefore, from now on, the mixed and the nanocomposite coatings will be denoted as co-deposited coatings based on the method for their deposition. Once information about their structure becomes available, the coatings will be denoted as mixed or nanocomposite.

2.2. Bilayer and multilayer coating architectures

The bilayer and multilayer architectures are realised by the sequential deposition of the constituents as shown on Figure 2.3. The thickness of each individual layer can be controlled by means of controlling the sputter rate of each source and controlling the time that the substrate is kept under the source in question. The solid lubricant is to be present throughout the entire volume of the coating in order to keep the friction coefficient low during its entire period of service. The bilayer coating structure is not considered to be useful in the scope of this work since once the top layer of solid lubricant is worn, no further lubrication

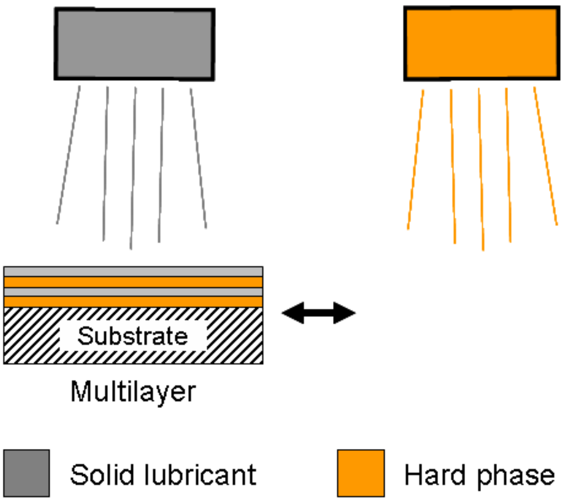

Fig. 2.3. Sequential deposition arrangement

will be provided for the underlying hard phase. In other words, one can not benefit simultaneously from the useful properties of the solid lubricant and the hard phase although the effect of decreasing the friction and wear when a layer of a solid lubricant deposited on a hard coating has been observed [1], [2], [3]. The multilayer structure can be useful in a real friction situation since such an effect, if constantly repeated many times throughout the multilayer coating wear life can lead to the overall effect observed with the composite and probably the mixed coatings. If the individual layers of the solid lubricant and the hard phase are very thin, in the range of few nanometers, overlapping of the effects of each phase on the overall properties of the coating will take place. Furthermore, due to local fluctuations in friction conditions, the multilayer coatings never wear layer by layer in such a way that there is only one phase present at the entire surface of the wear track at any moment. Rather, all the phases that present in the coating (i.e. all types of individual layers) are exposed at different parts of the wear track thus being able to exhibit their properties.

2.3. Summary of Section 2

For reasons mentioned above, in this work only co-deposited and multilayer coatings will be deposited and studied. For the sake of clarity, they will be described in separate chapters. Since the multilayer coatings contain their constituent phases in pure state, they will be studied first.

Reference List to Section 2

1. Spalvins, T. *Wear* vol.46, no.1 **1978** 295-304
2. Srivastav, A., Kapoor, A., and Pathak, J. P. *Wear* 155 2 **1992** 229-236
3. Guizhen, Xu, Zhongrong, Zhou, Jiajun, Liu, and Xiaohua, Ma *Wear* 225-229 1 **1999** 46-52

Section 3. Definition of the methods for deposition and deposition arrangement

In this group of deposition methods the material to be deposited is brought to the surface of the substrate in gaseous state. The deposition is carried out in chambers at pressures below atmospheric although there are some exceptions such as atmospheric CVD. Typical values are difficult to outline because of the wide range of pressures used varying from as low as possible to obtain with the current vacuum pumps to atmospheric. Nevertheless, most processes operate in the range of 0.1 ÷ 100 Pa. Based on the way in which the material to be deposited is brought to gaseous state, 2 main groups of vapour deposition methods are distinguished: CVD and PVD.

3.1. CVD

In CVD all materials to be deposited are delivered to the deposition chamber in the form of gases such as CH_4, SiH_4, etc. or vapours of volatile compounds such as $TiCl_4$, organometallics and so on. These gasses decompose in the chamber yielding solid materials that condense at the substrate. Below is a typical example for a gaseous state reaction widely used in the coating industry to deposit TiN coatings:

$$\mathrm{TiCl_4 + NH_3 + \tfrac{1}{2}H_2} \xrightarrow{\textbf{\textit{heating}}} \mathrm{TiN + 4HCl}$$

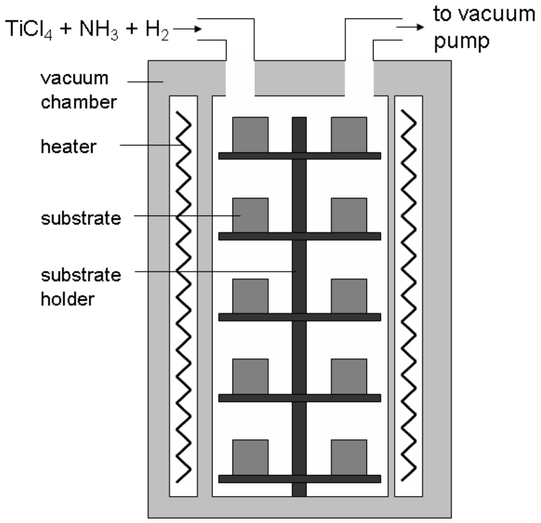

Fig. 3.1. A typical thermal CVD arrangement

The gas decomposition is caused by some sort of energy input in the chamber, for example thermal energy (thermal CVD), ion bombardment (plasma-assisted CVD, often denoted as PACVD), light (laser-CVD) and so on. A thermal CVD chamber is shown on Figure 3.1. Although many types of energy input decompose the gasses even at low temperature, dense and well adherent wear protective CVD coatings are obtained only when heating the substrate. In some very widely commercialised processes such as thermal CVD these temperatures very often exceed 800 °C. Because of this, the choice of materials to be coated was initially limited to only WC-Co and some other cemented carbides.

Steels could not withstand such high temperatures without deformation, annealing and other undesired effects on their structure. Introducing the Plasma-Enhanced CVD (PECVD) broadened the range of substrate materials because of the lower operating temperature of the PECVD (typically about 400 °C) compared to thermal CVD. However even this reduction in operating temperature is not sufficient to satisfy the requirements of many engineering materials. Another drawback of CVD is the use of expensive, toxic, explosive and flammable gaseous precursors. Handling these precursors and providing safe working environment is rather challenging not only from technical but also from economical point of view. A big advantage of CVD is the ability to uniformly coat very complex shapes and even inner surfaces of tubes and other similar geometries. The current state of the art in the CVD coatings is reviewed very well by Choy [1].

3.2. PVD

In PVD at least one of the materials to be deposited is brought to gaseous state by means of evaporation from a solid source or a melt facing the substrate or at least being at oblique angle relative to it. Gasses such as N_2, CH_4, O_2 and others might also be introduced in the chamber in order to react with the vapour so the product of the reaction is deposited on the substrate. This process is known as reactive deposition. A typical PVD deposition system is shown of Figure 3.2. The vapour source can be positioned above, below or aside the substrates depending on the design of the deposition system. Various techniques have been successfully used in PVD to evaporate solids and melts. Two groups of such techniques can

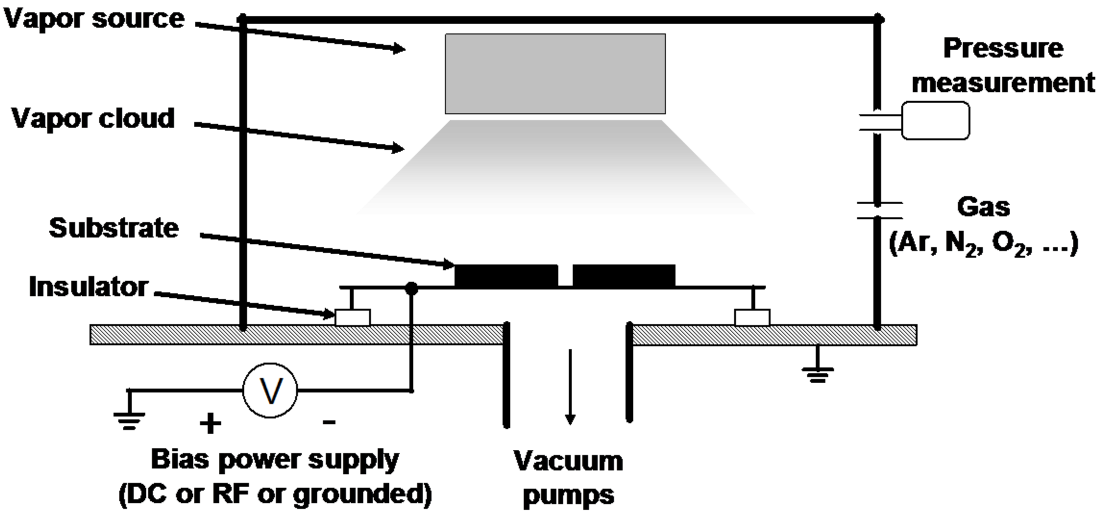

Fig. 3.2. A typical PVD deposition system

be distinguished based on the type of input of energy needed for evaporation: thermal (thermal evaporation) and momentum transfer (physical sputtering).

3.2.1. Thermal evaporation

In thermal evaporation the material is heated to a temperature at which its vapour pressure is sufficiently high for providing reasonable rate of deposition on the substrate. Heating is achieved with either of the following:

- Electrical resistive heating – the material to be evaporated is placed in a container made of refractory metal (W or Mo). Electric current is fed through the container resulting in Joule heating of the latter. For deposition of refractory metals and their compounds often no container is used and the current is fed directly through the metal which is in the form a filament or foil. Electrical resistive heating is not used, at least not industrially, for the deposition of wear protective coatings because of the low degree of ionisation of the evaporated species resulting at insufficiently strong adhesion of the coatings to the substrates. Another serious disadvantage of resistive evaporation is that alloys can not be evaporated with the vapour composition sufficiently uniform over the time due to difference in the vapour pressure of the elements of the alloy. When compound coatings are to be deposited by evaporation, individual evaporators are used for every component of the coating. This is also inconvenient since it complicates the design of the deposition system and limits the lateral compositional uniformity of the coating. Mostly low melting point substances such as Cu, Pb, Al, Se, etc. are evaporated by means of resistive heating.

- Electron beam heating – the material to be evaporated is placed in refractory metal container and subjected to intensive electron beam bombardment. The method offers the advantage of being able to deliver high degrees of ionisation of the vapour cloud by means of ionising collisions between the vapour species and the electrons from the electron beam. Thus plasma is created near the evaporation source. The ions from the plasma can be accelerated towards the substrate by means of applying negative bias to it. As a result dense and well adherent coating can be deposited. Another advantage of the method is that only the material to be evaporated is directly heated by the electron beam. Therefore the refractory container is subjected to substantially lower temperature compared to that used in resistive heating. This minimizes the chemical interaction with the contained material and also the vapour pressure of the material the container is made of.

- Cathodic arc evaporation – this method was first used by T. Edison [2] for plating phonograph cylinders. The principle of operation of the cathodic arc evaporation is shown on Figure 3.3. An electric arc is ignited and sustained between the material to be evaporated (cathode) and an anode. In many cases the grounded deposition chamber walls play the role of the anode. The temperature of the point at which the arc strikes the cathode is in the order of 10^4 K and combined with the very high electron current in the arc, this results in very high degree of ionisation of the evaporated species, typically 90% or more [3]. The kinetic energy of the ions and neutrals is thus in the range 40-100 eV . Negative bias applied to the substrate accelerates the ions further. Very effective sputter-cleaning of the substrate and shallow implantation of the ions takes place when the accelerated ions collide with the surface of the substrate and the growing coating. These features result in dense and very well adherent coatings [4]. Small particles, typically from less than 1 to few micrometers in size are ejected from the molten pool, travel to the substrate and remain embedded in the growing film. These particles are huge compared to the size of the ions and the neutral species in the plasma. Therefore they are called macroparticles. The surface of a typical arc-deposited coating and a cross-section of a tri-layer coating with an embedded macroparticle are shown on Figure 3.4.

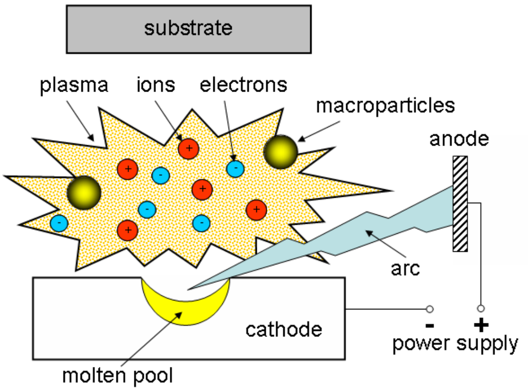

Fig. 3.3. Cathodic arc

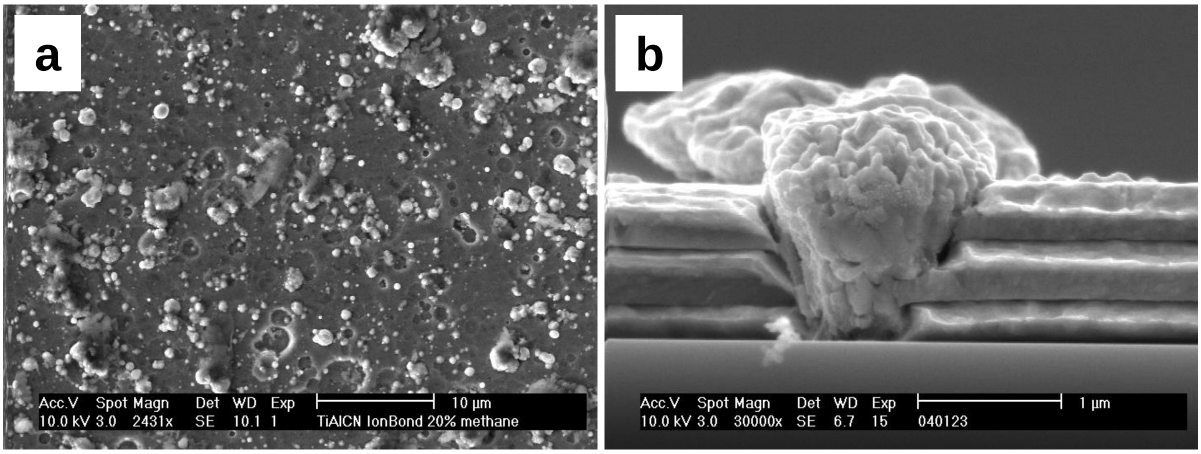

Fig. 3.4. The macroparticle problem: a) surface of an arc-deposited coating with the macroparticles clearly visible; b) a cross-section of a coating with a macroparticle embedded in it

The macroparticles can be harmful for the tribological properties of the coatings. Especially unacceptable they are for applications where smooth and defect-free surfaces are needed such as magnetic storage devices, optics and microelectronics. Substantial reduction of the number of macroparticles per unit area can be made by using special magnetic filters placed between the cathode and the substrate to be coated [5]. This technique is called Filtered Cathodic Vacuum Arc (FCVA) and is used widely in modern coating industry. A schematics of FCVA source and a photograph of the source in action are shown on Figure 3.5.

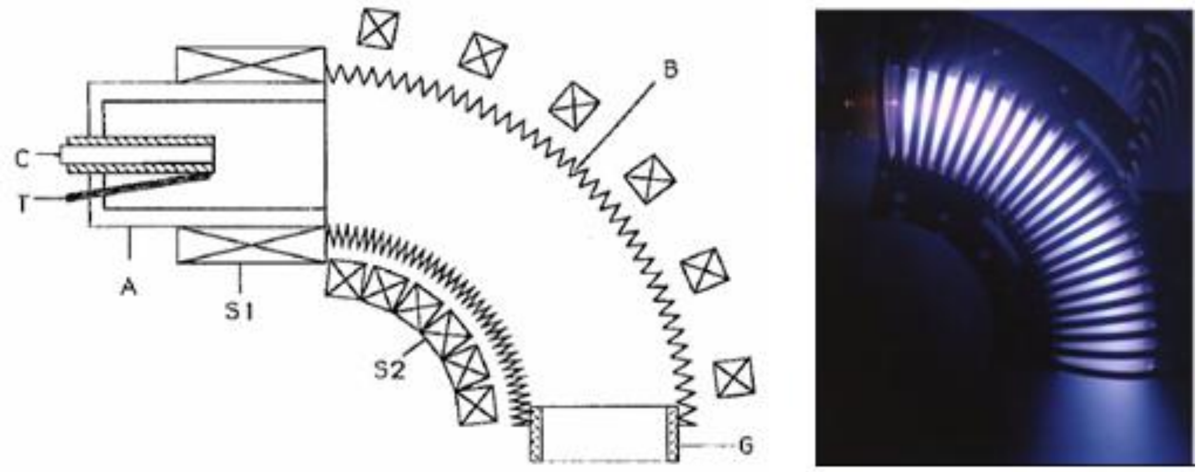

F*ig. 3.5. a) Schematics of a FCVA source. A – anode, C- cathode, T – trigger, S1 – focusing solenoid, S2 – guiding solenoid, B – duct, G – glass tube; b) the source in* operation

The ions and electrons of the plasma produced by the cathodic arc source are guided through a toroidal magnetic field due to the interaction of their charge with it. Ducting plasma through straight and curved magnetic fields was pioneered by Aksenov and his co-workers [6] and was further studied in detail in [7,8,9,10,11,12,13,14]. The field itself is created by a bent solenoid. Since the microdroplets are either neutral or their electric charge is very small compared to their mass, they are trapped in the filter so the plasma on its exit contains very small amount of microdroplets. Double-bent (S-shape) filters provide further reduction of the number of microdroplets at the exit of the filter so very smooth coatings suitable for electronics can be produced by FCVA nowadays [15]. In summary, cathodic vacuum arc evaporation offers the following advantages:

- Similarly to the other evaporation methods, cathodic arc evaporation can operate in physical vacuum.
- The coatings obtained are dense and very well adherent because of the high energy of the ions and neutrals generated by the cathodic arc.

- High deposition rates can be achieved.
- Control of the energy of the ions arriving at the substrate can be controlled by applying bias to it
- No poisoning (see below) of the cathode occurs in contrast to reactive sputtering

However, cathodic arc evaporation has some important disadvantages:

- Impossible to evaporate dielectrics.
- Generation of macroparticles (greatly reduced by using magnetic filters).
- Cathode difficult to manufacture – cast metallic cathodes are practically the only choice.
- High thermal load on the target.

The advantages of cathodic arc evaporation make the method very widely applied in the modern wear protective coating industry. Advances in magnetic arc filtering reduce the macroparticle content to levels acceptable for electronics and magnetic storage devices.

3.2.2. Sputtering

The term “sputtering” has its origin from the Latin verb “sputare” which means “to emit saliva with noise”. The physical process of sputtering was first reported by Grove in 1852 [16]. He sputtered from a needle held close to a highly polished silver surface at a pressure of about 0.5 Torr. There was deposit on the silver surface when it was used as the anode and the needle was used as the cathode. The sputtering process is illustrated on Figure 3.6 and can be described as a removal of material from a solid surface (referred to as a target) by bombarding it with particles with sufficient kinetic energy. The removed material is in gaseous (vapour) state and consists of neutral atoms, ions and electrons. Unlike the evaporation techniques described above, sputtering does not melt the material to be evaporated which is a very big advantage of the method. This means that the vapour has the same composition as the target. Hence, alloys and compounds can be evaporated with constant chemical composition of the vapour over the time.

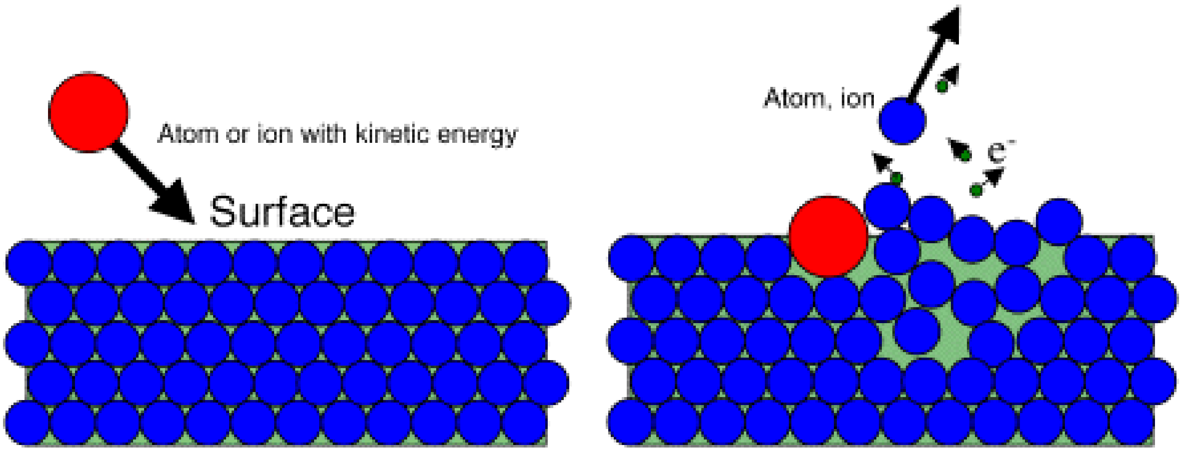

Fig. 3.6. The nature of sputtering process.

Although the principle of sputtering is simple to comprehend, the interaction of an accelerated particle with a solid surface is very complex. Some of the processes that take place when an accelerated particle collides with a surface are shown on Figure 3.7. From all these processes secondary electron emission and sputtered particles are the most important products for the scope of sputtering.

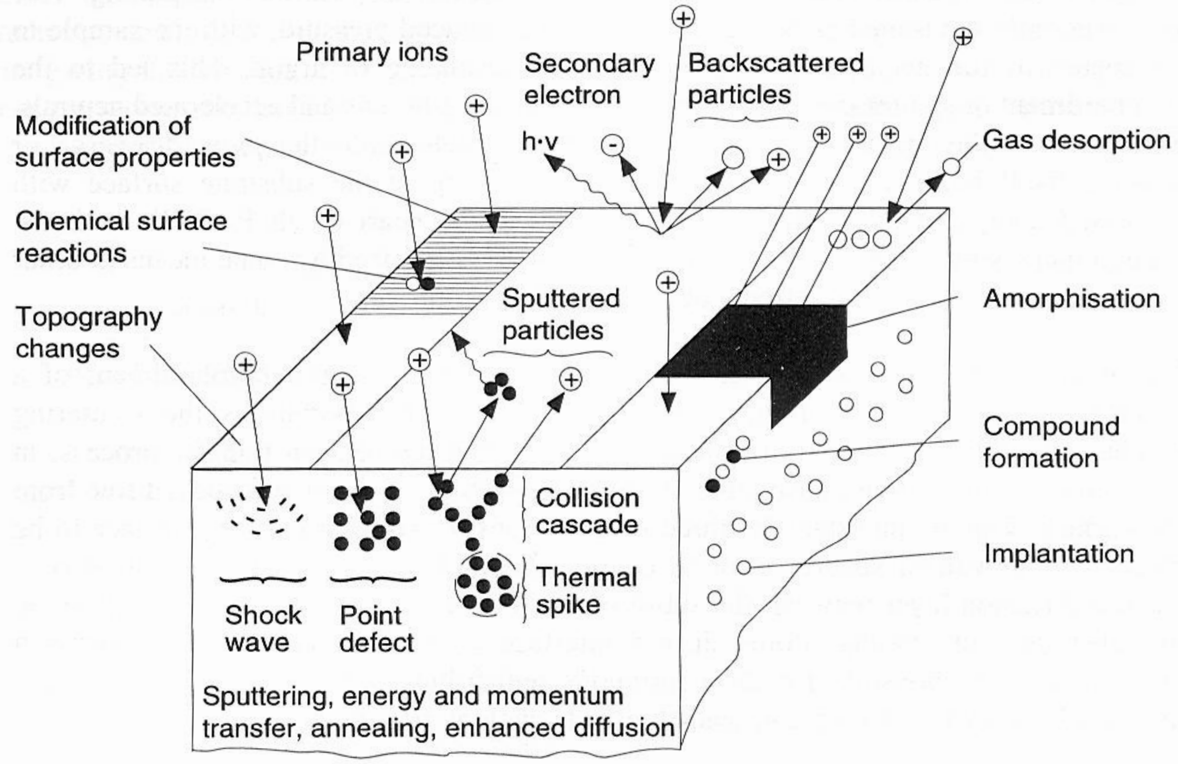

Fig. 3.7. Surface and subsurface processes following a collision of an accelerated particle with a solid surface

The particles bombarding the target are in most cases ions. They are charged particles and can be accelerated easily unlike neutral atoms or molecules. In order to avoid chemical interaction of the accelerated ions with the target, noble gasses are used for sputtering. Argon is the usual choice because it is inert, inexpensive, non-toxic, stored easily under pressure and, most important, its atom is heavy enough to sputter practically any material. The way the ions are accelerated towards the target divides sputtering into many types. The ions can be created away from the target and accelerated towards it by ion sources like the one shown on Figure 3.8. In most industrial sputter-deposition systems, however, sputtering is realized by the so-called glow discharge method.

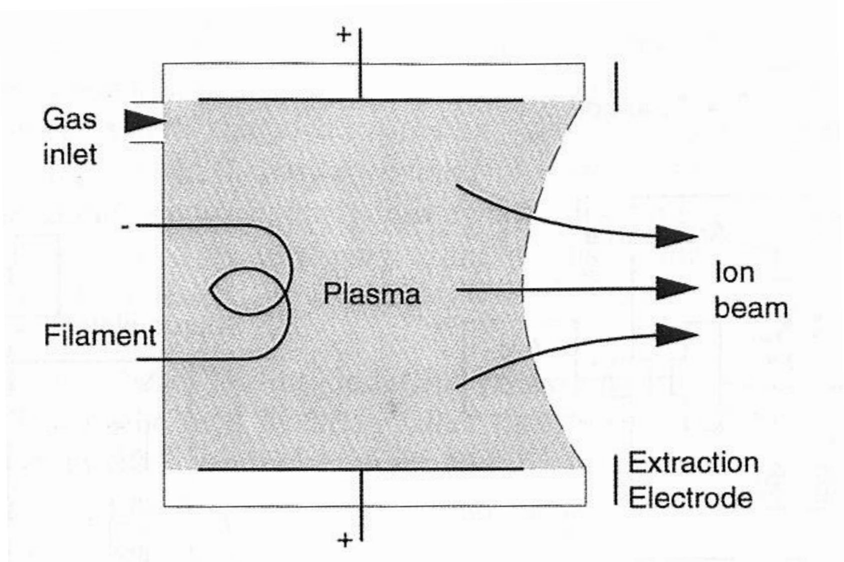

Fig. 3.8. An ion source principle

3.2.2.1. Glow discharges

When increasing voltage is applied to the target placed in low-pressure noble gas environment, a voltage-current dependence as shown on Figure 3.9 is observed.

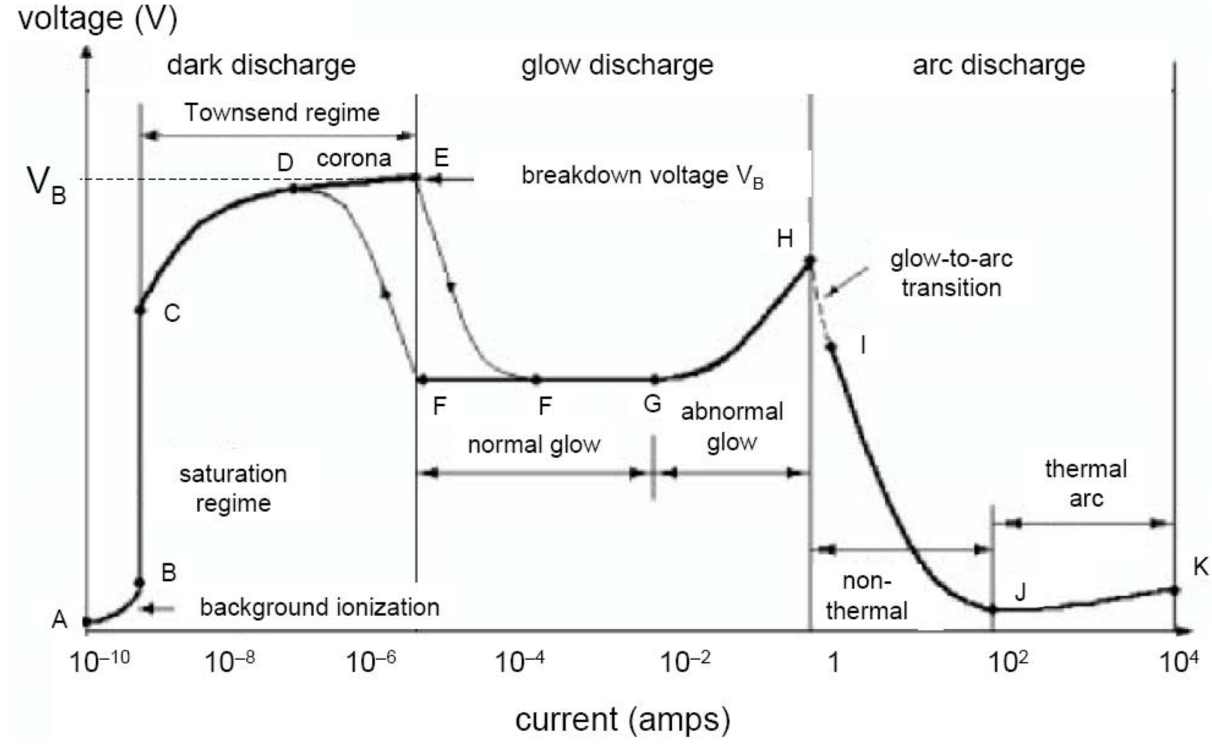

Fig. 3.9. Glow discharge V-I characteristics

The phenomena in the different regions of the voltage-current curve are as follows:

A to B: the applied electric field accelerates residual ions and electrons that are due to the background radiation in the system (from cosmic rays, radioactive materials in the room construction, etc.). These ions and electrons move towards the electrodes.

B to C: as the applied voltage increases, eventually all the available residual charges are swept up. This causes the current through the tube to saturate. The system is now operating in the saturation regime.

C to E: as the applied voltage increases beyond C, the E field is now large enough that remaining electrons can ionize gas atoms that they collide with before reaching the anode. As the voltage increases further, secondary electrons can also cause ionization.

D to E: once in the Townsend regime, coronal discharges can occur at various edges, sharp points or wires in the gas. This is due to the electric field enhancement that happens at such sites. These can be visible.

At E: at point E, electrical breakdown occurs. The voltage is high enough now that ionization occurs due to secondary electrons in the gas as well as the generation of additional secondary electrons at the cathode due to ion impact there. There is a sudden increase of current by several orders of magnitude causing an avalanche.

F to G: after breakdown from E to F, the gas enters the normal glow where the voltage is almost independent of current over several orders. As the current increases, the fraction of the cathode occupied by plasma increases until the plasma covers the entire cathode surface at G.

G to H: in the abnormal glow regime, further increases in voltage causes increases in current to provide the desired current in the system. This is the region of operation for most sputtering and other plasma systems. At this state, the ions extracted from the plasma by the negative charge of the target bombard it with sufficient kinetic energy to cause sputtering.

H to K: at H, the electrodes have become sufficiently hot that the cathode can now emit electrons thermionically and a second avalanche can happen. If the power supply is capable (low internal impedance), a transition from glow to arc happens in H to I. In the arc regime from I to K, the discharge voltage decreases as current increases until J.

3.2.2.2. Magnetrons

Secondary electrons emitted from the target and the electrons of the plasma are both repelled away from the target due to its negative potential. These electrons travel through the plasma and many of them leave it without undergoing collision(s) with the neutral atoms of the plasma. Thus ionization of the plasma can be improved by somehow trapping the electrons near the surface of the target thus increasing the probability for ionising collisions. Logically, the more ions exist in the plasma, the more ions will be accelerated towards the target and the more effective the sputtering process will be. The confinement of the electrons near the target was first reported by Penning in 1936 [17] who patented his idea in 1939 [18]. He used a combination of electric and magnetic field around the target with the magnetic field lines parallel to it surface. This allowed for better ionization of the plasma, shorter distance for acceleration of the positive ions towards it and as a result, effective sputtering at lower pressures and with higher rates. The devices that use magnetic fields for enhanced sputtering are called magnetrons. Magnetic fields that emerge from and re-enter into the target's surface have proved to be more efficient than that parallel to the target surface. Such magnetic electron confinement was patented by Knauer in 1965 [19]. However, his device was not primarily intended for sputtering but was an ion-getter pump. Clarke was the first to introduce magnetically-enhanced sputtering device in 1968 [20] called Sputter-gun or S-gun which had a tubular target geometry. Penfold and Thornton invented the post magnetron [21], [22]. The first planar target magnetron was reported by Corbani in 1973 [23]. However, Chapin is recognized to be the inventor of the planar magnetron [24], [25]. In the modern coating industry, planar magnetrons are most used most frequently for sputtering. The operating principle of a planar magnetron is shown on Figure 3.10. The electrons in the plasma spiral around the magnetic field lines. This increases the length of their paths through the plasma, hence the probability for ionising collisions with the neutral atoms in it. If the magnets at the periphery of the magnetron have the same strength as the central magnet, the magnetron is of the so-called balanced type (because the magnetic fields around it are balanced). The degree of ionization of the plasma are high only very close to the surface of the target of a

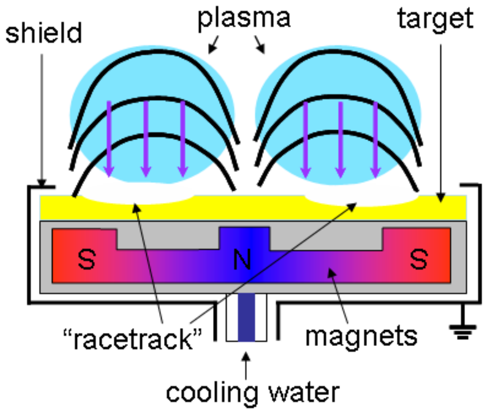

Fig. 3.10. The planar magnetron schematics

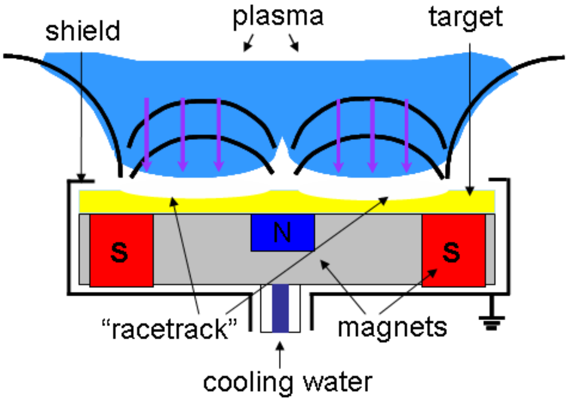

Fig. *3.11. Unbalanced magnetron schematics* balanced magnetron. Extending the plasma away from the target has a beneficial effect on increasing the reactivity of the reactive gasses fed into the chamber (if any) and providing mild ion bombardment of the growing coating. The latter results in more adherent, hard and dense coatings. The plasma extension can easily be provided by using of peripheral magnets stronger than the central one as shown on Figure 3.11. The peripheral magnets are stronger than the central one. Thus their field lines are not compensated (balanced) by the central magnet and extend into the deposition chamber. The electrons spiral around these lines thus sustaining the plasma away from the target. This configuration of a magnetron is called unbalanced magnetron. It was first introduced by Windows and Savvides in 1986 [26] and is the type of a magnetron that is used most widely in coating industry nowadays. For both balanced and unbalanced magnetrons, the target is eroded non-uniformly because the magnetic field is not uniform above it. The so-called "racetracks" form at the regions subjected to most intensive sputtering. Such racetracks are illustrated on Figure 3.12. This is a certain disadvantage of magnetrons since it allows not more than approximately 30% of the target volume to be used before the target is perforated. One possible way to improve the uniformity of the target usage is to use electromagnets with variable configuration of the field instead of permanent magnets. This, however, increases the energy consumption, complexity and price of the magnetron.

Fig. 3.12. "Racetrack" on a used magnetron-sputtering aluminum target

A further increase of the ion bombardment of the growing coating can be made by applying negative bias to the substrate. This extracts ions from the plasma and accelerates them towards the growing coating. Such energy bombardment improves the coating characteristics such as adhesion to the substrate, density and hardness. It also modifies the structure of the coatings by affecting the nucleation and crystal growth processes.

As shown on Figure 3.7, heat is one of the products of the collision of the incident ion with the target. This generated heat is a substantial portion of the total energy input of the magnetron. Cooling with water is therefore needed. Some magnetrons use either direct water flow flushing the back of the target and others use water-flushing a the face of the magnetron at which the target is tightened. Usually the first approach provides much more effective target cooling but it requires the target to be bonded to a copper backing plate. Silver-filled epoxy resins or indium are used in most cases for target bonding. The second approach to target cooling allows targets without backing plates to be used (including porous targets) but in this case the target cooling is not so effective and lower magnetron power is to be used in the case of temperature-sensitive targets.

Non-conductive targets can only be sputtered if polarity-changing voltage is fed to the magnetron. The frequency band of 13.56 MHz is internationally permitted for sputtering purposes. This band is in the radio-frequency range, hence sputtering with voltage modulated at 13.56 MHz is called Radio-Frequency (RF) sputtering. Besides providing the capability to sputter dielectrics, RF sputtering does not lead to charge accumulation at the target. Charge accumulation leads to arcing and special (and expensive) measures are to be taken to prevent it. However, in most industrial systems Direct-Current (DC) sputtering is used because it is more simple than RF sputtering, metallic targets are mostly used and arcing problems are not so severe.

If metal compound coatings are to be deposited such as oxides, nitrides, carbides, etc., usually sputtering of a metallic target is used to provide the metallic vapour and reactive gas is used to provide the non-metallic element such as oxygen, nitrogen, CH_4, C_2H_2, etc. These gasses are seldom used pure and in almost all cases are mixed with the sputtering gas (usually Ar). This deposition method is called reactive sputtering and the vast majority of wear-protective coatings are deposited using it. However, the flow rate of the reactive gas fed to the deposition chamber is to be carefully controlled. If the flow is too low, mostly metallic films are deposited. If the flow is too high, the so-called poisoning of the target takes place. This is caused by reaction of the target surface with the reactive gas and formation of a compound film on its surface that hinders sputtering. This phenomenon is not observed with arc evaporation.

3.3. Summary of Section 3

For the current study, a small research and development RF unbalanced magnetron sputtering system was used. Figure 3.13 shows the schematics of the system. It is supplied with 3 unbalanced magnetrons, two of which have RF power supplies capable of delivering up to 500 W to each magnetron. The third magnetron is supplied with a DC power supply capable of delivering 600 W power to the magnetron. Al three magnetrons can accommodate disk targets with 5 cm diameter and 6 mm height. DC bias voltage up to 750 V can be supplied to the substrate table. The substrate table is radiation-heated with two standard quartz lamps and rotated under each magnetron.

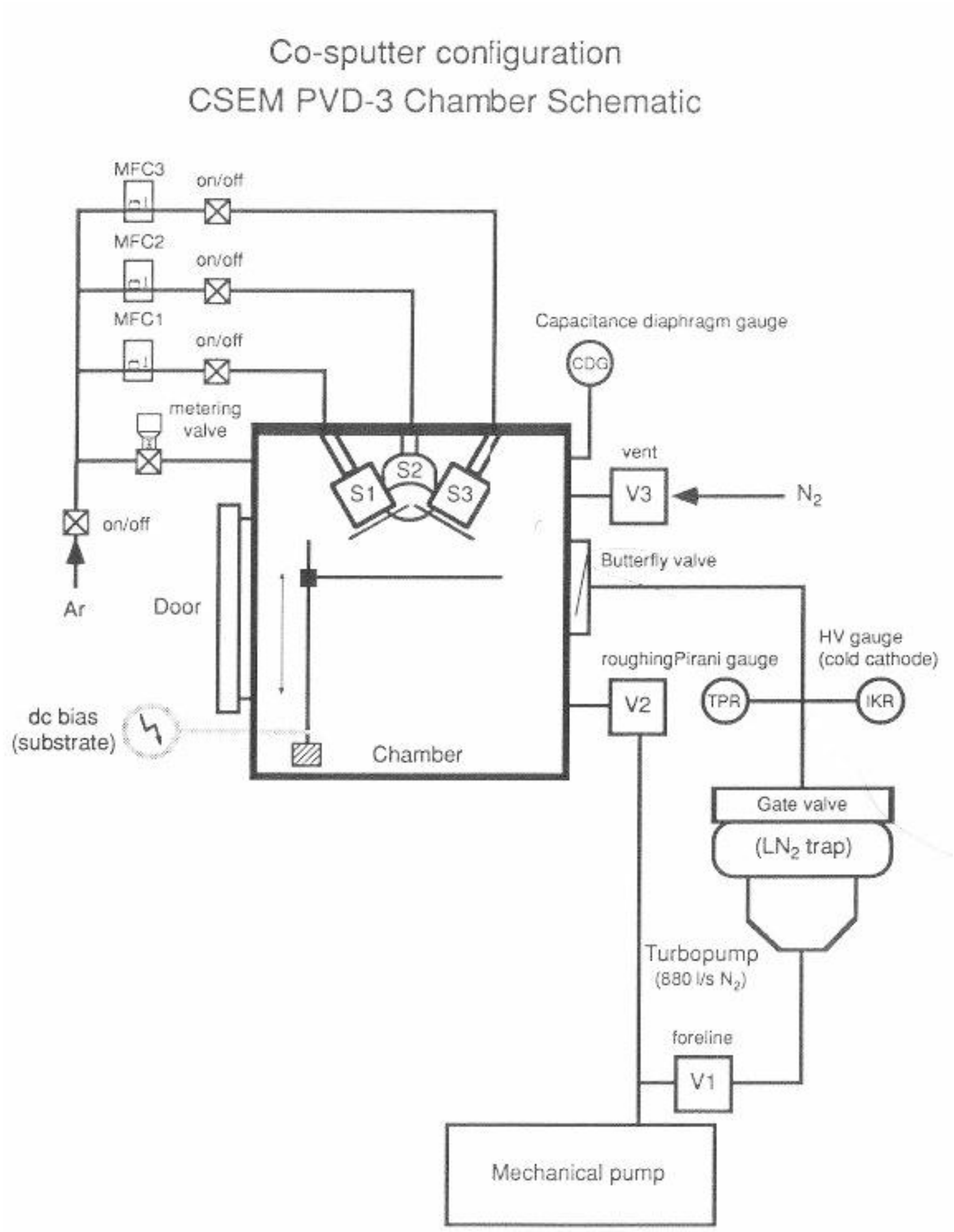

Fig. 3.13. Schematics of the deposition system used in this work

The temperature is measured with a K-type thermocouple inserted in a stainless steel disk and electrically insulated from the substrate. For the sake of preciseness, the temperature was measured only when the magnetrons are not operated and there is no DC bias supplied to the substrate table. This is made in order to avoid charging of the thermocouple by the plasma and hence obtaining a false reading. The substrate-to-target distance can also be varied. The pressure is measured by a Pirani cold cathode pressure gauge and was in all cases below 10^{-3} Pa prior to deposition. The preparation for deposition included 15 minutes of simultaneous operation of the magnetrons blocked by the shutters (for cleaning and preheating the targets) and ion sputter-cleaning of the substrates by applying -750 V DC bias to the substrate table.

Reference List to Section 3

1. Choy, K. L. *Progress in Materials Science* 48 **2003** 57-170
2. Edison, T. *US Patent No. 526147*
3. Kimblin, C. *Journal of Applied Physics* 45 **1974** 5253
4. Martin, P. *Vacuum* 36 **1986** 585
5. Anders, S., Anders, A., and Brown, I. *Journal of Applied Physics* 74 6 **1993** 4239-4241
6. Aksenov, I., Belous, V., Padalka, V., and Khoroshkikh, V. *Soviet Journal of Plasma Physics* 4 **1978** 425
7. Anders, S., Anders, A., and Brown, I. *Journal of Applied Physics* 75 10 **1994** 4895-4899
8. Anders, A., Anders, S., and Brown, I. *Plasma Sources Science and Technology* 4 **1995** 1-12
9. Bilek, M. and Anders, A. *Plasma Sources Science and Technology* 8 **1999** 488-493
10. Tay, B., You, G., Lau, S., and Shi, X. *Surface and Coatings Technology* 133-134 **2000** 593-597
11. Zhang, T., Kwok, D., Chu, K., and Brown, I. *Journal of Applied Physics* 89 1 **2001** 672-675
12. Tao, Z., Jun-Da, H., Bay-Yin, T., Chu, P., and Brown, I. *Chinese Physics* 10 5 **2001** 424-428
13. Fruth, W., Meerkamm, H., Krumpiegl, T., Schaufler, C., Erkens, G., and Ruttor, M. *Surface and Coatings Technology* vol.120-121 **1999** 470-475
14. Zhang, T., Chu, P., Fu, R., and Brown, I. *Journal of Physics D* 35 **2002** 3176-3180
15. Witke, T., Schuelke, T., Schultrich, B., Siemroth, P., and Vetter, J. *Surface and Coatings Technology* 126 **2000** 81-88

16. Grove, W. *Philosophical Transactions of the Royal Society* B142 **1852** 87

17. Penning, F. *Physica (Utrecht)* 3 **1936** 873

18. Penning, F. *US Patent 2146025*

19. Knauer, W. *US Patent 3216652*

20. Clarke, P. *US Patent 3616450*

21. Penfold, A. and Thornton, J. *US Patent 3884793*

22. Thornton, J. and Penfold, A. *US Patent 3995187*

23. Corbani, J. *US Patent 3878085*

24. Chapin, J. *Research and Development* 25 1 **1974** 37

25. Chapin, J. *US patent 4166018*

26. Windows, B. and Savvides, N. *Journal of Vacuum Science and Technology A* A4 3 **1986** 453

Section 4. Definition of the methods for studying of the structure and the chemical composition of the coatings

4.1. TEM basics

According to the classical Raleigh criterion that applies for light microscopy, the smallest distance between adjacent points that can be resolved by a light microscope **δ_d**, also called resolution due to diffraction, is

$$\delta_d = \frac{0.61\lambda}{\mu \sin\beta} = 0.61\frac{\lambda}{\alpha} \quad (4.1)$$

Where **λ** is the wavelength, **μ** is the refractive index of the viewing medium and **β** is the semi-angle of collection of the magnifying lens. With good preciseness the denominator **α** (also called numerical aperture) can be approximated to unity. Thus the resolution is roughly equal to half of the wavelength of the light used. For green light, for example, that is in the middle of the visible spectrum, the resolution of a good optical microscope can not exceed 300 nm. Overcoming this limit has been the main motivation for Knoll and Ruska who initially developed the idea of using electrons and electron lenses for imaging. They introduced the term “electron microscope”, built the instrument and demonstrated electron images taken with it in [1]. For this contribution Ruska received, with a big delay, the Nobel Prize for physics in 1986. It is interesting to mention that Ruska revealed that at the time he contributed to the invention of the TEM, he had not been aware about the ideas of de Broglie about the wave nature of the electrons. So Ruska thought that the wavelength limit does not apply for electrons. In fact it does. According to de Broglie, the electrons have dual nature and posses the characteristics of both particles (mass and charge) and waves (wavelength). The relation between these characteristics is as follows

$$\lambda = \frac{h}{m_0 v} \quad (4.2)$$

Where **λ** is the electron wavelength, **m_0** is the electron rest mass and **v** is the speed of motion

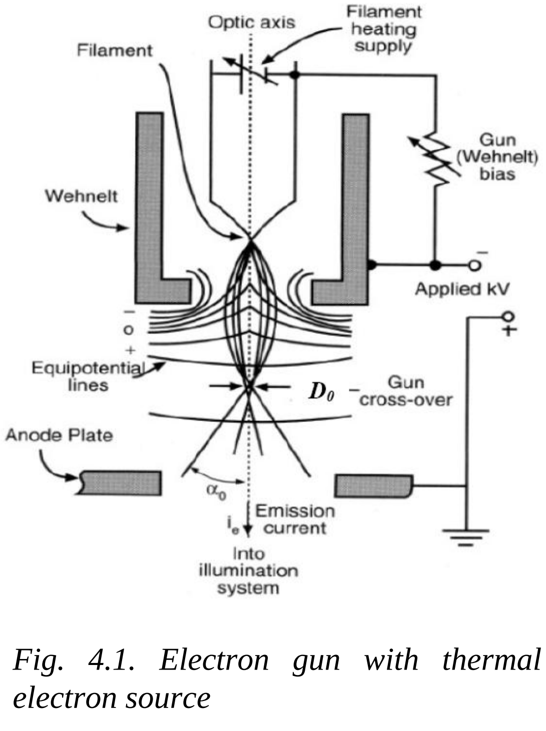

Fig. 4.1. Electron gun with thermal electron source

of the electron. In a TEM the electrons are accelerated by a device shown on Figure 4.1 and called electron gun. Electrons can be emitted by thermoelectron emission or field emission. The first is realized by heating a W filament or a LaB_6 monocrystal and the latter is realized by applying high voltage to a W needle. The potential difference between the Wenhelt and the anode plate is called accelerating voltage. The kinetic energy that an electron acquires in an electron gun is

$$\frac{1}{2}m_0v^2 = eV \textit{ (4.3)}$$

Where e is the electron charge and V is the accelerating voltage. Combining (4.2) and (4.3.) we obtain

$$\lambda = \frac{h}{\sqrt{2m_0eV}} \textit{ (4.4)}$$

In a modern TEM operating with accelerating voltage of 200 kV and more, the electrons acquire substantial speed and their mass, according to the theory of relativity, increases and a relativistic correction is to be introduced. Finally, taking into account the relativistic correction,

$$\lambda = \frac{h}{\sqrt{2m_0eV(1+eV/m_0c^2)}} \textit{ (4.5)}$$

Where **c** is the speed of light in vacuum. For example, for accelerating voltage of 200 kV λ=0.00251 nm.

The trajectory of a charged particle, which an electron is, can be influenced by either magnetic or electric field. In TEMs magnetic fields are used because of the difficulties related with the intense electric fields needed for deflecting accelerated electrons, among which is charging of the specimen, arcing and so on. So instead of glass lenses which is the case in light microscopy, TEMs use magnetic lenses. The motion of an electron in a magnetic field obeys the right-hand rule and is shown on Figure 4.2.

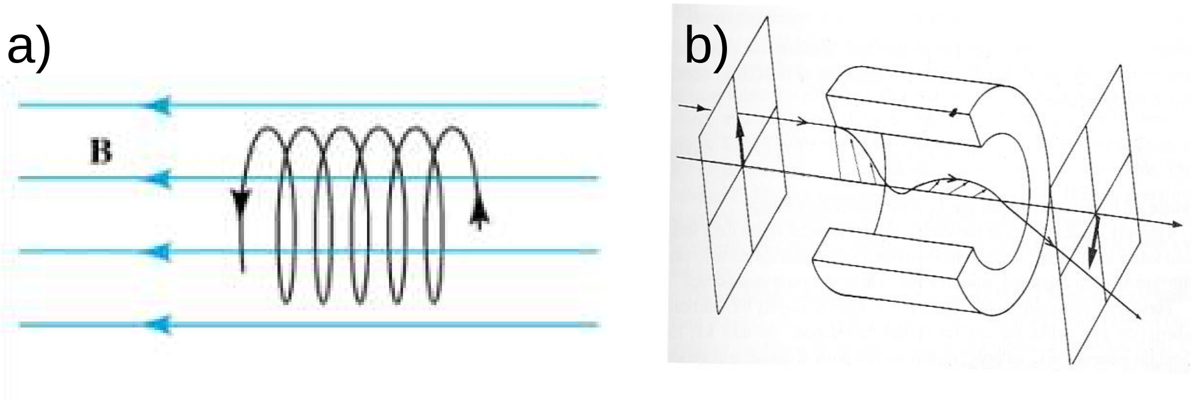

Fig. 4.2. Spiral motion of an electron in a) magnetic field and b) a magnetic lens

For this reason, in contrast with the optical microscopes, the image in a TEM is always rotated relative to the specimen and the degree of rotation depends on the strength of the lens, i.e. on the magnification. A schematic of a magnetic lens is shown on Figure 4.3.

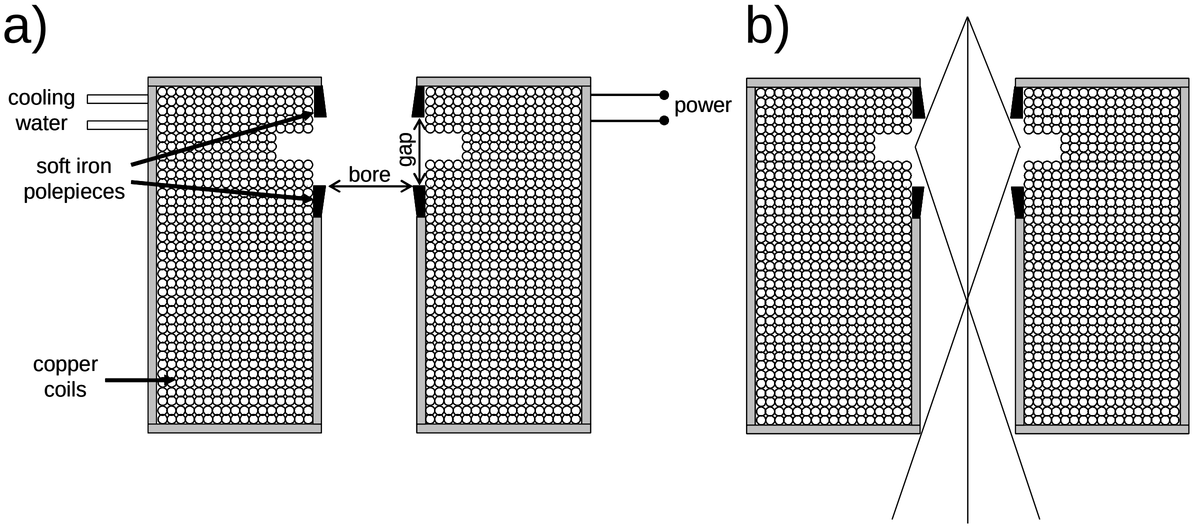

Fig. 4.3. a) magnetic electron lens; b) electron beam path through the polepiece

The current fed through the copper coils creates a magnetic field which is shaped by the polepieces. The electrons passing through the magnetic field in the gap between the polepieces are redirected in a way described in the figure. By varying the current through the coils one can vary the strength of the lens. While nowadays almost perfect lenses can be manufactured for light microscopy, even the best magnetic lens is very far away from being perfect. Using a magnetic lens for electron microscopy can be compared to using the bottom of a glass bottle for light microscopy. In other words, the resolution of a TEM is limited not by the wavelength of the electrons used but by the imperfections (mainly the spherical aberration) in the lenses that are used to create the electron image. The main defect of a magnetic lens is the so-called spherical aberration and is shown on Figure 4.4.

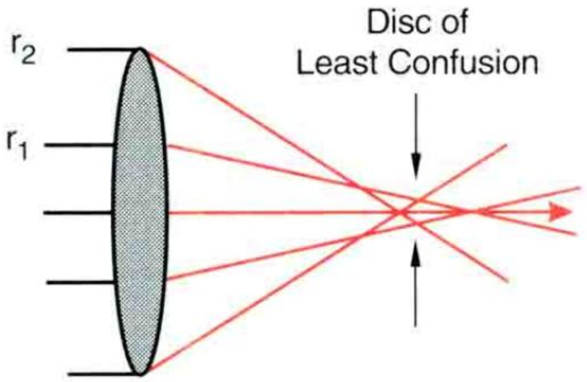

Fig. 4.4. Origin of the spherical aberration in a lens

The spherical aberration of a lens is due to radial-uneven strength of the lens. Thus rays passing through the periphery of the lens are refracted more strongly than the rays passing through it central part. The quality of the image produced by a lens with spherical aberration is highest in the so-called disk of least confusion where the sum of the image distortions is minimal. One possible way to minimize the spherical aberration is to collect a very narrow part of the rays, close to the optical axis of the lens. This is the reason for the very small semi-angles of collection β in a TEM, being typically a fraction of a degree and the resolution limit δ_s of a TEM due to spherical aberration is given by

$$\delta_s = C_s \alpha^3 \, (4.6)$$

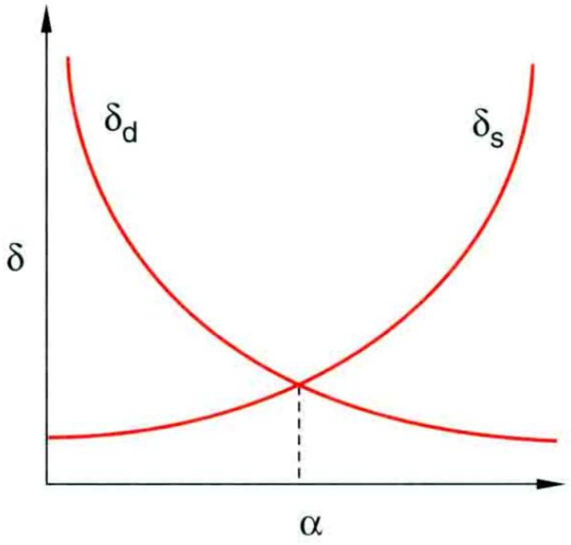

Fig. 4.5. Optimum combination of the values for δ_d and δ_s results in minimum α

Where $\mathbf{C_s}$ is the spherical aberration coefficient of the lens. The overall instrument resolution is then

$$\delta = \sqrt{\delta_s + \delta_d} = \sqrt{C_s \alpha^3 + 0.61\lambda / \alpha} \, (4.7)$$

Since magnetic lens with smaller C_s can not be made currently, the only way to increase the resolution of a TEM is to decrease λ by increasing the accelerating voltage. This is also limited by technical difficulties and increasing probability for electron beam-induced damage of the specimen. The dependence of δ_s and δ_d on α is represented graphically on Figure 4.5. Optimum value of α occurs when δ_s=δ_d. Then

$$\alpha^4 = 0.61 \lambda C_s \, (4.8)$$

One year after Knoll and Ruska built their microscope the resolution of the light microscope was surpassed and constantly improved through the years until individual atomic columns were observed for the first time in the middle of the 1970s. Nowadays a TEM has a typical resolution of about 0.15 nm. Because this resolution is sufficient for studying the atomic structure of the materials by imaging, improving the resolution of the TEM is not a paramount and the instrument is currently being developed in other directions.

The optical configuration of a TEM is shown on Figure 4.6. Since electrons interact very strongly with matter (including scattering from gasses), TEMs operate in vacuum. The mean free path of an electron should be greater than the electron gun-viewing media distance.

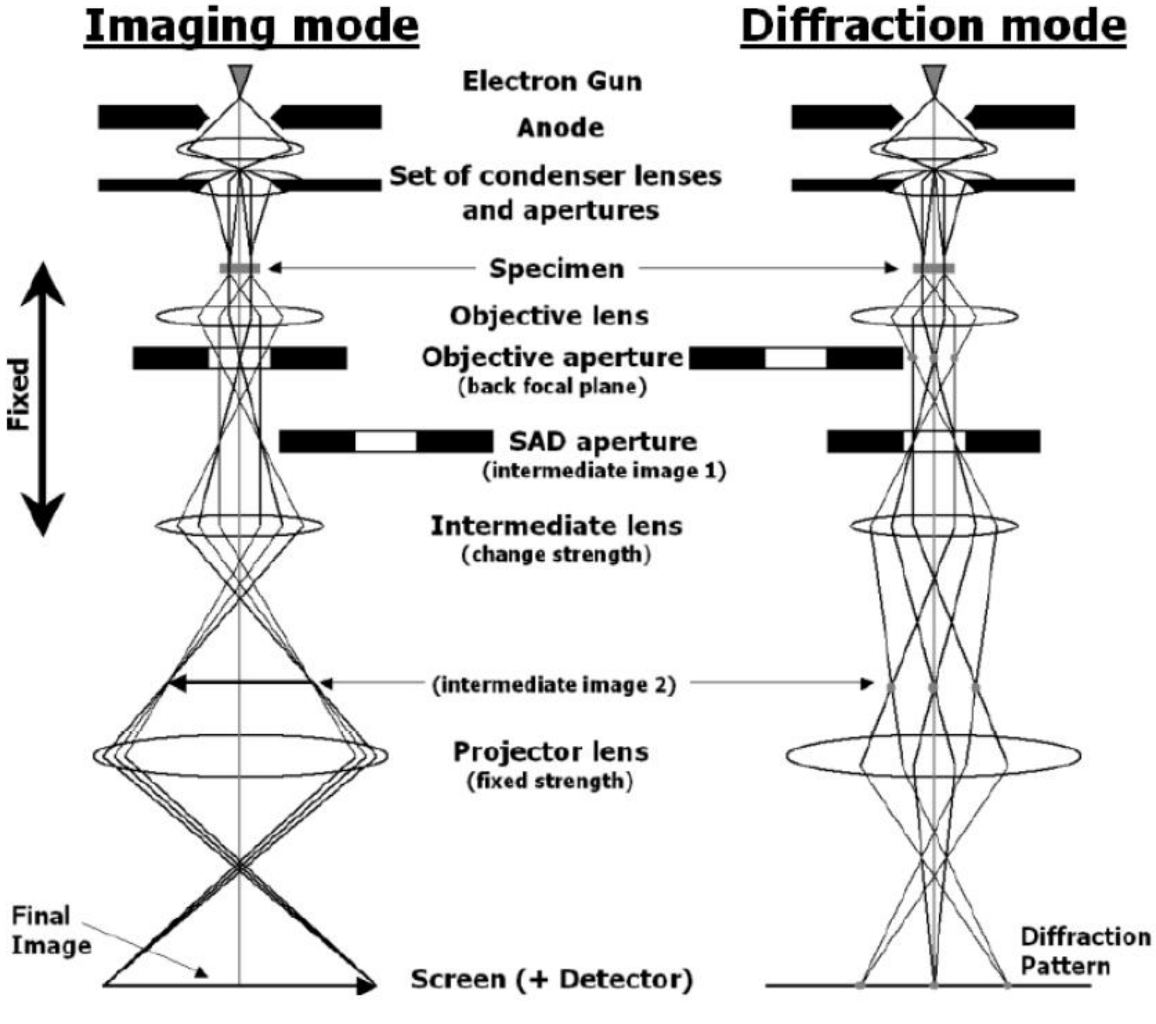

Fig. 4.6. Ray diagram of a TEM in imaging and diffraction mode. Note the difference in the objective and selected area diffraction (SAD) apertures and also the strength of the intermediate lens in both cases

Vacuum also prevents arcing in the electron gun and contamination/oxidation of the sample during observation. In principle a TEM consists of 2 main optical subsystems: illumination system that provides the electron beam arriving at the specimen with the desired characteristics and imaging system that brings the electrons transmitted through the specimen onto the appropriate imaging detector. The current illumination systems are capable of producing electron beams only few Å in diameter thus allowing analysis of very small regions of the specimen to be made. As seen from the figure, a TEM has two basic operation modes: imaging and diffraction. In imaging mode, the strength of the intermediate lens is such that it focuses into one point the beams scattered from the same point of the specimen. In diffraction mode the strength of the intermediate lens (often called diffraction lens) is such that it focuses in one point the beams scattered from the specimen at the same direction (i.e. the parallel beams leaving the specimen). This is the main difference between the two operation modes of a TEM.

4.2. Diffraction

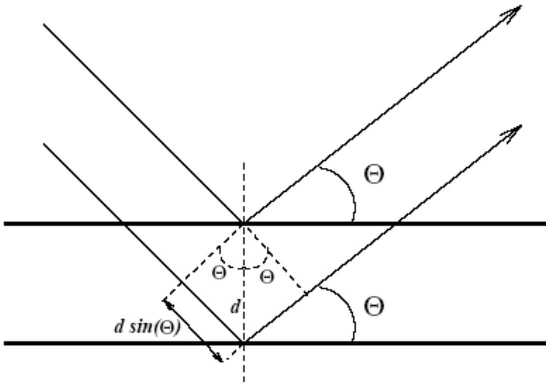

Fig. 4.7. Electron reflection from crystal planes.

Crystal lattices are good diffraction grids for the electrons used in a TEM due to the small wavelength of the latter. As it is with X-ray diffraction, electron diffraction is governed by the same basic geometrical law known as Bragg’s law. The Bragg’s law is schematically represented on Figure 4.7. The electron wave front reaches the crystal planes and is reflected by them. The difference in paths **Δ** passed by beams reflected by neighboring planes is

$$\Delta = 2d\sin\Theta \, (4.9)$$

Constructive interference between the reflected beams occur when **Δ** equals an integer number of wavelengths:

$$\Delta = n\lambda = 2d\sin\Theta \, (4.10)$$

or

$$n\lambda = 2d\sin\Theta \, (4.11)$$

or

$$d = \frac{n\lambda}{2\sin\Theta} \quad (4.12)$$

In other words, the interplanar distance **d** can be calculated by the angle at which these planes diffract the electron beam with given wavelength **λ**. Since in a TEM the electron beam is monochromatic, it is diffracted by the interplanar distances characteristic for the crystalline specimen at specific angles corresponding to that distances through the Bragg's law. On the imaging device the diffracted beam forms an image known as electron diffraction pattern. For the case of a monocrystalline specimen the electron diffraction pattern looks like the one shown on Figure 4.8.

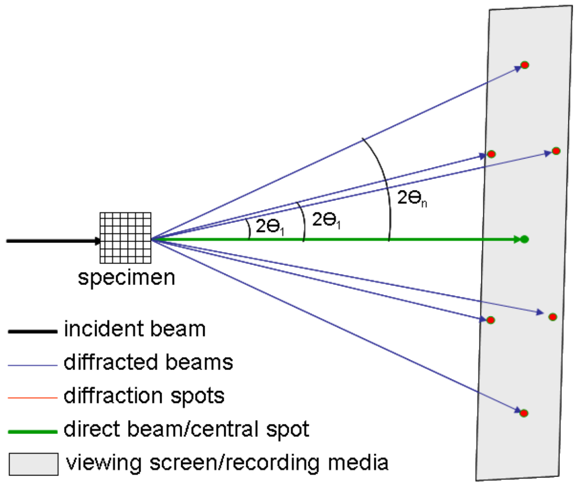

Fig. 4.8. Formation of a diffraction pattern from a monocrystalline specimen

For a polycrystalline specimen there are many crystals randomly oriented relative to the incident electron beam. This random orientation will give rise to superposition of all the beams diffracted from the individual crystallites. The resulting electron diffraction pattern for a polycrystalline specimen is shown on Figure 4.9 for the case of a completely random orientation of the crystals in the whole range 0-360°. If the crystallites are oriented randomly relative to the electron beam but only in a certain range of angles (i.e. if there is the so-called preferred orientation or texture in the specimen) the electron diffraction

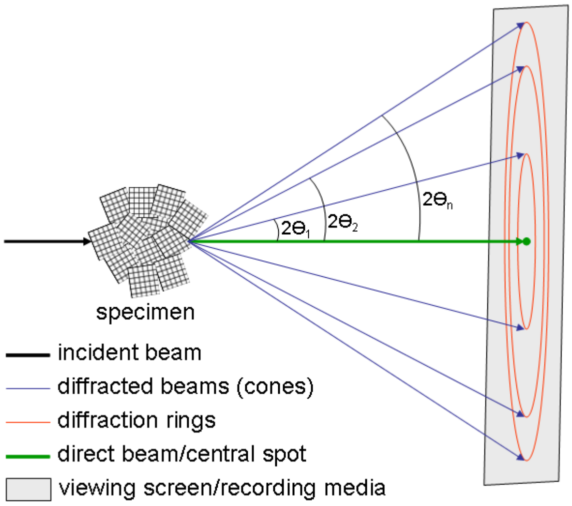

Fig. 4.9. Formation of a diffraction pattern from a polycrystalline specimen

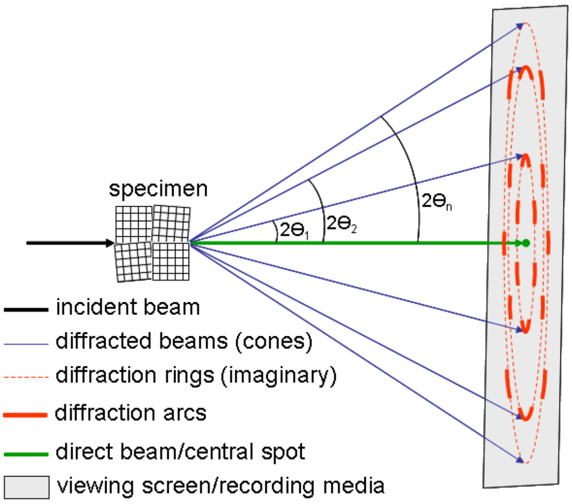

Fig. 4.10. Formation of a diffraction pattern from a textured polycrystalline specimen

pattern looks like the one shown on Figure 4.10. The angle of the arcs on that diffraction pattern corresponds to the range of the angles at which the crystals are oriented relative to the electron beam. The monocrystalline and random polycrystalline diffraction patterns can be considered the two extremes of the preferred orientation diffraction pattern.

In order to calculate the interplanar distances of the crystalline phase(s) present in the specimen, the values of $\boldsymbol{\lambda}$ and $\boldsymbol{\Theta}$ are needed. Knowing the accelerating voltage, the electron wavelength is easily calculated using equation 2.4.5. The diffraction angle cal be calculated using the concept shown on Figure 4.11.

The camera length **L** on the figure is the distance between the specimen and the recording media and in a TEM does not correspond to the physical distance between them due to the influence of the lenses. Rather, the camera length is given directly by the instrument for every given strength of the lenses. Because of the very short wavelength of the incident beam, the diffraction angles are very small, typically in the range of one to few degrees. Then it can be assumed with good preciseness that $\boldsymbol{\sin\Theta = \Theta}$. The radiuses of the diffraction rings or arcs (or the distance from the central spot to the diffraction spot for the case of monocrystalline specimen) are measured easily. By means of inserting an aperture (called diffraction aperture) in the intermediate image plane a diffraction pattern of only the region selected by the aperture can be taken. This method is called Selected Area Electron Diffraction (SAED) and

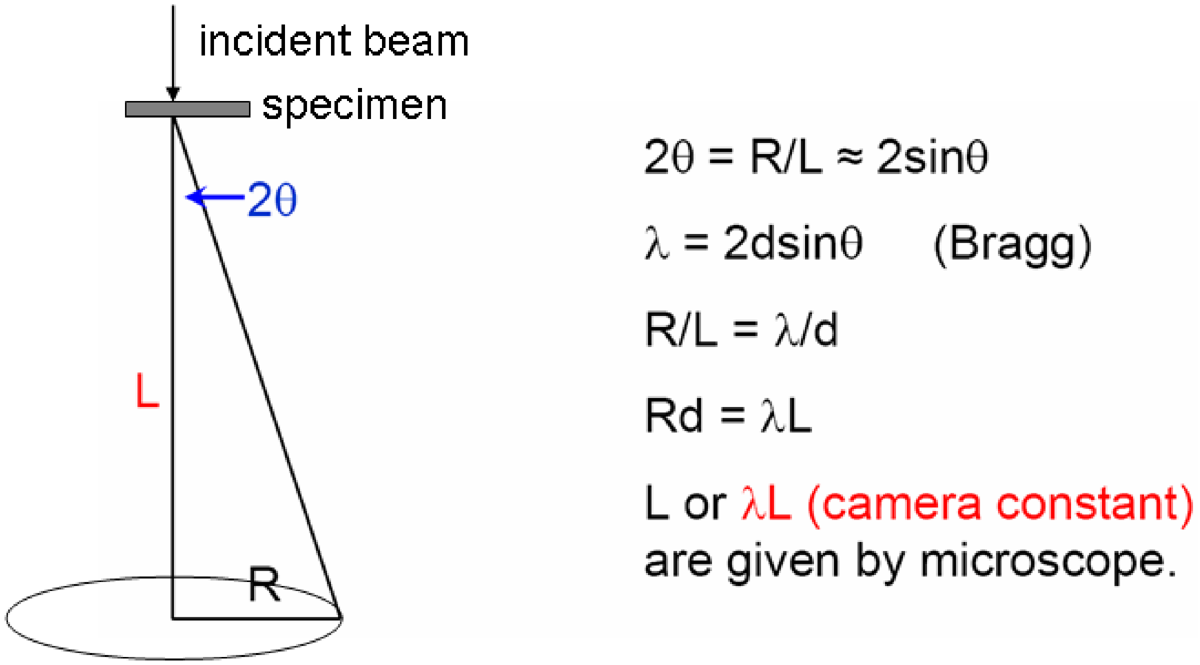

Fig. 4.11. Calculation of the TEM camera constant

is an extremely powerful technique for studying the crystalline structure of very small regions of the specimen. Unfortunately, the size of that region is limited because of the imperfections of the magnetic lenses used. Spherical aberration of the objective lens makes the actual position of the diffraction aperture differ from its position on the image. In other words, there is uncertainty in the position of the diffraction aperture so SAED pattern may be taken from different region than thought. For this reason SAED can be performed with sufficient accuracy only from regions about 200 nm in diameter. For smaller regions of the specimen other electron diffraction techniques are used which are not in the scope of this work.

4.3. Imaging

Since electrons are charged particles, their interaction with matter (especially with condensed matter, which most TEM specimens are) is very strong and generates many useful signals, as shown on Figure 4.12. Detecting these signals and relating them to the structural and chemical characteristics of the specimen extends the capabilities of a modern TEM far beyond being simply a higher resolution analogue of the light microscope. Arguably the TEM is probably the most powerful and versatile tool for studying the materials on atomic and even sub-atomic scale. The strong interaction of the electrons with condensed matter, however, is not only the blessing but also the curse of TEM because one should use very thin specimens in order to fully benefit from the high resolution of the instrument. For lattice-resolution imaging specimen thicknesses in the range of 50 nm and less depending on the average atomic weight of the specimen are only acceptable. The specimen preparation technique used in this work will be described later.

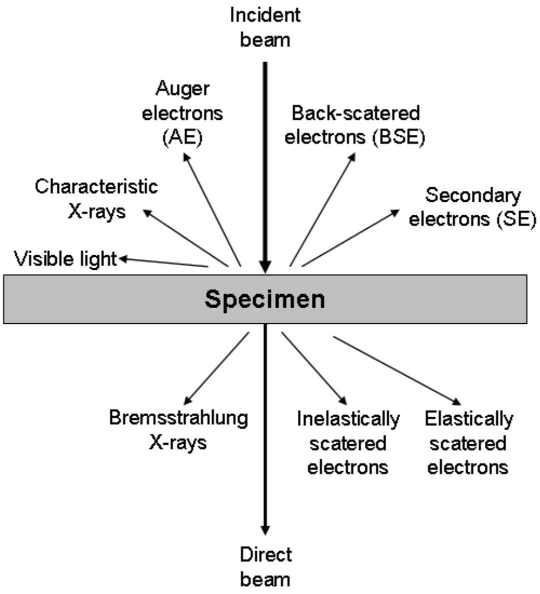

Fig. 4.12. Signals generated by the interaction of the incident beam with the specimen

From the electron-material interaction processes described in Figure 4.12 scattering is probably the most important one. It is responsible for the imaging capabilities (i.e. the ultimate purpose of a TEM) and also for studying the crystalline state of the specimen by means of electron diffraction. When an accelerated electron passes through a thin foil (specimen) of some material, there is a probability that it will scatter from its original direction. Electrons scattered in directions opposite to the incident beam are called backscattered electrons and the phenomenon is called backscattering. This signal is usually not detected in TEM but is of great importance for Scanning Electron Microscopy. The electrons scattered in the direction of the incident beam are called forward scattered electrons and the phenomenon is called forward scattering. This is by far the most useful signal in a TEM. Inelastic or elastic scattering is observed depending on whether the forward-scattered electrons have lost part of their energy or not, respectively. The overall probability for scattering is called scattering cross-section and the probability for scattering from a singe atom $\boldsymbol{\sigma_T}$ is the sum of the cross sections of the elastic $\boldsymbol{\sigma_E}$ and inelastic $\boldsymbol{\sigma_I}$ scattering from this single atom:

$$\sigma_T = \sigma_E + \sigma_I \quad (4.13)$$

For a specimen with thickness **t**, density **ρ** and average atomic weight **A** the number of scattering events per unit distance that the electron travels through the specimen **Q** is

$$Q = \frac{N_0 \sigma_T \rho}{A} \quad (4.14)$$

where $\mathbf{N_0}$ is the Avogadro’s number. If the specimen has a thickness t, then the total number of scattering events for and electron traveling through the entire specimen $\mathbf{Q_T}$ would be

$$Q_T = Qt = \frac{N_0 \sigma_T (\rho t)}{A} \quad (4.15)$$

The term **(ρt)** is called mass-thickness of the specimen. In other words, thicker and/or heavier parts of the specimen will scatter more strongly than thinner and/or lighter parts of it. This mechanism is very important for imaging in the cases of studying amorphous specimens with non uniform thickness and/or distribution of the elements. The image contrast obtained in this case is called mass-thickness contrast. In case the electron beam passes through an amorphous specimen with uniform thickness

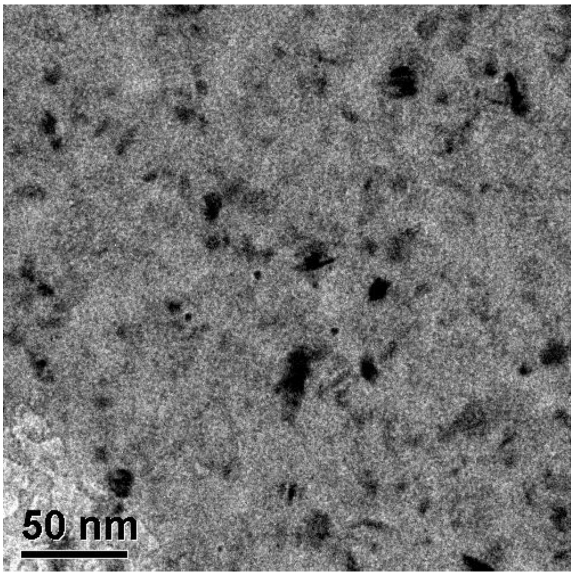

Fig. 4.13. A TEM image of a polycrystalline specimen

and uniform distribution of the elements, no contrast, i.e. no image will be formed on the viewing device. Clearly, this mechanism of contrast formation is valid also for crystalline specimens but in this case another mechanism also contributes for the image contrast. In the case of observation of a polycrystalline specimen with uniform thickness and distribution of the elements, strong contrast will be still be formed due to the fact that crystallites with different orientation will scatter (diffract) the incident beam in different (Bragg's) angles. A typical TEM image of a polycrystalline specimen is shown on Figure 4.13 where a layer of pure Si with uniform thickness is shown. The different crystallites are oriented in different angles to the incident beam and appear with different intensity on the image.

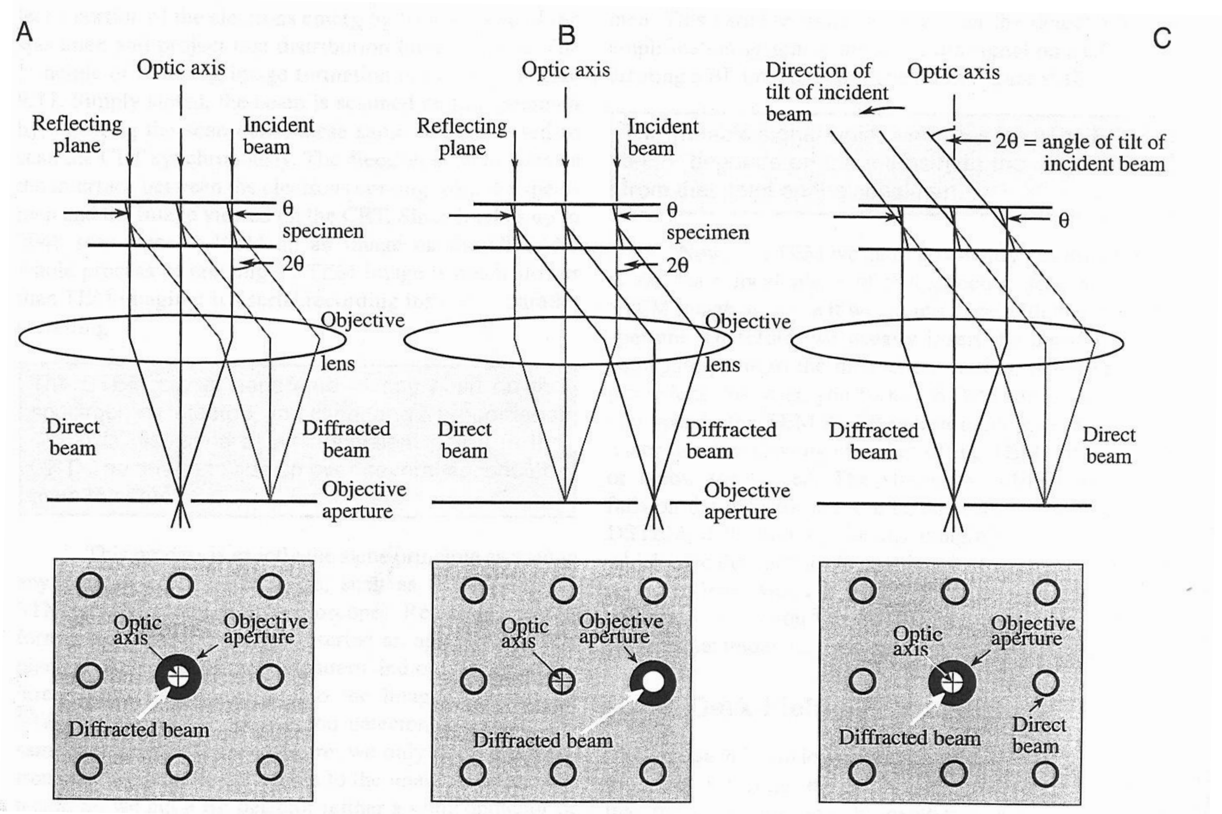

Fig. 4.14. a) bright field imaging; b) objective aperture dark field imaging; c) tilted beam dark field imaging

In the case of crystalline specimens structural features such as dislocations, vacancy clusters, grain boundaries, amorphous inclusions, etc. also contribute to contrast formation and allows their study. The two most important imaging techniques used in a TEM, the so-called bright field and dark field imaging, are shown on Figure 4.14. As seen on the figure, bright field images are formed by the electrons scattered at small angles near the direct beam (central spot on the electron diffraction pattern). In dark field imaging only electrons scattered in a randomly selected direction are used to create the image. In other words, only the electrons from a selected spot of the electron diffraction pattern form the dark field image. There are two ways to select only these electrons. In the first, the objective aperture is placed off-center in such a way that it blocks the central beam and its opening coincides with the desired direction from which the electrons are brought on the viewing device. In the second and more widely used way, the incoming beam is tilted in such a way that the beam of electrons scattered in the desired direction coincides with the optical axis of the microscope.

In practice, dark field images are formed by the following sequence of actions:

- Bringing the specimen's area of interest in the middle of the bright field image;
- Inserting a diffraction aperture so that only the area of interest is seen on the viewing device;
- Switch the microscope to diffraction mode so that SAED pattern is seen on the viewing device;
- Tilt the incident beam (specimen illumination) in such a way that the desired spot/arc/ring from the SAED pattern is in the center of the viewing device. Now the central spot is not anymore in the center;
- Switch back to imaging mode, remove the diffraction aperture and insert the objective aperture,

Dark field imaging allows only electrons scattered by particular crystalline planes to contribute to the image formation. This is a very useful technique when studying the orientation of the crystals in polycrystalline specimens. A typical bright field and dark field images from the same region of the specimen are shown on Figure 4.15.

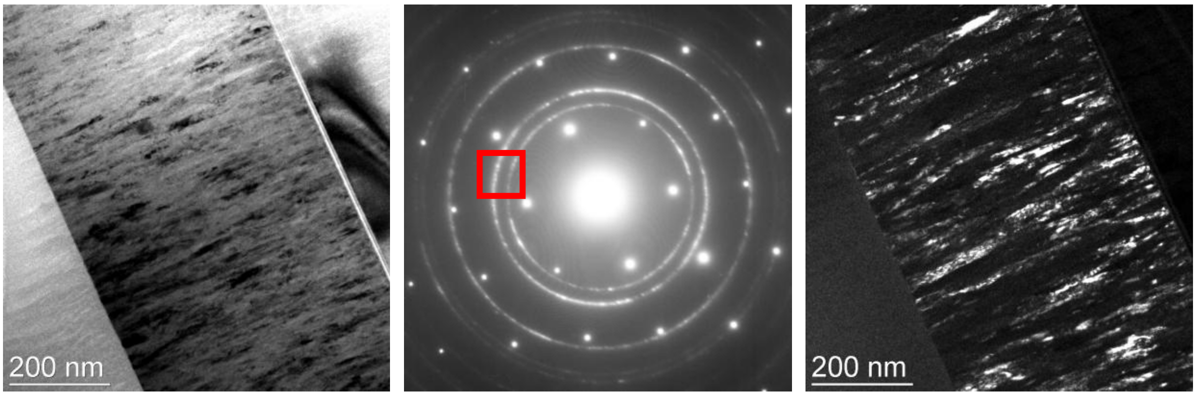

Fig. 4.15. a) a bright field image; b) the corresponding SAED pattern; c) a dark field image taken of the same region using the squared part of the SAED pattern

4.4. Image recording

In order to convert the electrons in a visible light image various devices can be used. Historically the first devices were the fluorescent screens. They are based on the fact that electron bombardment of some substances such as ZnS leads to the emission of visible light. Cathode radiation tubes of the TVs operate on the same principle. In TEMs plates coated with ZnS particles (typically 50 µm in size) are used. The ZnS is doped in order to give green light with wavelength of 550 nm. Such devices are very widely used for observation.

For recording an image special electron photographic plates were widely used. With the advance of electronics Charge-Coupled Device (CCD) cameras become more and more popular for both observation and image recording. A CCD camera can be (and usually is) connected with appropriate image-processing software. All this facilitates the work with the instrument so much that many modern TEMs have only CCD cameras and no fluorescent screens.

4.5. Spectroscopy

As seen on Figure 4.12, one of the signals generated when the incident electron beam interacts with the specimen is the so-called characteristic X-rays. When an accelerated electron collides with an atom, it can knock-off an electron from one of the inner electron shells as shown on Figure 4.16.

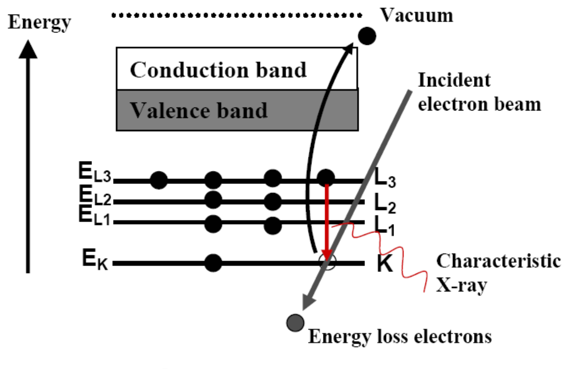

Fig. 4.16. Characteristic X-ray generation due to electron bombardment

This sets the atom in excited state which is relaxed by filling the electron hole with an electron from the outer electron shells. This electron transition emits a quantum, usually in the X-ray spectrum. The energy of this quantum is characteristic for the given transition. For example when a hole in the K-shell of a Ca atom is filled with an electron from its inner L-shell, the transition is referred to as $Ca_{K\alpha 1}$ where K denotes the shell of the filled hole, α denotes that the electron to fill the hole comes from the first neighboring shell (in this case – the L-shell) and 1 denotes that the electron comes from the first (outermost) sub-shell of the neighboring shell. A more detailed idea about the various electron transitions can be obtained from Figure 4.17.

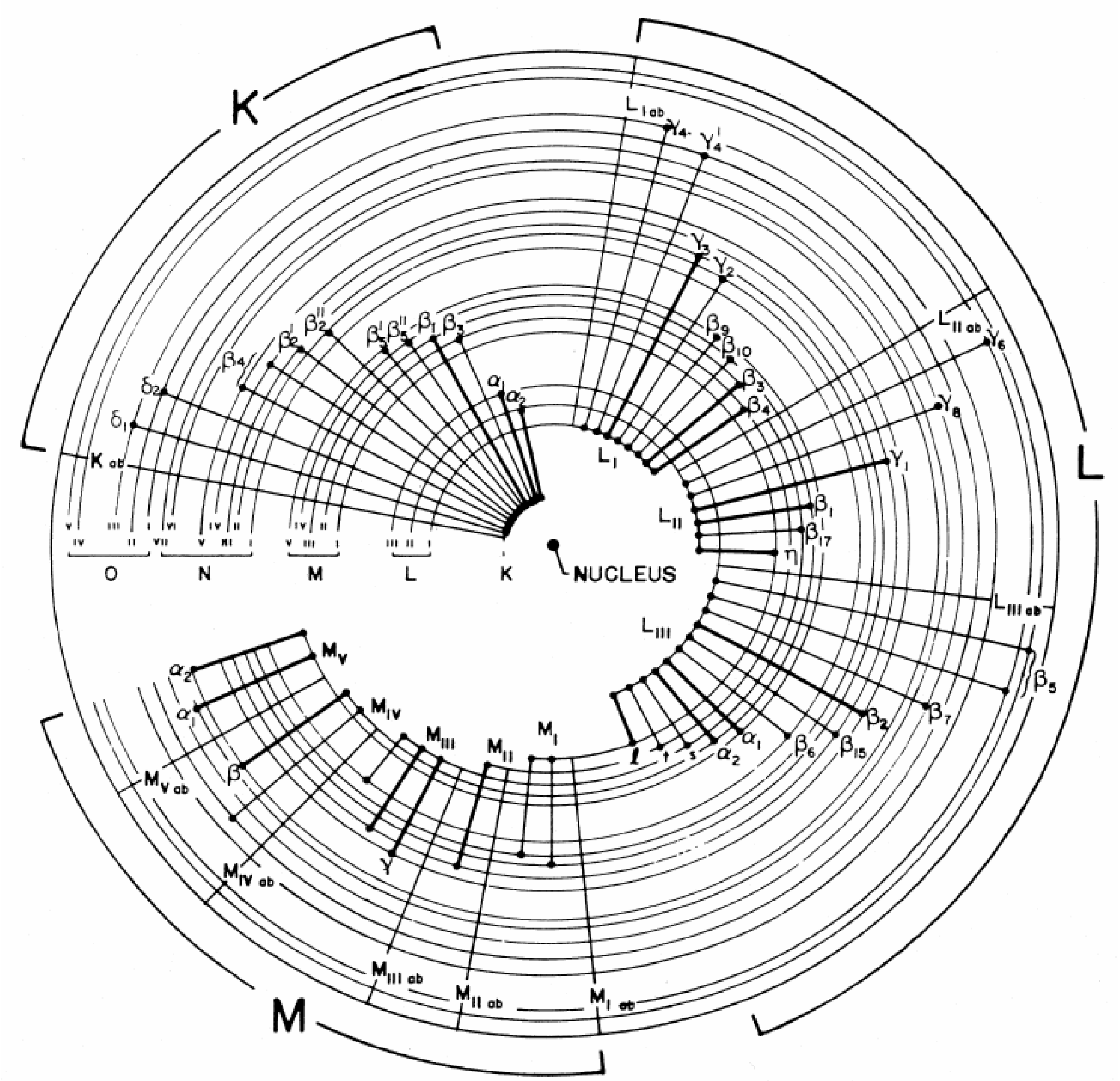

Fig. 4.17. Possible electron transitions in a relaxing atom and their designations

The $\mathrm{Ca}_{K\alpha 1}$ transition emits an X-ray quantum with energy of 3.69 keV. The energy of the transition $\mathrm{K}_{K\alpha 1}$ is 3.31 keV. The α-transitions are 7-8 times more intensive than the β-transitions. Thus every element has its own X-ray “signature” which is tabulated and this allows information of the chemical composition of the specimen to be determined. Furthermore, by using narrow electron beams, chemical analysis of very small regions of the specimen can be made. This technique is called Energy-Dispersive X-ray Spectroscopy (EDXS or, shorter, EDX or EDS). In this word the abbreviation EDX will be used. A typical EDX spectrum is shown on Figure 4.18. One disadvantage of EDX is the low sensitivity for light elements which makes quantitative analysis difficult for elements with atomic weight below 20 carbon units.

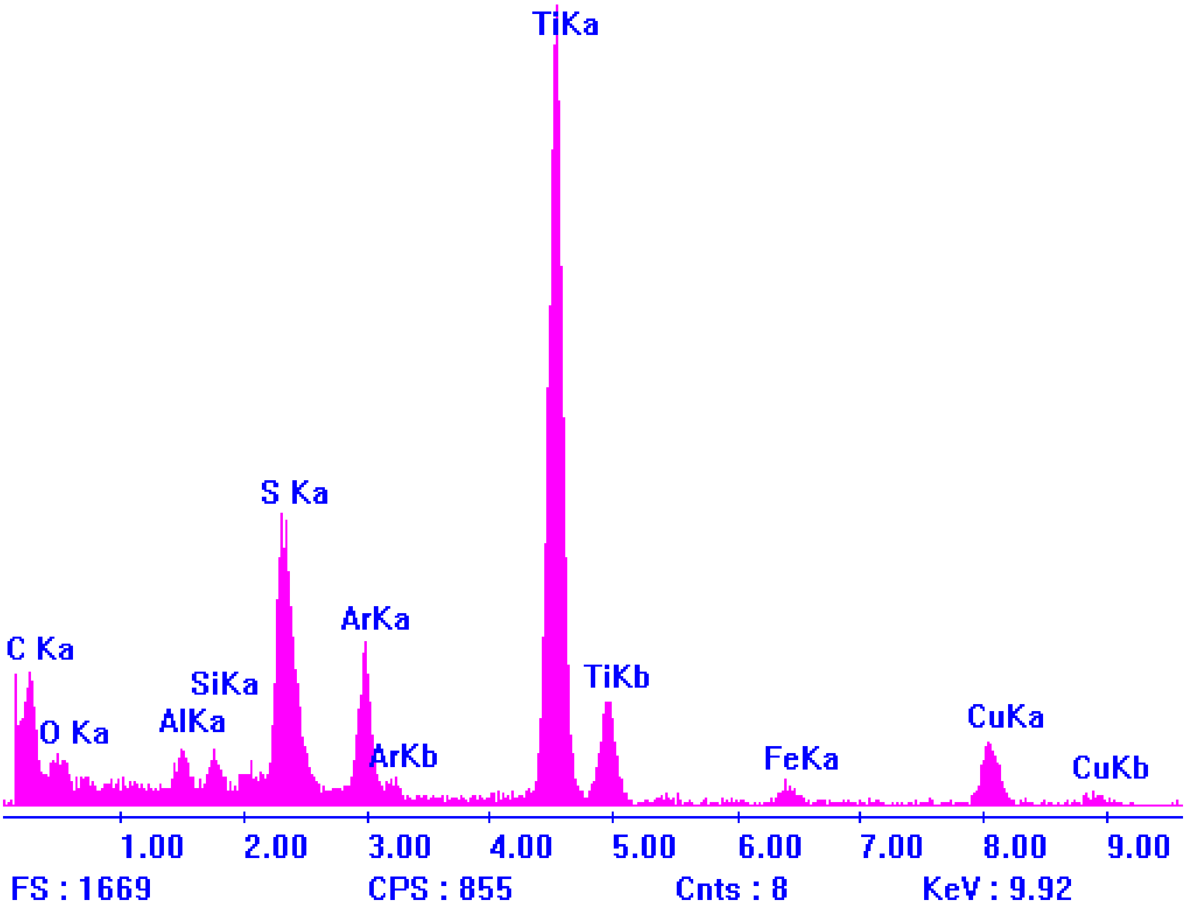

Fig. 4.18. An EDX spectrum obtained with a TEM operated at 200 kV accelerating voltage. Note the difference in intensities of the $Ti_{K\alpha}$ *and* $Ti_{K\beta}$ *lines*

4.6. Details of the TEM techniques used in this work

For studying the structure and chemical composition of the coatings that are the objective of this work, a transmission electron microscope PHILIPS CM 200 operating at 200 kV accelerating voltage is used. The instrument is equipped with EDX spectrometer allowing EDX analyses to be made. Bright field and dark field imaging, SAED and EDX were used to obtain structural and chemical information about the coatings studied. A Gatan CCD camera was used for taking the images. Gatan Digital Micrograph® software package was used to control the CCD camera and for image editing. The spots, arcs and rings in the SAED patterns have very high intensity which might damage the very sensitive CCD camera. For this reason the SAED patterns were recorded on photographic plates.

4.7. Specimen preparation

As mentioned previously, the specimens for TEM study need to be very thin due to the strong interaction of electrons with matter. For thicker specimens the following major unwanted phenomena are observed:

- Low electron image intensity: need for longer exposure times (i.e. the image might be strongly influenced by specimen drifting), higher noise level if a CCD camera is used for taking the images, lower contrast
- Overlapping of structural elements in the specimen leading to misinterpretation of the images.
- Loss of contrast.

To bring a material to a very thin (few tens of nanometers and less) foil without altering its structure and/or chemistry is a challenging task. Mechanical thinning is an obvious possibility but even before the foil becomes thin enough to be electron-transparent, it is already very sensitive to mechanical disturbance. This is especially true for brittle materials such as ceramics, semiconductors and glasses. For metals mechanically-induced structural changes (dislocation movement, recrystallization, etc.) also pose severe limits. Therefore, mechanical thinning is used mostly in the initial stage of specimen preparation when the foil is sufficiently thick and strong to withstand the mechanical stresses without being damaged. Although mechanical thinning still has been reported to give good results in some cases [2,3,4,5,6,7], it is by far not an universal method for TEM specimen preparation, especially in the case of samples with high or even moderate internal stress. To further thin the specimen to electron transparency other, non-mechanical methods are applied.

Chemical and electrochemical thinning is a non-mechanical method for TEM specimen preparation that has been successfully used for metallic materials [8]. However, this method is applicable almost only to metals and some conductive materials and is not generally suitable for ceramics, glasses and semiconductors.

Ion bombardment has proven to be a very good approach to preparing TEM specimens with large electron-transparent areas [9], [10], [11], [12], [13], [14], [15], [16]. The method is often called ion milling. Its principle of operation is shown on Figure 4.19. The surface of the specimen is controllably bombarded with accelerated ions and/or neutrals produced and accelerated by the ion guns. Neutral particles have the advantage that they do not charge

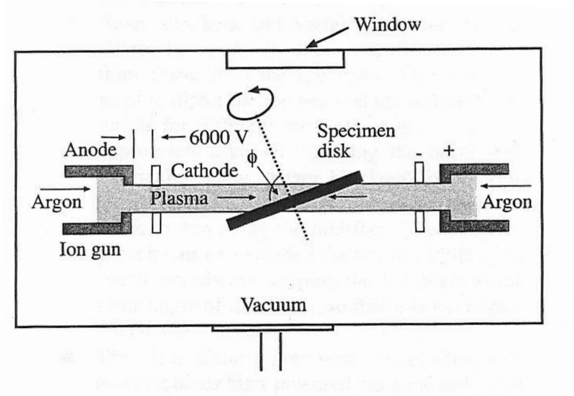

Fig. 4.19. Double beam ion milling principle

dielectric samples. However, the question whether even neutrals undergo ionization when they collide with the specimen or not is still open. As a result of these collisions, sputtering of the specimen occurs and leads to its gradual thinning. The most important process parameters are as follows:

- Accelerating voltage – typically in the range of 3-10 kV. Although such voltages provide relatively low kinetic energy of the accelerated species, substantial ion-induced surface damage (mostly amorphization) of the specimen may occur [17], [18], [19]. To minimize this damage, low-voltage ion milling has been proposed by Barna [20] with an ion gun operating at 0.1-2 kV.
- Angle of incidence – very small angles of incidence should be used, typically between 0 and 15°. Angles greater than 15° cause implantation of the sputtering species in the specimen. The amorphization also intensifies strongly with increasing angle of incidence and is small at angles below 10° [20]. Because of the low angles of incidence ion milling is very often referred to as low angle ion milling.
- Sample rocking/rotation – in order to achieve uniform sputtering of all asperities, the specimen is to be rotated/rocked during milling [18].
- Sputtering gas – Ar is probably the best choice since it is chemically neutral, its ions/atoms heavy enough to cause high rate sputtering, it does not contaminate the ion milling chamber and other hardware and is an element which does not normally exist in many materials.
- Milling time – the end of the milling process is defined mostly by the appearance of a small hole in the specimen. The edges of the hole are very thin and electron transparent. Observation of the sample and the operator's experience are the most reliable ways to interrupt the milling process in the appropriate moment although CCD cameras combined with image-processing

software to do the job are also available in the specialized ion milling equipment.

The intensive ion bombardment may introduce some artifacts in the specimen the researcher should be well aware of. Implantation, amorphisation and changes (chemical and/or structural) are some of the most important ones. To minimize the heating of the sample, cooling is sometimes necessary for temperature-sensitive samples.

In the current work the specimens were prepared by means of mechanical thinning followed by low-angle ion milling to electron transparency.

4.7.1. Mechanical thinning

"Sandwiches" of 0.3 mm thick polished Si(100) wafer substrates with the coatings to be studied were made according to a procedure shown on Figure 4.20. Transparent thermal-curing epoxy was used as a glue. The resulting "sandwiches" were then cut into the shape shown on Figure 4.21 by means of a diamond wire saw. The width of the sandwich of 2.5 mm has turned out to adequately match the capabilities of the specimen holder. The thickness of the sandwich is determined by the thickness of the Si(100) substrates and is approximately 0.65 mm. The height of the sandwich is not so critical and is dictated mostly by convenience of handling. It was found that height of approximately 10 mm is completely sufficient. A special device called tripod and shown on Figure 4.22 is used for mechanical polishing of the specimen. The sandwich obtained is glued

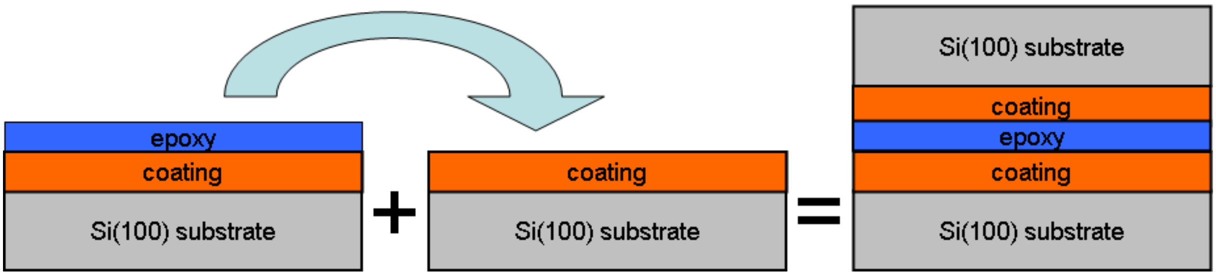

Fig. 4.20. Coated Si(100) wafer "sandwich" preparation procedure

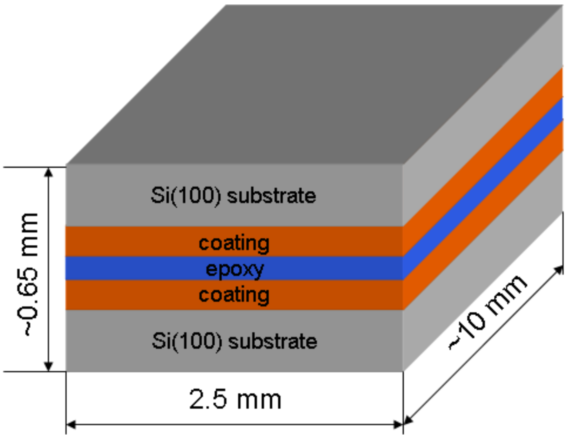

Fig. 4.21. Coated Si(100) wafer "sandwich" architecture

to the glass mount of the tripod as shown on Figure 4.23. The 2.5 x 0.65 mm face of the sandwich is then ground with several diamond grit sandpapers with grit size decreasing as shown on Table 4.1.

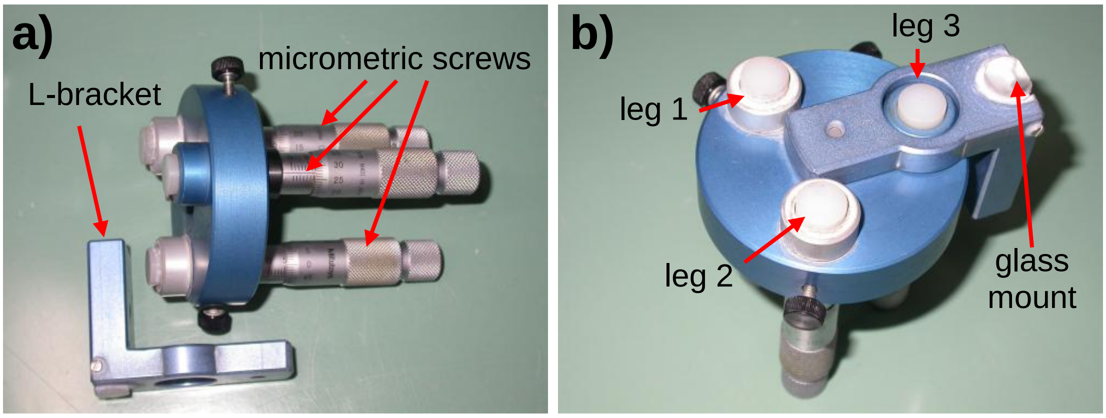

Fig. 4.22. A tripod with a) the L-bracket removed; b) fully assembled

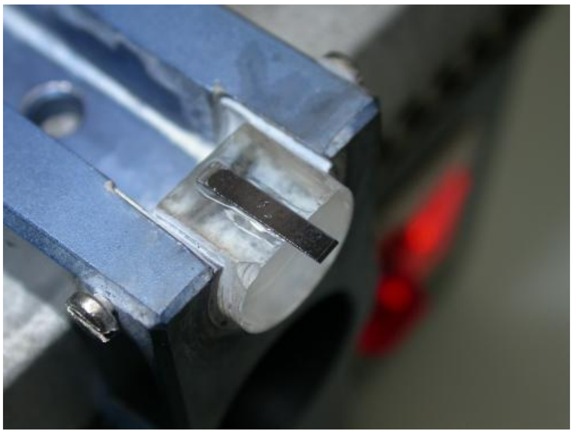

Fig. 4.23. Mounting of the "sandwich" for the first stage of the mechanical polishing. The surface of the sandwich that is to be polished faces down-right

Diamond sandpaper grit size, μm	**Specimen thickness to be removed**
30	150
15	100
6	50
3	20
1	10
0.5	10

Table 4.1. Diamond sandpaper grit sizes used

Initially, all three legs of the tripod are brought into one plane with the face of the sandwich to be ground. This is made by putting the tripod on a leveled plain surface, retracting the third leg completely and bringing the two other legs and the face to be ground in a horizontal plane by means of the their micrometric screws. The bubble-level of the tripod is a measure for horizontality. Once this is made, the third leg is brought into contact with the leveled surface. Then, before the grinding with the 30 μm grit diamond sandpaper, the three legs are retracted with 150 μm using the micrometric screws. The grinding with 30 μm grit diamond paper starts and continues until the third leg touches the sandpaper and the sandwich stops leaving a track on the sandpaper. This means that 150 μm of the sandwich height have been removed. The sandpaper is changed to the next size, the three legs are retracted with the corresponding distance

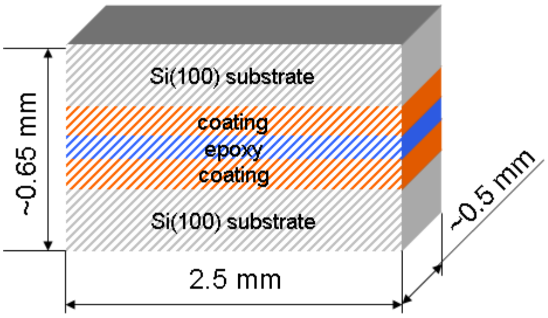

Fig. 4.24. The "sandwich" ready for the second stage of tripod polishing. The side polished in the first stage is hatched.

and the above mentioned polishing takes place until the third leg touches the sandpaper. The step is repeated until the final polishing with 0.5 µm paper is finished. Then the polishing wheel is changed with a felt wheel and polishing with 30 nm particle size silica water suspension is carried out for about 2 minutes. The specimen is then rinsed very well with deionised water. Optical microscope inspection of the polished surface is made between the steps. In case chips, cracks and other defects are observed, the step is to be repeated. Only the sandpaper marks should be visible on the surface if the step is carried out properly. After the final polishing with the silica suspension, a uniform, extremely smooth surface should be seen in the microscope. Then the sandwich is removed from the glass mount and a piece of it is cut as shown on Figure 4.24 by means of a diamond wire saw. The L-bracket is mounted on the tripod and the two legs are brought into one plane with the glass mount as shown on Figure 4.25. Then the bottom of the glass mount is ground with 6 µm grit diamond sandpaper until its surface is uniformly ground and free of scratches. The goal of this procedure is to ensure that the bottom of the glass mount will be coplanar with the diamond sandpaper during the next stages of specimen thinning. The L-bracket is then removed from the tripod and the cut specimen is glued to the bottom of the glass mount with its polished side facing the glass mount as shown on Figure 4.26. Then the L-bracket is mounted back on the tripod. Then the grinding starts using diamond sandpapers in the same order as shown on Table 4.2

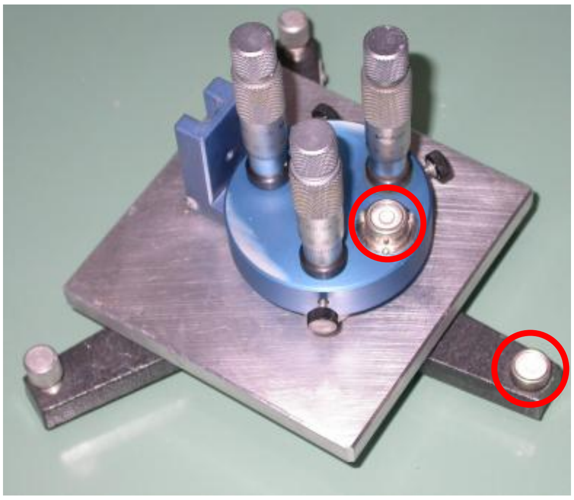

Fig. 4.25. Leveling of the tripod by means of a leveled table. The bubble-level gauges are marked with red circles

Diamond sandpaper grit size, µm	**Residual specimen thickness after grinding**

30	200
15	100
6	50
3	20 (Si becomes brown in transmission)
1	10 (Si becomes red in transmission)
0.5	Until Si is orange in transmission

Fig. 4.26. Installation of the specimen on the glass mount of the tripod for the second stage of polishing

The residual thickness of the sandwich is measured by the focus of the optical microscope and a linear displacement measurement device attached to the object table of the microscope. The final stages of grinding are controlled by the color of the sandwich in transmitted light. Grinding with 0.5 µm grit sandpaper is stopped when no scratches are observed on the surface and the sandwich is orange in transmission. Then the specimen is polished with silica suspension as described above. After polishing and rinsing with deionised water the L-bracket is removed from the tripod and placed in acetone for ungluing the specimen. Once the specimen is detached from the glass mount, it is glued to an aluminum horseshoe specimen holder by means of ARALDITE Rapide® epoxy as shown on Figure 4.27a. Prepared in such way, the specimen is ready for low angle ion milling.

Table 4.2. Diamond sandpaper grit sizes used for the second stage of polishing

4.7.2. Ion-milling

The specimen, as glued on the horseshoe holder, is installed on a titanium ion milling holder and introduced in a BALTEC RES 100 ion milling system equipped with CCD camera for specimen observation during milling. First one side of the specimen is milled with Ar^+ accelerated with 2.5 kV and 4° angle of incidence for 30 minutes. During this stage, the specimen is rocked with amplitude of 20°. This stage is needed for removing the contamination and the small scratches and pits that almost inevitably exist on this side of the specimen. Then the holder is flipped and a high angle (15°) ion milling is performed at 4 kV accelerating voltage. During milling the specimen is rocked with amplitude of 20°. This stage is needed for rough thinning of the specimen and is terminated when either a perforation occurs at or near the region with the coating (the middle of the sandwich) or the eroded "saddle" reaches the coating (the middle of the sandwich). The second case, which is more frequent, is illustrated on Figure 4.27b. The termination of this stage is decided based on optical observation of the sample during milling. The experience of the operator plays a very important role here. Once this stage is finished, the milling continues for 30 minutes at 4° angle of incidence and 2.5 kV accelerating voltage. The specimen is rocked with amplitude of 20°. The aim of this stage is to remove the amorphous layer caused by the previous, high angle and high voltage, stage and to also remove any residual asperities on the surface of the specimen. After accomplishing this stage, the specimen is ready for observation. All specimens are stored in a vacuum chamber in order to avoid or at least minimize their oxidation.

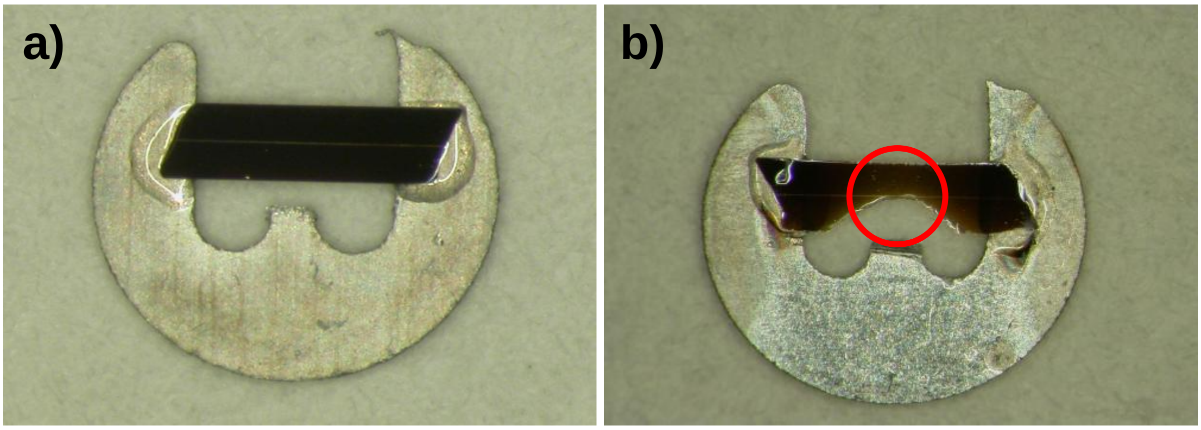

Fig. 4.27. Specimens mounted on a specimen holder a) prior to ion milling; b) after ion milling and ready for TEM study with its area of interest encircled in red

Reference List to Section 4

1. Knoll, M. and Ruska, E. *Z. Physik* 78 **1932** 318

2. Ayache, J. and Albarede, P. *Ultramicroscopy* 60 **1995** 195-206

3. Benedict, J., Anderson, R., and Klepeis, S. J. *Specimen Preparation for Transmission Electron Microscopy of Materials - III Symposium* **1992** 121-140

4. Benedict, J. P., Anderson, R., and Klepeis, S. J. *International Symposium on Electron Microscopy* **1991** 450-460

5. Benedict, J. P., Anderson, R. M., and Klepeis, S. J. *Advances and Applications in the Metallography and Characterization of Materials and Microelectronic Components. Proceedings of the Twenty-Eighth Annual Technical Meeting of the International Metallographic Society* **1996** 277-284

6. Shaapur, F. and Rimer, J. *Specimen Preparation for Transmission Electron Microscopy of Materials IV. Symposium* **1997** 181-185

7. Anderson, R. and Klepeis, S. J. *Specimen Preparation for Transmission Electron Microscopy of Materials IV. Symposium* **1997** 193-199

8. Hall, C. *Introduction to electron microscopy* **1966 McGraw-Hill, New York**

9. Radnoczi, G. and Barna, A. *Surface and Coatings Technology* 80 **1996** 89-95

10. Tsujimoto, K., Tsuji, S., Takatsuji, H., Kuroda, K., Saka, H., and Miura, N. *Specimen Preparation for Transmission Electron Microscopy of Materials IV. Symposium* **1997** 207-215

11. McCaffrey, J. P. and Barna, A. *Microscopy Research and Technique* 36 **1997** 362-367

12. Kouzaki, T., Yoshioka, K., and Ohno, E. *Specimen Preparation for Transmission Electron Microscopy of Materials IV. Symposium* **1997** 251-256

13. Grant, J. T., Walck, S. D., Scheltens, F. J., and Voevodin, A. A. *Specimen Preparation for Transmission Electron Microscopy of Materials IV. Symposium* **1997** 49-71

14. Cinibulk, M. K., Welch, J. R., and Hay, R. S. *Specimen Preparation for Transmission Electron Microscopy of Materials IV. Symposium* **1997** 3-17

15. Bugiel, E. *Specimen Preparation for Transmission Electron Microscopy of Materials IV. Symposium* **1997** 89-95

16. Anderson, R. and Kelpeis, S. J. *Specimen Preparation for Transmission Electron Microscopy of Materials IV. Symposium* **1997** 187-192

17. Barber, D. *Ultramicroscopy* 52 **1993** 101-125

18. Barna, A., Pecz, B., and Menyhard, M. *Ultramicroscopy* 70 **1998** 161-171

19. McCaffrey, J. P., Phaneuf, M., and Madsen, L. *Ultramicroscopy* 87 **2001** 97-104

20. Barna, A., Pecz, B., and Menyhard, M. *Micron* 30 **1999** 267-276

Section 5.1. Characterization of the tribological properties

As mentioned earlier, coatings with specific tribological properties such as friction and wear coefficients are the central topic of this work. For the characterization of these properties a standard Pin-On-Disk (POD) method will be used for the following reasons:

- It is very suitable for material screening, measurement of the friction and wear coefficients and wear mechanism analysis. The value for the friction coefficient is instantly provided by the testing equipment.
- The testing equipment is relatively simple, commercially available and usually software-controlled so the experimental data is easy to process.
- Although it is very difficult if not impossible to directly relate the tribological properties of a material as determined with POD tests with the tribological behavior of this material in a real application, the POD test is good in comparative analysis of the tribological properties of materials, including wear protective coatings.
- The author had direct access to a piece of equipment.

The POD method is the subject of an international interlaboratory exercise aimed at standartization under the auspices of the Versailles Project on Advanced Materials and Standards (VAMAS). The results of this exercise are published by Czichos et al. [1], [2].

The instrument that uses the POD method for the evaluation of the tribological properties of the materials is called a POD tribometer. For the sake of simplicity, in this work from now on it will be referred to as tribometer. The principle of operation of this instrument an explanatory image of the tribometer used in this work are shown on Figure 5.1.1. The counterpart can be either a ball with a certain diameter of a pin with spherical cap. It is pressed with a normal force $\mathbf{F_n}$ against the coated flat substrate by means of a dead weight. The substrate is rotated with a chosen radial speed of rotation that can be varied. The tangential speed of rotation (also known as the speed of sliding or sliding velocity) is defined by the radial speed of rotation and the offset of the counterpart from the axis of rotation. This offset is equal to the wear track radius $\mathbf{r}$ and can also be varied. The overall sliding distance is defined by the total number of revelations and the wear track radius. In order to measure the wear coefficient, the wear track is scanned with either a mechanical stylus or a laser scanner. The wear track cross section area $\mathbf{S}$ is calculated from the scan and input in the equation already familiar from Section 1:

$$K = \frac{V}{F_n.s} = \frac{2\pi r S}{F_n s}$$

where **K** is the wear coefficient, **V** is the volume of the wear track and **s** is the total sliding distance of the experiment. A scan and a SEM image of a typical abrasive wear track are shown on Figure 5.1.2.

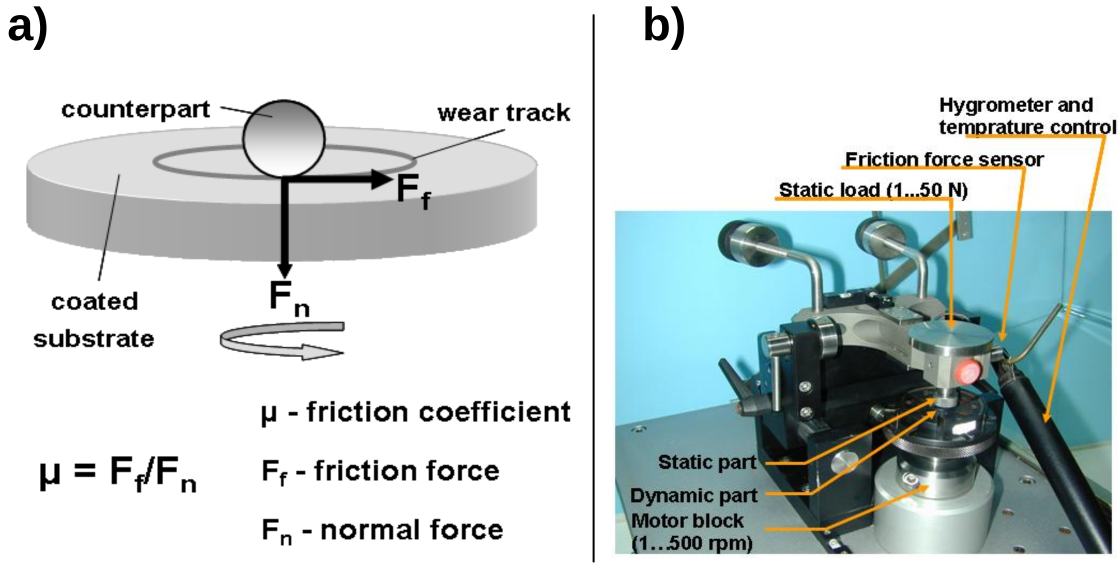

Fig. 5.1.1. a) principle of the POD test; b) the POD test instrument used in the current work

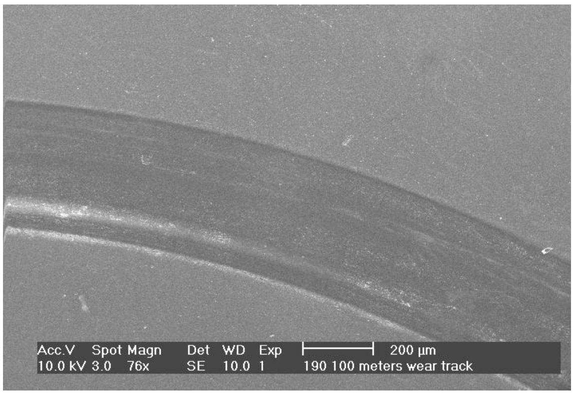

Fig. 5.1.2. A SEM image of a typical abrasive wear track

The instrument is equipped with displacement gauge attached to the counterpart holder. The latter is suspended on a spring with a known elastic constant so the friction force is calculated easily. The normal force is input in the tribometer software prior to the test and the value of the friction coefficient is given directly by the tribometer for every given moment versus the elapsed sliding distance. The graphical tribometer’s output is referred to as a friction curve and an example for it is given of Figure 5.1.3. As mentioned above, every modern tribometer is controlled by a software package and the data for the friction coefficient versus the elapsed sliding distance, number of revelations or elapsed test time is stored as an appropriate file format, usually TXT or XLS.

The counterpart material and the topography of its surface, the Relative Humidity (RH) and gas composition of the test environment (e.g. dry air, humid air, N_2, Ar, etc.), the normal force, the sliding velocity, and the wear track radius are the important parameters that need to be carefully selected for every specific case study. These factors are worth being described in a little more detail.

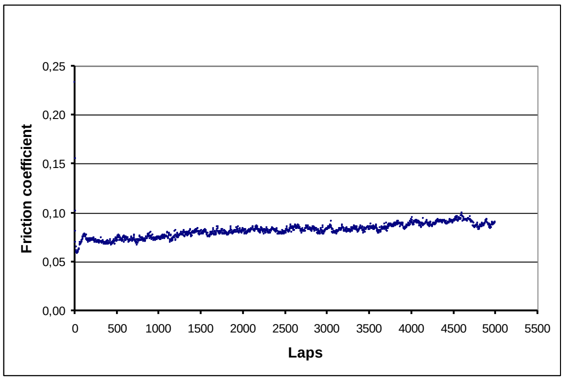

Fig. 5.1.3. A typical friction curve generated by the POD tribometer used in this work. The sliding distance is expressed in number of turns (i.e. laps)

5.1.1. Counterpart material

As mentioned earlier in this work, friction and wear depend strongly on the chemistry and topography of the sliding surfaces. If there is significant difference in the hardness of the sliding bodies, adhesive wear may take place. The harder material will be coated with the softer one thus the sliding will take place between this "transfer" layer and the counterpart. Hence, no useful information will be derived about the tribological properties of the harder surface. A wear track with such transfer layer is shown on Figure 5.1.4. If adhesion between the two surfaces is not sufficient to lead to adhesive wear, the wear of the softer body generates big amount of wear particles, also referred to as wear debris. These particles can strongly influence the friction by ploughing in the softer surface. This can also be a source of erroneous conclusions about the tribological properties of the harder material. To avoid all these unwanted influences on the interpretation of the tribological experiments data, a counterpart that meets the following requirements is to be used:

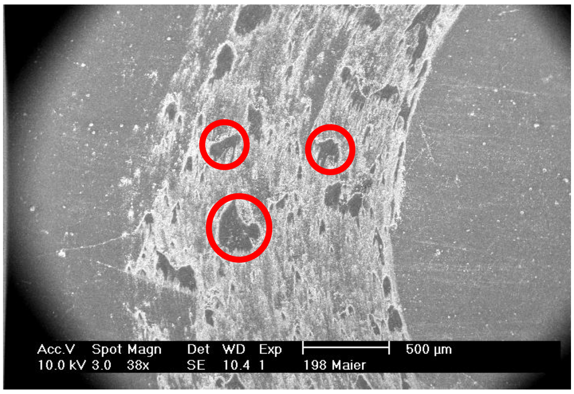

Fig. 5.1.4. A SEM image of a typical adhesive wear track in the case of steel sliding against a hard coating. The red circles show some of the islands of the transfer film from the softer steel bal counterpart

- Surface roughness as low as possible in order to minimize the effect of asperities on the friction and wear as well to minimize the generation of wear particles

- Hardness comparable to that of the coating
- Chemical inertness to minimize the possible chemical interaction with the coating
- Simple geometry and ease of manipulation
- Availability and recognition for engineering purposes.

A counterpart that meets very well these requirements is a polished polycrystalline Al_2O_3 ball with diameter of 6 mm supplied by SKF, Inc. They are used in ceramic ball bearings and are easily available with very good reproducibility of all their mechanical and chemical properties.

5.1.2. Test environment

Since most metal working processes and sliding and rolling components operate in humid air, laboratory air with controlled RH=50% was chosen for POD testing of the coatings studied in this work. In many applications the friction takes place at high temperatures and tribometers operating at these temperature range do exist. However, access to such instruments is difficult. For this reason the tests in the scope of this work were carried out at room temperature. These conditions have also been used in the VAMAS project.

5.1.3. Sliding speed

In the VAMAS project mentioned above the sliding speed has been selected to be 10 cm/s and this parameter was adopted in the current study.

5.1.4. Normal force

As mentioned above, the normal force influences the Hertzian pressure in the contact zone. In the VAMAS project the Hertzian pressure is calculated to be 1000 MPa. For an the Al_2O_3 balls used in the current work a normal force of 5 N would result in 1200 MPa Hertzian pressure which is close by value to that used in the VAMAS project. Therefore, a dead weight providing a normal force of 5 N was used in this work.

5.1.5. Wear track radius

The wear track radius was selected to be 5 mm which allows for easy measurement of the wear track cross section area.

5.1.6. Test duration and stop criterion

For the correct measurement of the wear coefficient of a coating, the wear track is to have a certain cross section area so it can be measurable with the scanning stylus. On the other hand, the coating should have not been worn in such a way that the wear track penetrates in depth to the substrate. Therefore a test stop criterion is to be carefully selected separately for each case. This criterion can be defined for the tribometer control software as number of turns (laps), sliding distance passed or test duration. In this work it is made on the basis of the trial-and-error method. 5000 laps were initially defined as a test stop criterion based on previous experience with hard coatings. Then the wear track was scanned with Rank-Taylor ruby stylus profilometer. In case the depth of the wear track was greater than 100 nm and smaller than the coating thickness, the test stop criterion was set to be 5000 laps also for the other coatings.

Reference List to Section 5.1.

1. Czichos, H., Becker, S., and Lexow, J. *Wear* 114 **1987** 109-130

2. Czichos, H., Becker, S., and Lexow, J. *Wear* 135 **1989** 171-191

Section 5.2. Characterization of the hardness

Hardness of a material is defined as its resistance towards indentation. As such, it is measured by the size of the indent that it left after indenting the studied material with an indenter with a specific and defined geometry pressed towards the studied material with a certain known force. In order to minimize the deformation of the indenter during hardness measurement, it is usually made of a material substantially harder than the material studied. The ideal indenter material is diamond and for this reason it is widely used for that purpose.

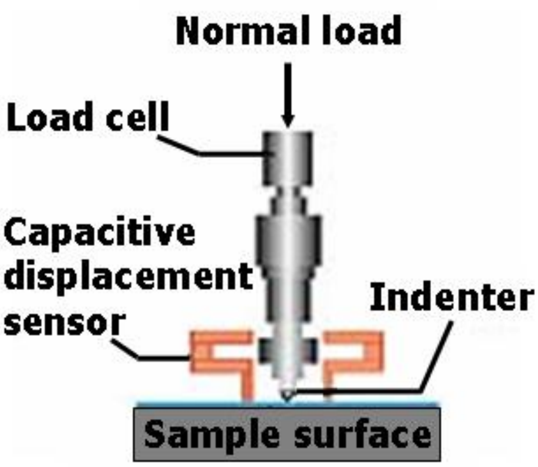

Fig. 5.2.1. NHT measurement principle

There are many indentation techniques for measuring hardness of bulk materials. However, for coatings the situation is somewhat more specific because of the small thickness of most industrially used wear protective coatings, usually varying from one up to several micrometers. The depth of indenter penetration is in this range for the most popular conventional hardness measurement methods and if they are used for determining the hardness of a coating, the hardness of the coating-substrate composite will be measured instead that of the coating itself. Development of a hardness measurement method with very small depth of penetration of the indenter was made in late 1970s and early 1980s [1], [2], [3]. The method is called Nano Hardness Test (NHT) and is very widely used for hardness measurement in coating research and development. The principle of operation of the NHT method and a Scanning Probe Microscope (SPM) image of an indent created with it are shown on Figure 5.2.1. As seen from the figure, the NHT method is very similar to the conventional hardness measurement methods with the only difference that very small loads and penetration depths are used. The studies of Ohmura et al. have clearly demonstrated that the penetration depth should be maximum 20% and 10% of the coating thickness for metallic (i.e. relatively soft, such as Al, Au and Pt) and ceramic (i.e. hard such as TiN) coatings, respectively, in order to avoid interference from the substrate [4], [5]. For hard coatings with thickness in the range of 1-5 µm the maximum penetration depths should be in the range of 100-500 nm. Such penetration depths correspond to loads in the range of 0.1-30 mN. Consequently, the equipment to realize and precisely measure these loads and penetration depths is very sensitive and more sophisticated than that used for conventional hardness measurement methods. Special care should be taken to insulate the instrument from possible interference from the laboratory environment such as vibrations (including sound), temperature and humidity fluctuations and even radio signals. The following test parameters are defined by the operator:

- Final load
- Loading rate
- Multiple indents – since the surface of the coating may contain macroparticles, pores or other defects, several indentations are normally made and the results from them are averaged. Thus a spatial indentation "matrix" can be made and its shape (for example for 10 indentations it can be 2x5, 5x2, 10x1 or 1x10 elements) as well as the space between its elements (indentations) can be defined.

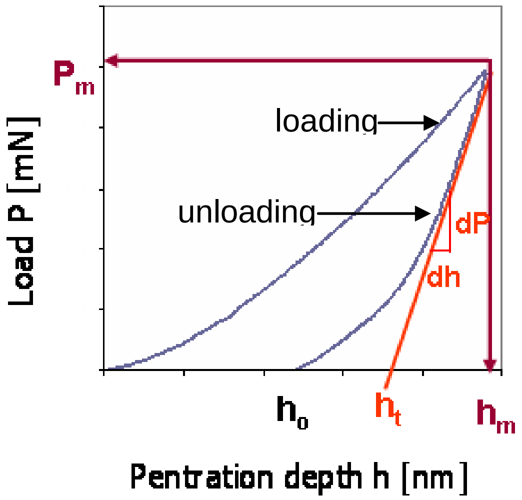

Fig. 5.2.2. A typical NHT load-displacement curve

The instrument is computer-controlled and the result of the measurement is given as a the so-called load-displacement curve shown on Figure 5.2.2. where the term “displacement” denotes simply the penetration depth as measured by the displacement sensor of the instrument. The indenter that is used for NHT is known as Berkovich indenter and its geometry is as well as an AFM image of an indent made with it are shown on Figure 5.2.3. The triangular pyramid is relatively easy to obtain with reproducible geometry and thus the Berkovich indenter is a standard that is used for coating characterization. As mentioned above, diamond is the best material for manufacturing of such indenters because of its unsurpassed hardness so the indenters are almost always made of diamond. The hardness of the coating **H** is calculated as

$$H = \frac{kP_m}{{h_m}^2}$$

Where **k** is a dimensionless constant related to the geometry of indenter (for Berkovich indenter k = 0.0408), $\mathbf{P_m}$ is the maximum load and $\mathbf{h_m}$ is the maximum penetration depth. The hardness has a dimension of pressure and is therefore expressed in Pa or, more frequently, as GPa.

Using NHT not only the hardness but also many other coating parameters can be studied. However, they are not germane for the scope of this work.

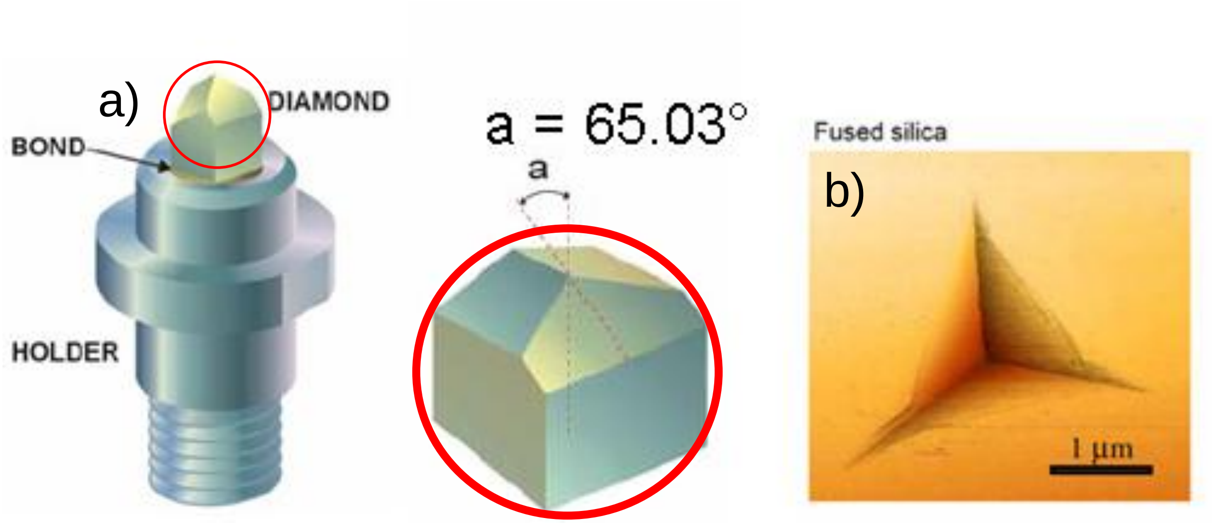

Fig. 5.2.3 a) Berkovich indenter; b) an AFM image of an indent made with it in polished fused silica

Summary of Section 5.2.

A CSM Instruments nanohardness tester equipped with a diamond Berkovich indenter was used for all hardness measurements. Load of 5 mN was used for all indentations. This value was selected experimentally so that in all cases the penetration depth does not exceed 1/10 of the coating thickness. The loading rate was 10 mN/min. Prior to and after each test, calibration of the instrument was made with a polished fused silica specimen with known hardness of 12 GPa. The standard deviation from this value was in the range of 1 GPa which is considered acceptable. For every specimen a matrix of 10 (5x2) indentations was realized with distance of 50 μm between the indentations. The hardness was averaged over the values obtained from all 10 measurements. Then these with deviation of more than 20% from the average value were excluded and the final value of the coating hardness was the average of the remaining (minimum 5) measurement results.

Reference List to Section 5.2.

1. Nishibori, K. and Kinoshita, K. *Thin Solid Films* 48 **1978** 325
2. Newey, D., Wilkins, M., and Pollock, H. *Journal of of Physics E* 15 **1982** 119
3. Petnica, J., Hutchings, R., and Oliver, W. *Philosophical Magazine A* 48 **1983** 593

4. Ohmura, T., Matsuoka, S., Tanaka, K., and Yoshida, T. *Thin Solid Films* 385 **2001** 198-204

5. Ohmura, T. and Matsuoka, S. *Surface & Coatings Technology* 169-170 **2003** 728-731

Section 5.3. Characterisation of the adhesion

Adhesion of a coating to the substrate is a parameter of the coating-substrate composite that has a very strong influence on its wear-protective properties. Schönjahn et al. demonstrated that adhesion of a coating is in direct relation with the lifetime of the coated tool [1]. Therefore adhesion is one of the coating parameters that are to be addressed when new coatings are developed. Formally, the adhesion strength is defined as the force per unit area needed for detaching the coating from the substrate also known as pull-off force. This parameter, however, is rarely equal to the actual adhesion of the coating, i.e. the strength of the interface between the coating and the substrate. In most cases the pull-off force value is smaller than the actual adhesion. For example, a coating with actual adhesion of 100 MPa may be pulled-off applying a force of only half of that value or less due to the fact that in most wear protective coatings intrinsic stresses exist. Thus the actual adhesion is counteracted by a very complex combination of the stress in the coating and the pull-off force. One of the factors that influence the amount of intrinsic stress in the coating is the coating thickness. Thus thicker coatings accumulate greater intrinsic stress and therefore comparative measurements are only to be made between coatings with equal or very similar thickness.

Numerous methods exist for assessing the adhesion in the coating-substrate composite. The simplest of them is illustrated on Figure 5.3.1. It measures directly the pull-off force of the coating-substrate composite. This method, however, is applicable only for the cases where the strength and adhesion of the adhesive to the coating is greater than the pull-off force, which is rarely the case for wear protective coatings. Another and very widely used adhesion measurement method, illustrated on Figure 5.3.2, is the so-called scratch test where a diamond stylus with spherical shape is slid over the surface of the coated substrate. The normal force with which the stylus is pressed against the coating is gradually increasing during the sliding thus forming a scratch on the surface of the coating. At a certain moment (corresponding to a certain normal force called critical load), a coating

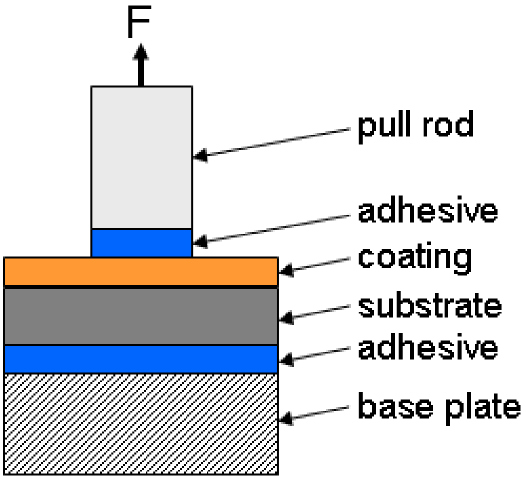

Fig. 5.3.1. Pull-off adhesion strength measurement test

failure event occurs. The most common coating failures are appearance of cracks inside or outside the sliding track, coating spallation and coating perforation down to the substrate inside the sliding track. These events are illustrated on Figure 5.3.3.

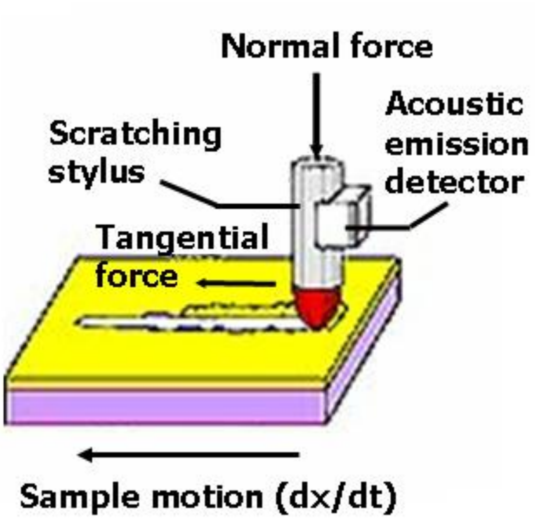

Fig. 5.3.2. The scratch test principle

Some previous work [2] has already considered both intrinsic parameters (scratching speed, loading rate, diamond stylus radius and diamond wear) and extrinsic parameters (substrate hardness, coating thickness, substrate and coating roughness, friction coefficient and friction force) which need to be taken into account in order to improve the interpretation of critical load results. Although the method does not directly measure the pull-off force, adhesive spallation (if any) of the coating is a typical event where the coating-substrate composite suffers adhesive failure. The critical load of adhesive spallation is a quantitative measure of the adhesion strength of the coating and can be used as such in comparative studies of coatings with equal thickness and similar hardness.

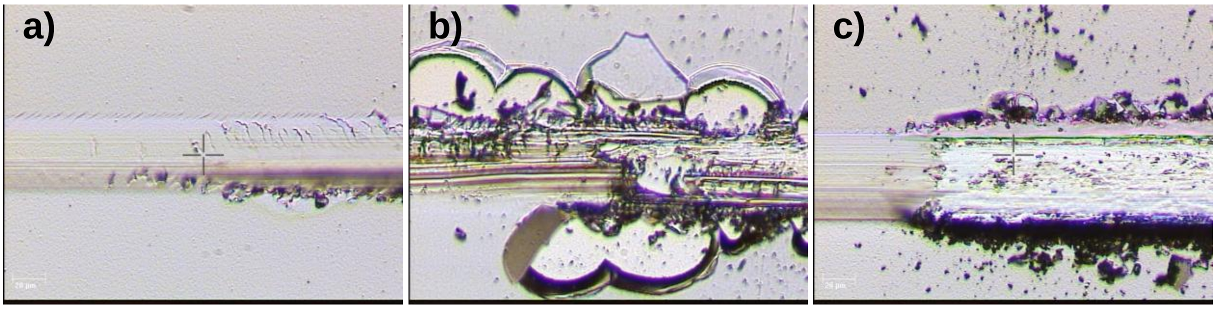

Fig. 5.3.3. Examples for coating failure event. Optical microscope images of: a) circular cracks in the scratch; b) adhesive spallation; c) coating perforation

To measure the adhesion properties of coatings with thickness of less than 1 µm, a variant of the scratch test is used called micro-scratch test (MST). The method was developed in the early 1990s [3], [4] and successfully used for measuring the adhesion properties of very thin (95 nm) TiN coatings [5]. It uses smaller normal forces and diamond styluses with smaller radii than the “macro” scratch test. A comparison between the range of test parameters used by MST and “macro” scratch-test instruments is shown on Table 5.3.1.

Test parameter	MST	Macro
Normal force range	30 mN to 30 N	0.5 to 200 N
Force resolution	0.3 mN	3 mN
Maximum friction force	30 N	200 N
Friction force resolution	0.3 mN	3 mN
Maximum scratch length	120 mm	70 mm
Scratch speed	0.4 to 600 mm/min	0.4 to 600 mm/min
Maximum depth	1 mm	1 mm
Depth resolution	0.3 nm	1.5 nm
XY stage movement	120x20 mm	70x20 mm
XY resolution	0.25 µm	0.25 µm

Table 5.3.1. Comparison between a MST and a "macro" scratch test main features

The modern MST instruments are fully computer-controlled and allow for parameters such as penetration depth, friction force, friction coefficient and acoustic emission to be effectively monitored during the test and easily recorded once the test is accomplished. For visual assessment of the failure events the instruments are supplied with a CCD camera mounted on an optical microscope with appropriate magnification.

Summary of Section 5.3.

MST was used in this work in order to compare the adhesion of the self-lubricating hard coatings with that of the benchmark coating and also to study the effect of solid lubricant addition on the adhesion of the coatings. The direct access to MST equipment and the relatively small thickness of the coatings being 1.5 µm were the factors to determine the choice of MST over the "macro" test. A CSM Instruments microscratch tester was used equipped with a Rockwell C type of indenter (200 µm radius spherical diamond tip). The initial normal force was 0.1 N and the final normal force was 30 N. The normal force was increased with a rate of 100 N/min and the scratching speed was 10 mm/min. This resulted in total scratch length of 3 mm. Visual observation using a microscope attached to the instrument was used to determine the coating failure events.

Reference List to Section 5.3.

1. Schönjahn, C, Lewis, D., Münz, W.-D., and Petrov, I. *Surface Engineering* 16 2 **2000** 176-180

2. Steinmann, P., Tardy, Y., and Hintermann, H. E. *Thin Solid Films* 154 **1987** 333-349

3. Julia-Schmutz, C. and Hintermann, H. E. *Surface and Coatings Technology* 48 **1991** 1-6

4. Sarin, V. K. *Journal of Adhesion Science and Technology* 7 **1993** 1265-1278

5. Benayoun, S., Hantzpergue, J. J., and Bouteville, A. *Thin Solid Films* 389 **2001** 187-193

Section 6. Definition of the materials for the substrates and their surface finish

As already mentioned in Section 4, Si(100) wafers were used as substrates for TEM characterization of the coatings because they are easy to process both mechanically and by means of ion-milling. For tribological and mechanical characterization, however, the self-lubricating hard coatings are to be deposited on substrates satisfying the following criteria:

- To be easily available
- To be chemically inert and possible to store for long periods in laboratory air without corrosion
- To be possible to machine with the in-house equipment available
- To be of such size as to fit in the deposition system substrate holder and the tribological and mechanical characterization equipment
- To be used widely in engineering applications
- To be mechanically stable and tough
- To have hardness comparable to that of the coatings used in order to avoid substrate interference during NHT measurements
- To be able to withstand temperatures of 400 °C which is the maximum temperature the deposition system is capable of achieving

Cermets (also known as hardmetals) of the type WC-Co are widely used in tribological applications such as cutting and forming tools, bearing components and others. Their properties meet all the above mentioned requirements. Therefore, WC-6%Co hardmetal grade HT-600 was chosen as a substrate material for the coatings intended for tribological and mechanical studies. This material consists of WC crystals with average size of 300 nm embedded in a Co matrix. HT-600 disks with 20 mm diameter and 5 mm height were available in-house and were found to be appropriate in terms of geometrical properties.

In order to minimize the influence of the surface roughness on the tribological and mechanical characterization of the coatings, the substrates were polished with diamond compound with grit size of 1 µm to surface roughness R_a<0.02 µm as measured by a Rank-Taylor surface profilometer equipped with a ruby stylus.

Section 7. Deposition of the benchmark coatings as defined in Section 6

As stated in the introduction, comparison of the tribological properties and hardness of the self lubricating hard coatings with these of a pure hard coating (TiN) and a typical MoS_2-based solid lubricant will serve as a basis for judgment of whether the concept of this work has been achieved. For this purpose, TiN and MoSy-based solid lubricant coating have been deposited and their tribological properties and hardness were studied.

7.1. Deposition and tribological properties of the benchmark hard coating

TiN coating was deposited in the deposition system described in Section 3 by RF sputtering of a TIN target. Such a sputtering arrangement (also known as non-reactive sputtering) does not require precise control of the N_2 flow typically needed for deposition of TiN coating by sputtering of Ti targets in $Ar+N_2$ reactive atmosphere. Furthermore, using non-reactive deposition TiN coatings with higher hardness are deposited at low substrate bias voltages compared to reactive deposition [1]. Based on previous laboratory experience, 3 TiN benchmark coatings were deposited at 0.4 Pa, 0 V substrate bias (grounded substrate) and temperatures of 150, 280 and 380 °C. The thickness of the coatings was 1.5 µm and a 170 nm thick Ti layer was deposited under them in order to improve the adhesion. The substrates and their surface quality are described in Section 6. In all cases the chamber was evacuated to pressure of $<10^{-3}$ Pa prior to deposition. The deposition temperature was maintained and measured as described in Section 3. The substrates were sputter-cleaned for 15 minutes by applying -750 V bias to the substrate table at Ar pressure of 2.4 Pa. The tribological and mechanical properties of the resulting coatings were measured with the techniques and at the test conditions described in Section 5. The results of these measurements are summarized in Table 7.1.

Deposition temperature, °C	Hardness $HV_{0.5}$, GPa	Average stable friction coefficient	Wear coefficient, $x10^{10}$ mm^3/Nm
150	18.3	0.83	5.9
280	32.0	0.76	1.73
380	35.0	0.80	1.24

Table 7.1. Properties of the TiN benchmark coatings deposited at different temperatures

The coating deposited at 150 °C has hardness and wear resistance substantially lower to that of the coatings deposited at 280 and 380 °C. The deposition carried out at 380 °C was found to lead to excessive heating of the target. This effect can be minimized when depositing multilayer coatings.

7.2. Deposition and tribological properties of the benchmark solid lubricant coating

Doping of MoS_2 coatings with Ti has been widely used to improve their tribological properties [2], [3]. Significant amount of experience has been gained at the Swiss Center for Electronics and Microtechnology in the field of MoS_2-Ti solid lubricant coatings. Based on this experience, MoS_2-Ti coating was chosen as a solid lubricant benchmark. It was deposited at exactly the same conditions and architecture as the TiN benchmark coating deposited at 280 °C. The solid lubricant benchmark has hardness $HV_{0.5}$ of 16.8 GPa, stable friction coefficient of 0.06 and wear coefficient of $3.7.10^{-11}$ mm^3/m.

Reference List to Section 7

1. Mayrhofer, P., Kunc, F., Musil, J., and Mitterer, C. *Thin Solid Films* 415 **2002** 151-159
2. Sun, Kyu Kim, Young, Hwan Ahn, and Kwang Ho Kim *Surface and Coatings Technology* 169-170 **2003** 428-432
3. Renevier, N., Hampfire, J, Fox, V., Witts, T, Allen, T, and Teer, D. *Surface and Coatings Technology* 142-144 **2001** 67-77

Section 8. Deposition, structural and tribological characterization of TiN/MoS_x multilayer coatings

8.1. Introduction

PVD coatings consisting of alternating layers of different materials have been extensively studied in the past 2 decades. In the early works it was shown that TiN/TiCN multilayer coatings have superior cutting life compared to the individual TiN and TiC coatings [1]. Later it was demonstrated that multilayer coatings with thickness of the individual layers in the range of 2-10 nm have exceptionally high hardness in the order of 50 GPa [2]. The strengthening mechanisms in such structures have been studied extensively and explanations for it such as dislocations blocking by the layer interfaces [3], [4] and Hall-Petch strengthening [5]. Various combinations of metal/metal, metal/ceramic and ceramic/ceramic multilayers were studied and significant improvement of the mechanical and tribological properties of the obtained multilayer coatings compared to the coatings from the pure constituents has been reported. On this basis, it is somewhat surprising that there is very little published effort in studying hard phase/MoS_2 multilayer coatings. Coatings with metal/MoS_2 multilayered structure have been reported by some authors [6], [7], [8], [9], [10], [11], [12] . However, the authors introduced metal layers in the MoS_2 coatings not to combine the tribological properties of MoS_2 with these of the metal but rather to control the structure and growth of MoS_2. Sun et al. used a mixture of Au and rare-earth metal fluoride for this purpose [13]. Watanabe et al. used multilayering of MoS_2 with WS_2 which is also a solid lubricant very similar in structure and properties to MoS_2 [14]. The authors deposited MoS_2/WS_2 coatings with improved tribological properties compared to pure MoS_2 and WS_2 coatings deposited at the same conditions.

To the author's knowledge, so far no work has been published dedicated to the deposition of multilayer coatings consisting of MoS_2 and a hard phase in order to combine the solid lubricant properties of MoS_2 and the high wear resistance and hardness of the hard phase.

When combining two phases in a multilayer coating, the structure of each phase strongly influences the structure of the coating as a whole and hence its properties. Furthermore, the growth of each phase can be strongly influenced by the structure of the other. Since the thickness of the individual layers is in the order of few nanometers, the initial stages of structure formation of each phase play a key role in the overall coating structure. Therefore, prior to deposition of a functional TiN/MoS_2 multilayer coating, the initial stages of growth of

MoS_2 on magnetron-sputtered TiN layers are to be studied in detail. This will allow to control the structure of the MoS_2 layers by selecting the deposition parameters resulting in the desired MoS_2 structure.

The structure of magnetron sputtered MoS_2 coatings has been studied widely in the past 3 decades. It was reported that it strongly influences the tribological properties of the coatings [15], [16], [17], [18], [19], [20]. Generally 3 structural types of MoS_2 coatings were reported by the researchers:

- Type I 2H MoS_2 coatings with their c-axis oriented parallel to the substrate
- Type II 2H MoS_2 coatings with their c-axis oriented perpendicular to the substrate
- Amorphous MoS_2 coatings

Type II coatings have lower friction coefficient and higher wear life compared to type I coatings as reported by the authors. Spalvins [16] stated that amorphous coatings had no lubricating properties. Friction-induced reorientation of the type I crystallites into type II was reported to be responsible for the lubricious properties of type I MoS_2 coatings [21], [22], [23], [19], [24], [25], [26], [27], [28], [29]. Another advantage of type II over type I MoS_2 coatings is the better oxidation resistance of the former [17]. For these reasons type II is the preferred structure of MoS_2 coatings.

It was also noted that sputter-deposited MoS_2 coatings are substoichiometric with a general chemical composition MoS_x where $x<2$ [30], [31], [32]. Some controversy exists on the relation between the stoichiometry of the MoS_x coatings and their tribological properties. Christy et al. reported that coatings with composition close to the stoichiometric have better properties than sub-stoichiometric MoS_x [33]. Dimigen et al. [34] reported that sulfur-deficient films exhibit lower friction coefficient and wear rate than stoichiometric coatings with optimum tribological performance at $x=1.5$. Coatings with $x<1$ had no lubricious properties. This observation was confirmed by the same group in another publication [32] while Bolster et al. found no relation between stoichiometry and tribological properties of MoS_x [35]. Aubert et al. observed minimum friction coefficient for coatings with $x=1.5\div1.6$ [18]. Similar observation was made by Moser et. al [36] who reported minimum friction coefficient for coatings with $x=1.5$ The authors observed no lubricious properties for coatings with $x=0.8$. The coatings with $x=2.5$ had low friction coefficient but short wear life.

Based on these considerations, from now on in this work the term “MoS_2” will be referred to as “MoS_x” when used in the context of MoS_2-based coatings.

The most important deposition parameters that influence the orientation (type I or type II) of magnetron-sputtered MoS_2 coatings are as follows:

- Temperature. The influence of temperature on the structure and chemical composition of MoS_x coatings has been studied by many authors. Amorphous MoS_x coatings deposited at room temperature or below are reported by Spalvins [16], [37], [25], Dimigen et al. [34], Kuwano and Nagai [38], Moser and Levy [39]. MoS_x films deposited at room temperature with nanocrystalline structure were reported by Nozhenkov et al. [21], [26], Lince and Fleischauer [22] and Bertrand [40], [29], [41]. Coatings deposited at elevated temperatures were reported to be crystalline [34], [16], [21], [22], [40], [42], [37], [43], [44], [25], [26], [29]. Change from type II to type I coatings with increasing substrate temperature has been reported by some authors [45], [46], [47]. The deposition temperature influences not only the structure of the MoS_x coatings but also their stoichiometry. Reichelt and Mair studied reactive deposition of MoSx by sputtering of a Mo target in Ar+H_2S reactive atmosphere [31]. The authors noticed decrease of x with increasing temperature and explained it with the desorbtion of S atoms at elevated temperature. The same observation was made by Dimigen et al. for MoS_x coatings deposited by sputtering of MoS_2 target [34]. Bichsel et al., however, reported little influence of temperature on stoichiometry of MoS_x coatings deposited in the range of -70÷150 °C. The slightly higher value of x observed for coatings deposited at higher temperature was ascribed to increased reactivity of Mo sites on the surface of the growing coating at higher temperatures [48]. Similar to this was the observation reported by Moser et al. [36] who found little influence of deposition temperature on the stoichiometry of MoS_x coatings deposited in the temperature range 100÷500 °C.
- Chamber pressure. This deposition parameter has also a very pronounced effect on the structure and chemical composition of sputter-deposited MoS_x coatings. Its influence on the has been studied by many authors. Buck reported a well pronounced type I structure at deposition pressure of 1.73 Pa [49]. Moser et al. [36] obtained amorphous MoS_x at 0.3 Pa, type II MoS_x at 1 Pa and type II MoS_x at 6 Pa at room temperature. The same authors deposited type II MoS_x coatings at 0.3 Pa and type I MoS_x coatings

at 0.4 Pa, both at substrate temperature of 300 °C [29]. Change of orientation from type I to type II with increasing deposition pressure has also been reported by other authors [46], [47], [50]. The influence of pressure on the chemical composition has been also studied and the general conclusion made by the researchers was that the parameter x increases with increasing pressure [34], [48], [46], [51], [50]. However, Ito and Nakajima found the opposite dependence [30] while Weise et al. found no influence of the deposition pressure on stoichiometry of the MoS_x coatings [20].

- Substrate bias. Ion bombardment of the growing MoS_x coatings has a very strong effect on its stoichiometry. Applying negative bias voltage to the substrate intensifies the ion bombardment of the growing coating. In the case of MoS_x, ion bombardment leads to preferential sputtering of the S atoms adsorbed at the surface of the coating or even already chemically bonded to a Mo atom. This effect has been reported for MoS_x coatings [34], [32], [36], [48], [52], [53], [46], [47] and for bulk MoS_2 as well [54], [55], [56]. Substrate bias strongly influences the structure and orientation of sputter-deposited MoS_x films. Tendencies towards formation of type II structure at moderate substrate bias and type I structure at no or low substrate bias are reported [36], [49] while no influence of the bias on structure has been found by some authors [46], [47]. Amorphisation of MoS_x coatings treated by post-deposition Ar^+ bombardment has been reported [57]. Densification of the structure of MoS_x coatings by Ar^+ ion bombardment either during [42], [58] or after [59] deposition has also been observed.

In summary, some controversy on the effects of the main deposition parameters on the structure and chemical composition of MoS_x coatings still exists. Most studies report findings based on the whole volume of the coatings and very little has been published on the nucleation and initial stages (fist few nm of film thickness) of growth of MoS_x coatings. Spalvins has reported ridge formation (type I structure) in the fist stages of growth [25], [23]. He used plain-view TEM so unfortunately no information on the MoS_x-substrate interface is available from his studies. Moser et al. published very valuable findings on the sputter-deposited MoSx growth on Si(100) substrates presenting lattice-resolution TEM images of the cross-section of the MoSx-substrate interface [36], [60]. However the authors did not systematically study the influence of the main deposition parameters on the structure of the interfacial region. A similar study carried out by Lee and More reported on CVD deposition of MoS_x. The authors found out a change from type II to type I structure with temperature increasing from 320 °C to 430 °C. Shimada studied the influence of substrate chemistry on the orientation of MoS_x nanoclusters deposited by molecular beam epitaxy on Al_2O_3 and TiO_2 particles [61]. No study could be found describing the nucleation and first stages of growth of MoS_x coatings deposited on TiN substrate although TiN has been used as a substrate for MoS_x coatings [62]. The significant scattering of the reported result strongly suggests that the influence of the deposition parameters on the structure and stoichiometry of MoS_x coatings is very complex and depends on "random" factors such as deposition system geometry and the nature of the sputtering target.

8.2. Experimental details

On the basis of the published effort mentioned above no prediction can be made about the structure of MoS_x deposited on TiN layers at different conditions in the deposition system used in this work. For this reason, an experiment was carried out to study the influence of substrate temperature, deposition pressure and substrate bias on the structure of MoS_x coatings with thickness of <50 nm deposited on TiN. The deposition parameters matrix is shown on Table 8.1. A thin TiN layer was deposited under each MoS_x coating so a multilayer coating as described on Figure 8.1 was obtained. The coatings are marked as follows:

- LTLP (Low Temperature Low Pressure): the multilayer coating deposited at 150 °C and 0.4 Pa
- LTHP (Low Temperature High Pressure): the multilayer coating deposited at 150 °C and 2.4 Pa
- MTLP (Medium Temperature Low Pressure): the multilayer coating deposited at 280 °C and 0.4 Pa
- MTHP (Medium Temperature High Pressure): the multilayer coating deposited at 280 °C and 2.4 Pa
- HTLP (High Temperature Low Pressure): the multilayer coating deposited at 380 °C and 0.4 Pa
- HTHP (High Temperature High Pressure): the multilayer coating deposited at 380 °C and 2.4 Pa.

Substrate temperature T, °C	**Deposition pressure p, Pa**	**Substrate bias, V**	**MoS_x Layer identification**	**Multilayer coating indentification**
150	0.4	-50	LTLP-50	LTLP
150	0.4	-25	LTLP-25	
150	0.4	0	LTLP0	
150	0.4	50	LTLP50	
150	0.4	100	LTLP100	
150	2.4	-50	LTHP-50	LTHP
150	2.4	-25	LTHP-25	
150	2.4	0	LTHP0	
150	2.4	50	LTHP50	
150	2.4	100	LTHP100	
280	0.4	-50	MTLP-50	MTLP
280	0.4	-25	MTLP-25	
280	0.4	0	MTLP0	
280	0.4	50	MTLP50	
280	0.4	100	MTLP100	
280	2.4	-50	MTHP-50	MTHP
280	2.4	-25	MTHP-25	
280	2.4	0	MTHP0	
280	2.4	50	MTHP50	
280	2.4	100	MTHP100	
380	0.4	-50	HTLP-50	HTLP
380	0.4	-25	HTLP-25	
380	0.4	0	HTLP0	
380	0.4	50	HTLP50	
380	0.4	100	HTLP100	
380	2.4	-50	HTHP-50	HTHP
380	2.4	-25	HTHP-25	
380	2.4	0	HTHP0	
380	2.4	50	HTHP50	
380	2.4	100	HTHP100	

Table 8.1. Deposition conditions matrix

The separate MoS_x layers in these coatings are marked with the same abbreviation with the value of the substrate bias voltage added in the end of the abbreviation. For example the abbreviation HTLP-25 means MoS_x layer deposited at 0.4 Pa, 380 °C and -25 V substrate bias. The structure of all coatings was studied by means of TEM imaging, SAED and EDX spectroscopy, all carried out in the same TEM as described in 4. The specimen preparation procedure is also described in the same chapter. Such an architecture is very beneficial for studying the structure of MoS_x deposited on TiN layers because:

- It simulates multilayer TiN/MoS_x coatings. MoS_x is deposited on a freshly deposited TiN layer without breaking the vacuum in the deposition chamber.

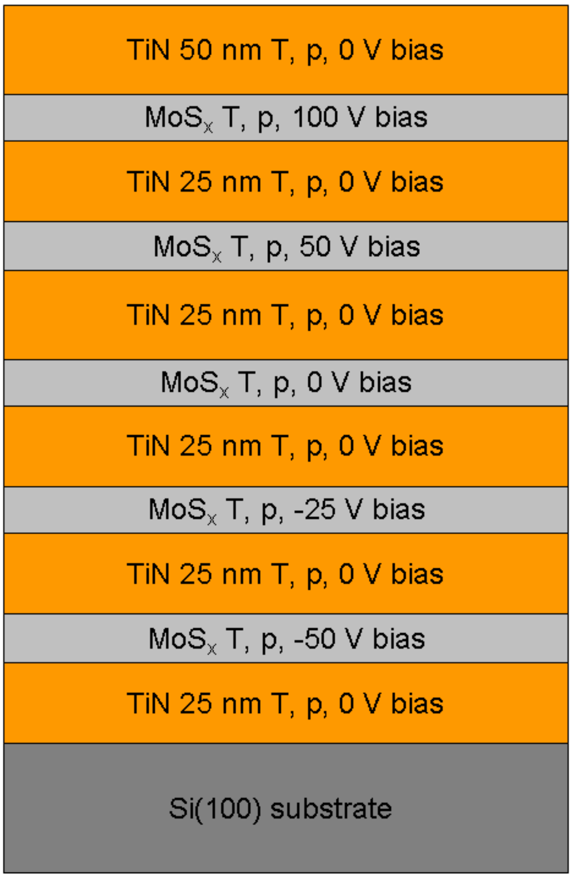

Fig. 8.1. TiN/MoS_x *multilayer architecture used for studying the effect of the deposition conditions on the structure of the near-interface region of* MoS_x

- All MoS_x layers are deposited at the same preconditioning state of the deposition chamber thus avoiding variation of the residual water vapor and oxygen partial pressures which are reported to influence the growth of MoS_x [63].

- A TEM specimen preparation is time and effort consuming a procedure. Using the coating architecture shown on Figure 8.1. reduces the number of TEM specimens needed for studying the growth of MoS_x from 30 to 6. Furthermore, the possible artifacts introduced during sample preparation will be the same for all MoS_x layers in one sample thus reducing the probability of misinterpretation of the TEM images and SAED patterns.

In all cases the chamber was evacuated to pressure of $<10^{-3}$ Pa prior to deposition. The deposition temperature was maintained and measured as described in 3. The substrates were sputter-cleaned for 15 minutes by applying -750 V bias to the substrate table at Ar pressure of 2.4 Pa. Then the layered architecture was deposited by moving the substrate table under a TiN and MoS_2 targets to deposit TiN and MoS_x layers, respectively. During the deposition of one component the source of the other was shut down. The deposition pressure was maintained at the desired value by feeding Ar in the chamber through a needle valve.

8.3. Deposition parameters – MoS_x structure relationship

In this part the influence of the deposition parameters substrate temperature, deposition pressure and substrate bias on the properties of the resulting MoS_x layers will be studied and a brief summary of the deposition parameters - layer structure will be made.

8.3.1. LTLP multilayer coating

The SAED pattern of multilayer coating LTLP is shown on Figure 8.2. It consists of a typical polycrystalline SAED pattern superimposed over the monocrystalline SAED pattern of the Si(100) substrate. The presence of the Si(100) SAED pattern is due to the fact that the diffraction aperture used was bigger than the overall thickness of multilayer coating LTLP. Such a superposition, however, is useful because it gives information about the preferred orientation (if any) of the crystal phases relative to the surface of the substrate. In this case the diffraction spot produced by the (100) plane of the Si(100) substrate is marked with a red square. This crystal lattice plane is actually parallel to the surface of the Si(100) substrate and all diffraction spots that lay on the red line shown on the figure are parallel to the surface of the substrate. The crystalline state of the TiN is fcc, as defined from the diffraction rings. A more detailed information (i.e. preferred orientation relative to the substrate surface, crystal size, etc.) can be defined from the SAED pattern. However, it is not the objective of this work. What is important, however, is to find out what is the state of the MoS_x layers in coating LTLP. A more careful look at the region around the central spot of the SAED pattern reveals a pair of diffraction arcs situated around the red line as shown on the insert where these arcs are marked with orange arrows. These arcs correspond to a lattice spacing of 1.3 nm which is in good agreement with the (001) lattice spacing of 2H MoS_2. Therefore, 2H MoS_x exists in coating LTLP with its c-axis perpendicular to the substrate surface (type II).

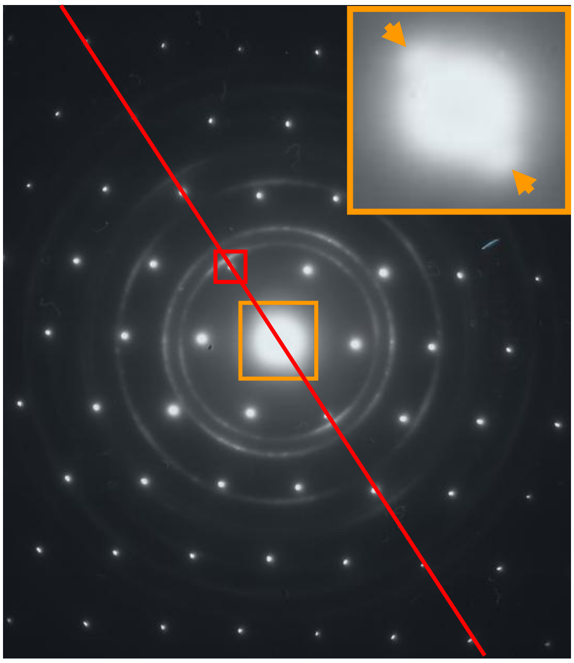

Fig. 8.2. SAED pattern of multilayer coating LTLP. The red line denotes the planes parallel to the surface of the Si(100) substrate. The red square shows the Si(100) diffraction spot. The orange arrows show the 2H MoS_2 (001) diffraction arcs.

8.3.1.1. Layer LTLP-50

A TEM bright field image of the layer is shown on Figure 8.2a. The growth direction is shown with an orange arrow on the figure. The orientation of the TEM images on all figures from now on will be the same unless stated differently. Small crystallites (circled in red) embedded in an amorphous matrix are seen on the figure. Some of these crystals are common for the neighboring TiN and MoS_x layer which strongly supports the conclusion that local epitaxy takes place at this case. Local epitaxy in (Ti,Al)N/Mo multilayer coatings has been reported by Tavares et al. [64]. The presence of metallic Mo in ion-irradiated MoS_2 has been proved by Feng and Chen [56]. Dark field TEM image taken from the TiN (111) diffraction ring and presented in Figure 8.2b reveals the similarity of the structure of the crystals with fcc TiN.

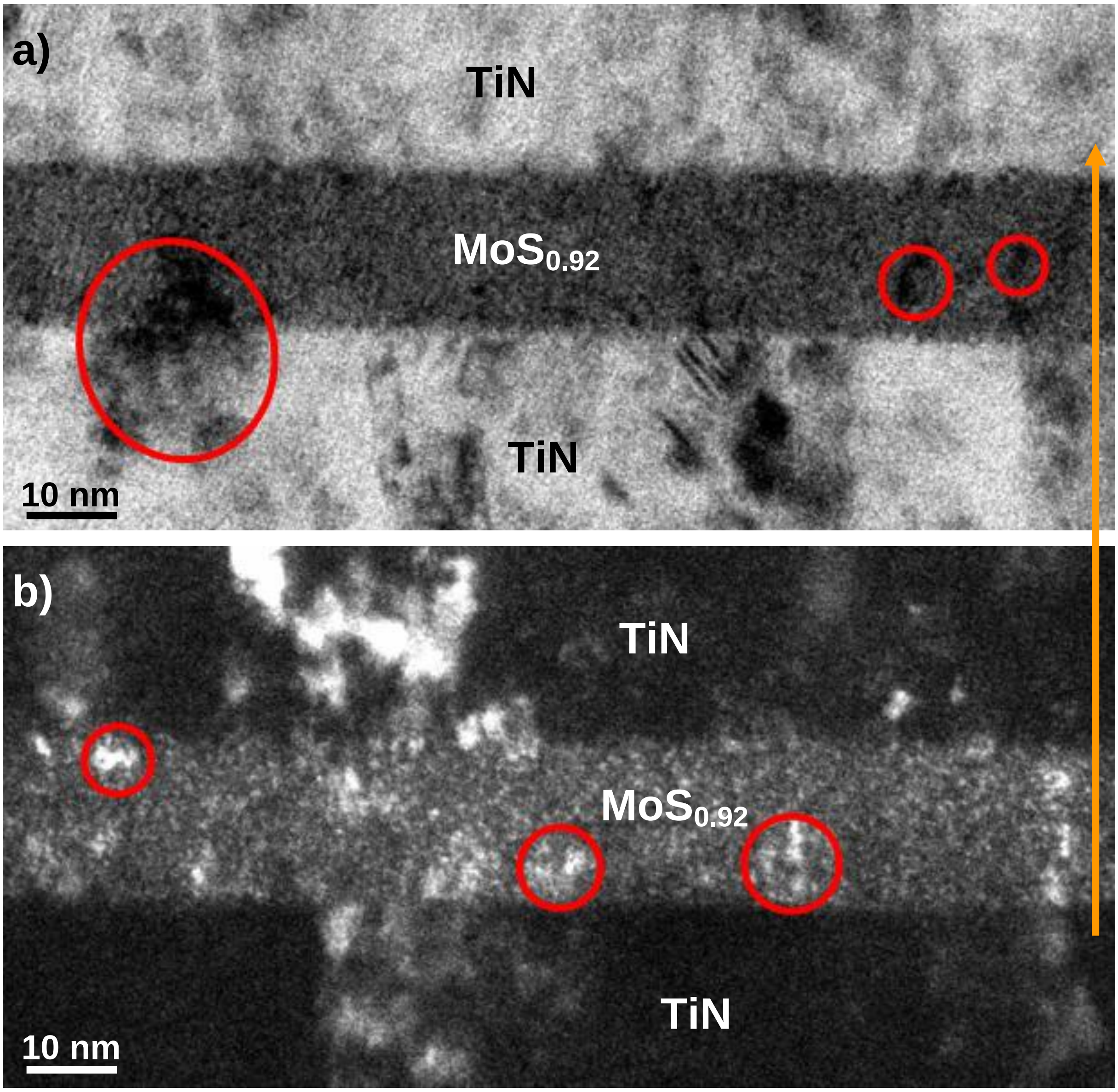

Fig. 8.2. a) TEM bright field image of layer LTLP-50; b) TEM dark field image of the same layer. The red circles show some of the cubic crystals found in the layer and the orange arrow shows the growth direction

Therefore the conclusion can be made that the structure of layer LTLP-50 consists of fcc Mo-based MoS_y crystals embedded in an amorphous MoS_z matrix. The numbers y and z can not be defined with the equipment used but the overall value of x was estimated to be 0.92 so the overall layer chemical composition is $MoS_{0.92}$, as shown on the figure.

8.3.1.2. Layer LTLP-25

This layer has 2H structure as seen from Figure 8.3. The (001) lattice fringes are clearly seem on the image and the crystals are oriented with their c-axis perpendicular to the substrate surface (type II). The crystals are extremely small, being only about 5 nm in lateral dimension and consisting of only 3-5 (001) layers in height. They are embedded in an amorphous matrix. The chemical composition of this layer was estimated to be $MoS_{0.96}$.

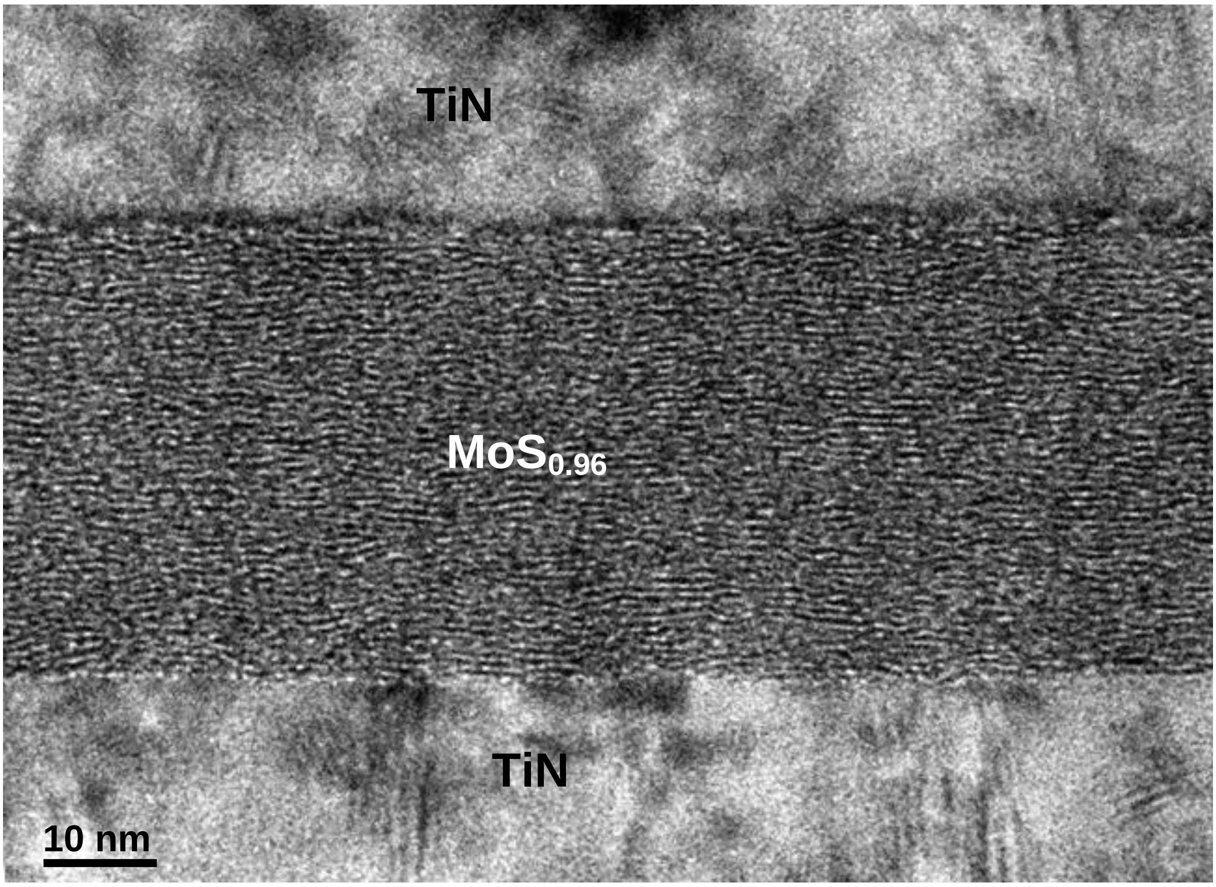

Fig. 8.3. TEM bright field image of layer LTLP-25. The lattice fringes of the 2H MoS_x *(001) planes are clearly seen.*

8.3.1.3. Layer LTLP0

This layer is completely amorphous as seen on Figure 8.4. The chemical composition of this amorphous phase was estimated to be $MoS_{1.22}$. The higher value of x compared to that of the MoS_x layers deposited with negative substrate bias suggests that preferential sputtering of the S atoms occurs during deposition on negatively biased surfaces. This is in good agreement with the observations made by previous researchers.

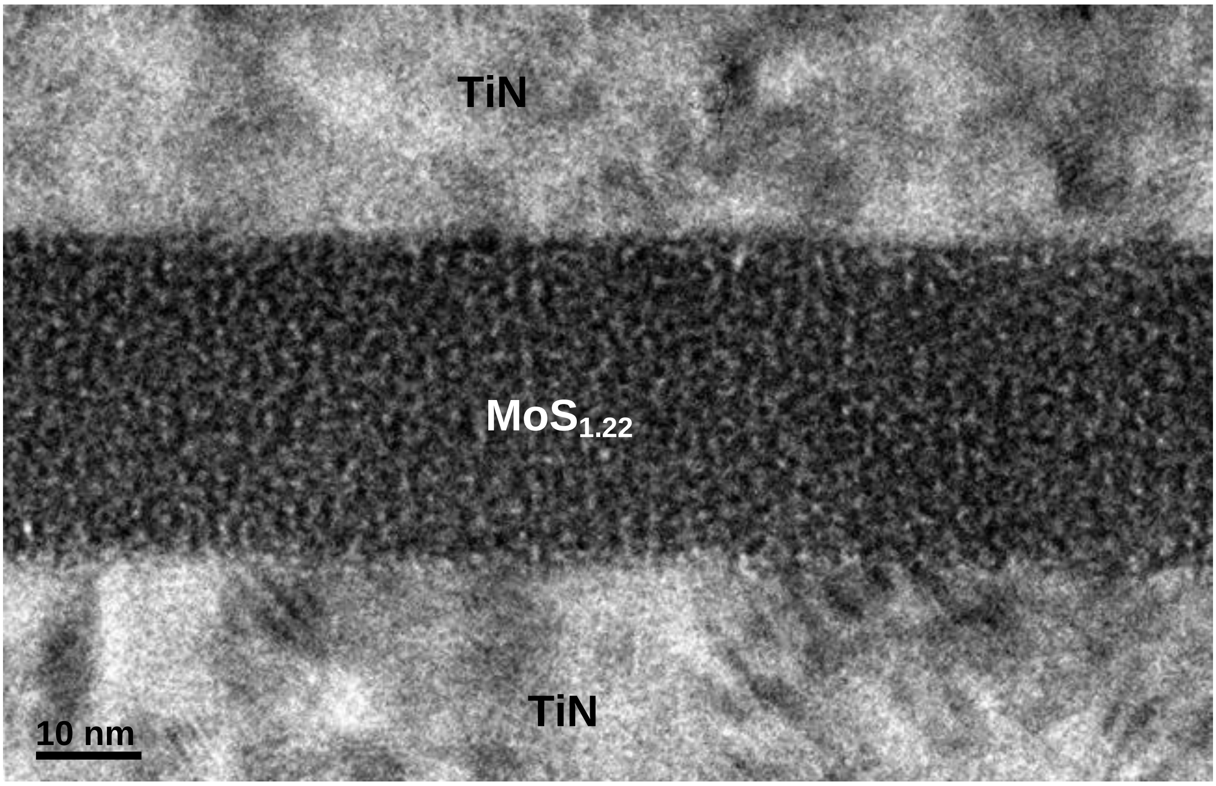

Fig. 8.4. TEM bright field image of layer LTLP0. The layer is completely amorphous.

8.3.1.4. Layer LTLP50

A TEM image of this layer is shown on Figure 8.5. The layer has 2H structure with its crystallites substrantially bigger than these observed in the case of the layer deposited at -25 V substrate bias. The stoichiometry of the layer corresponds to $MoS_{1.50}$. Some type I oriented crystals are observed.

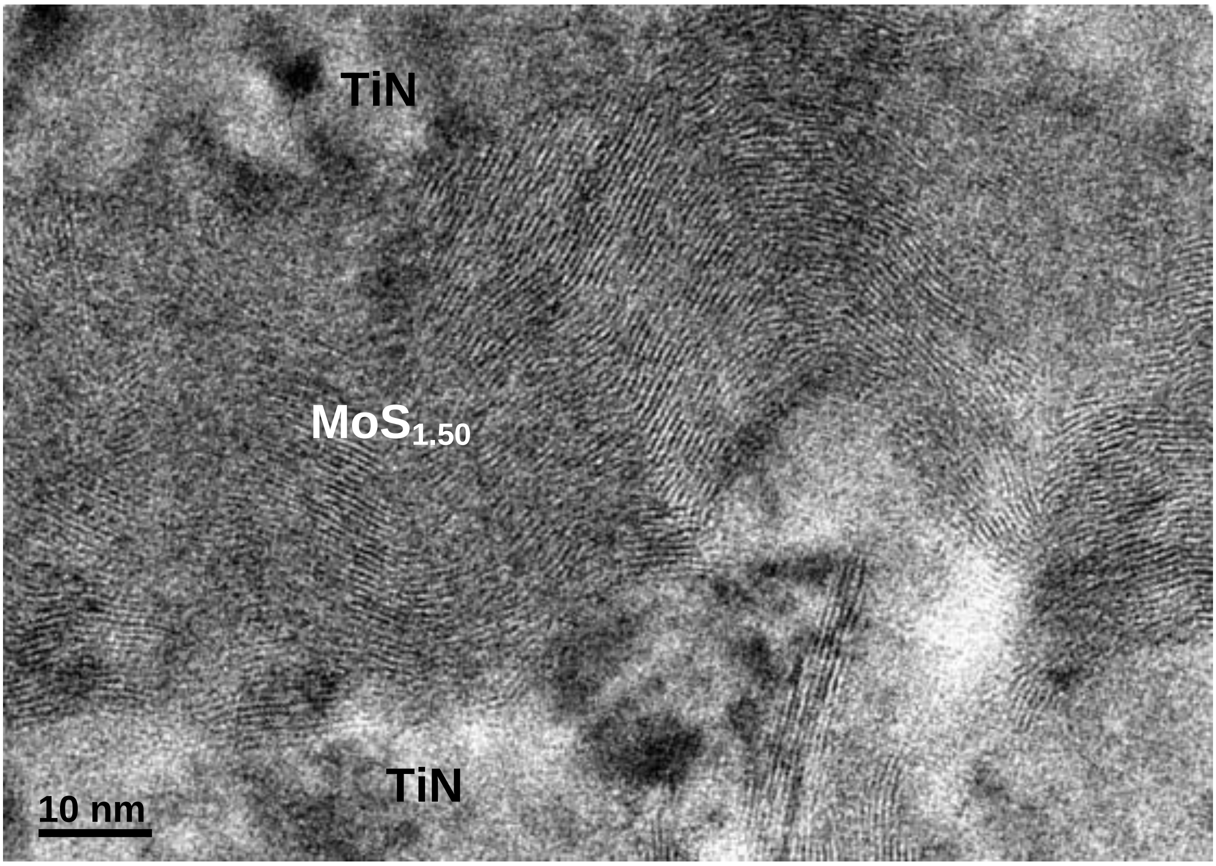

Fig. 8.5. TEM bright field image of layer LTLP50.

8.3.1.5. Layer LTLP100

A TEM inage of this layer is shown on Figure 8.6. No significant difference in both structure and stoichiometry was found compared to layer LTLP50.

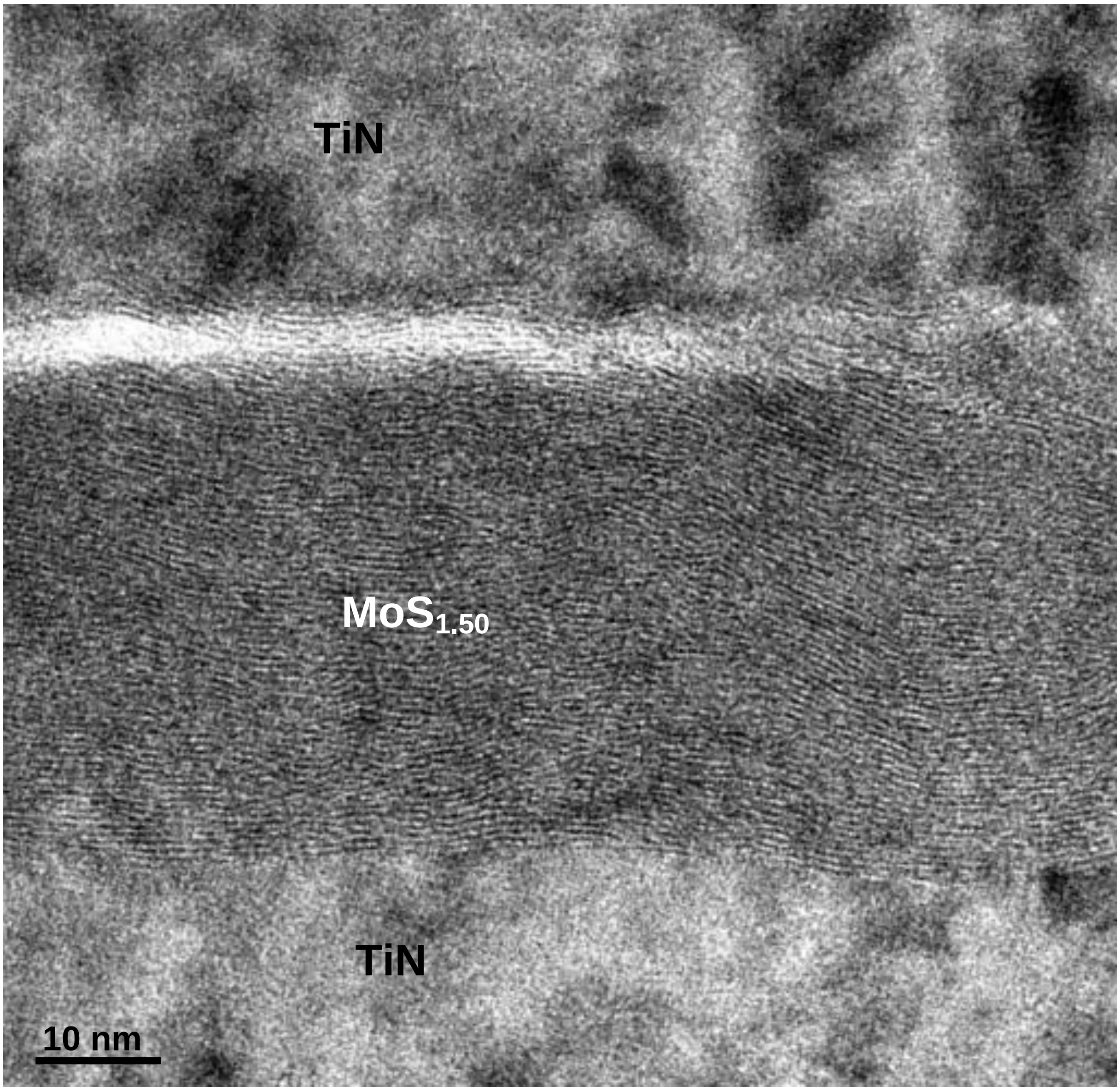

Fig. 8.6. TEM bright field image of layer LTLP100

8.3.2. LTHP multilayer coating

The SAED pattern of LTHP multilayer coating is shown on Figure 8.7. The most significant difference compared to the SAED pattern of the LTHP multilayer coating is the presence of another pair of diffraction arcs corresponding to the 2H MoS_2 (001) crystal planes, as shown on the figure. These two new arcs are rotated at 90° relative to the red line. This means that in the LTHP multilayer both type I and type II 2H MoS_x exist, in contrast to the case of the LTLP multilayer where only type II 2H MoS_x was identified by both SAED and lattice-resolution TEM.

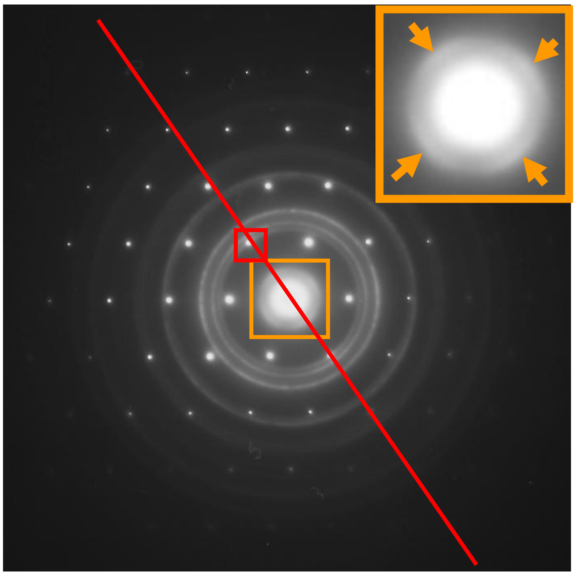

Fig. 8.7. SAED pattern of multilayer coating LTHP. The red line denotes the planes parallel to the surface of the Si(100) substrate. The red square shows the Si(100) diffraction spot. The orange arrows show the 2H MoS_2 (001) diffraction arcs.

8.3.2.1 Layer LTHP-50

The MoSx layer deposited at -50 V has a dual structure, as shown on Figure 8.8. The initial 5 nm or more of the growth result in amorphous structure. Then a sudden initiation of growth of type I oriented 2H crystals takes place. Some small type II crystallites are also seen at some places of the layer. The overall chemical composition of the layer corresponds to $MoS_{1.44}$

8.3.2.2. Layer LTHP-25

This layer also consists of 2 types of structures as shown on Figure 8.9. In the initial few nm of layer growth, a mixed 2H + amorphous structure is formed which later switches to 2H type I. The chemical composition of the layer was estimated to be $MoS_{1.70}$.

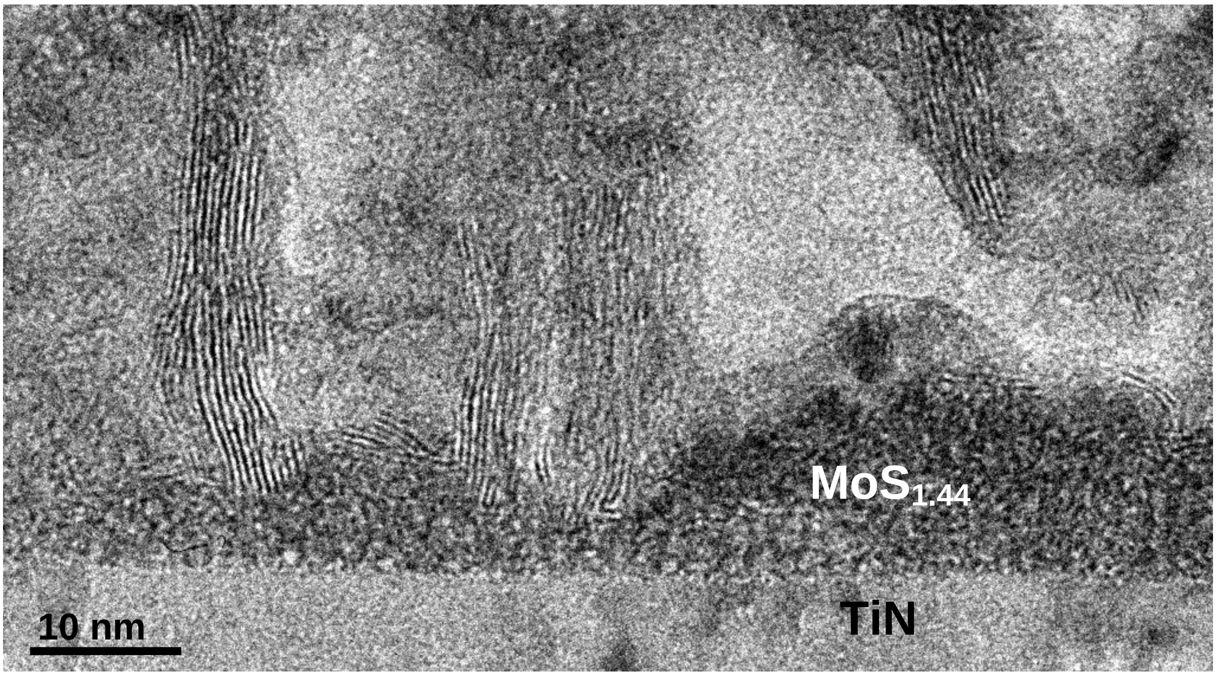

Fig. 8.8. TEM bright field image of layer LTHP-50. Note the type II MoSx crystals in the left part of the image.

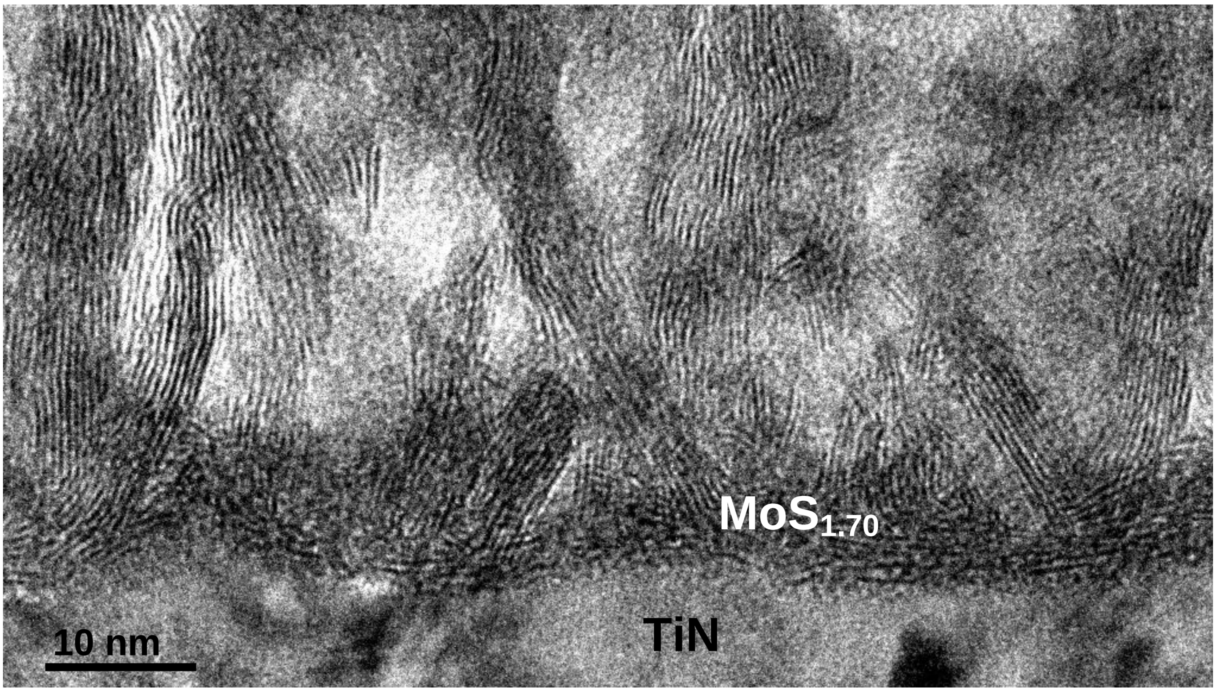

Fig. 8.9. TEM bright field image of layer LTHP-25.

8.3.2.3. Layer LTHP0

At 0 V substrate bias the MoS_x layer deposited at LTHP conditions is almost fully crystalline with 2H structure as seen from Figure 8.10. The first few nm of the film are type II followed by transition into type I crystals. The chemical composition of the layer is $MoS_{2.03}$.

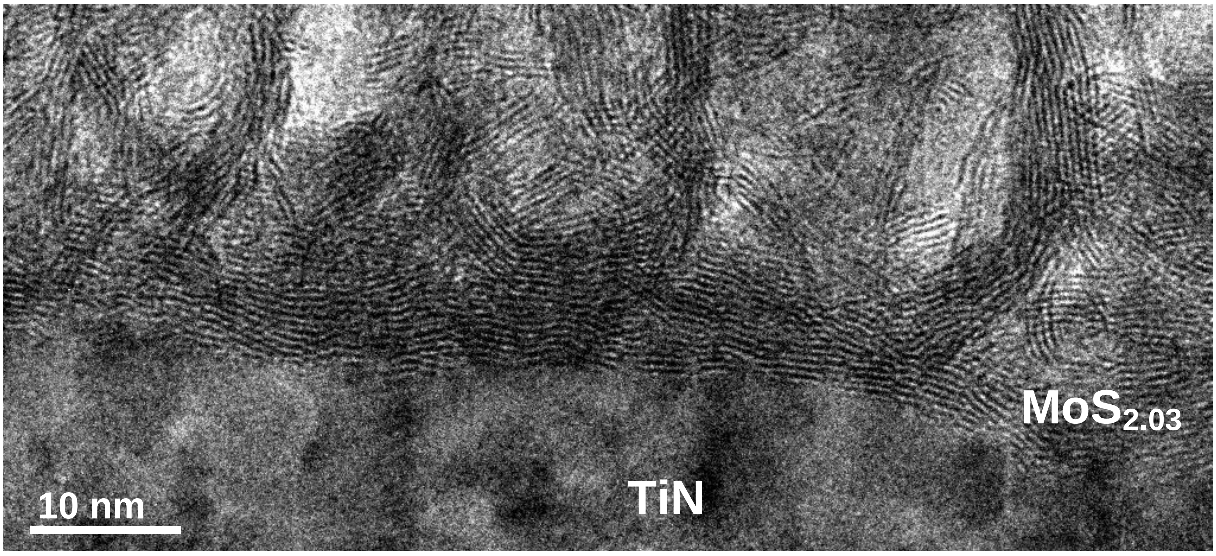

Fig. 8.10. TEM bright field image of layer LTHP0.

8.3.2.4. Layer LTHP50 and layer LTHP100

These layers have the same structure as the layers deposited at 0 V substrate bias, as evident from Figure 8.11 and 8.12. The only difference between the three types of layers is their stoichiometry which is $MoS_{2.13}$ and $MoS_{2.23}$ for the layers deposited at 50 V and 100 V substrate bias, respectively.

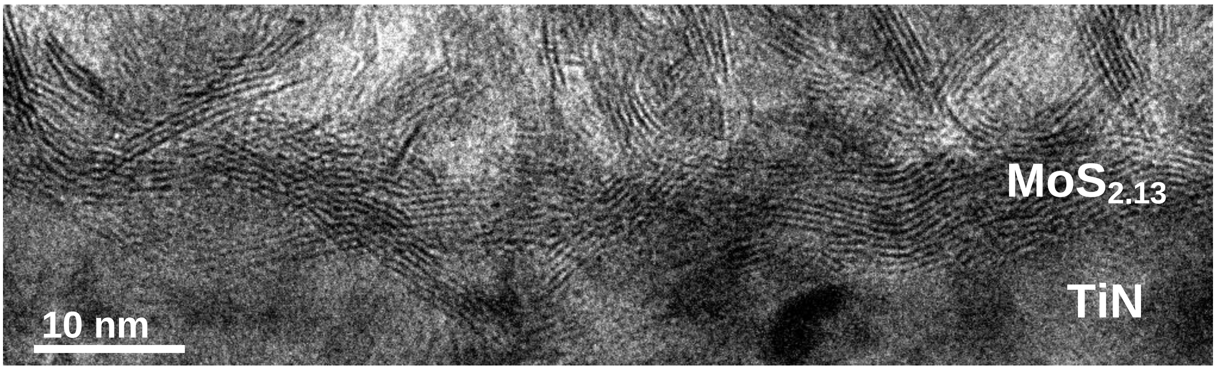

Fig. 8.11. TEM bright field image of layer LTHP50.

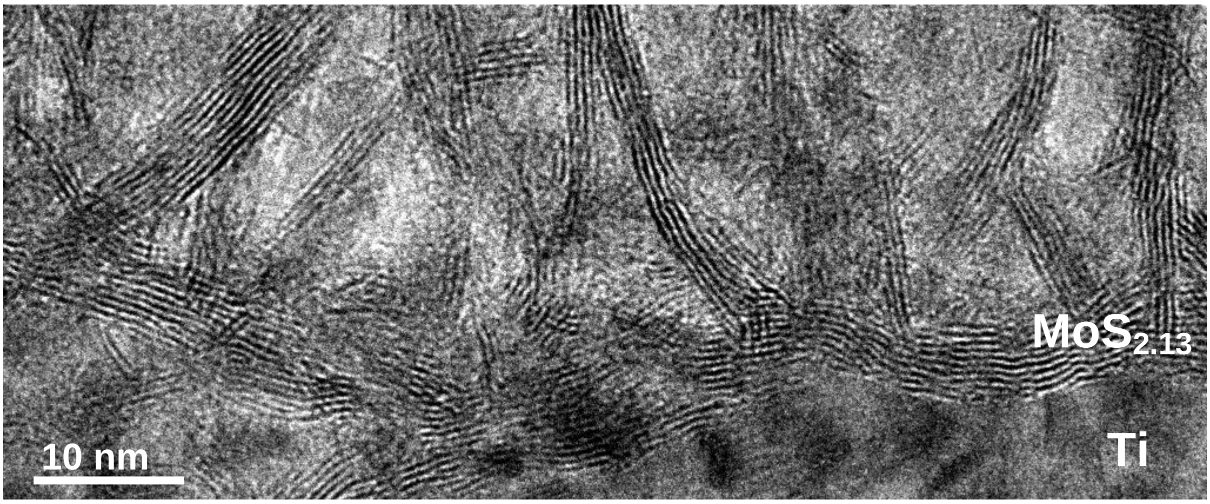

Fig. 8.12. TEM bright field image of layer LTHP100.

8.3.3. MTLP multilayer coating

The SAED pattern of this multilayer coating is presented on Figure 8.13. It is very similar to that of the LTLP multilayer coating. The only 2H MoS_x crystals identified on this SAED pattern are of type II. The other crystalline phase identified is fcc TiN.

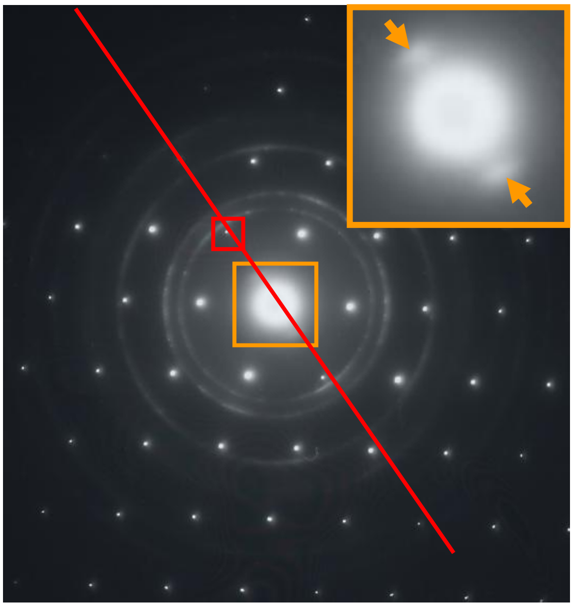

Fig. 8.13. SAED pattern of multilayer coating MTLP. The red line denotes the planes parallel to the surface of the Si(100) substrate. The red square shows the Si(100) diffraction spot. The orange arrows show the 2H MoS_2 (001) diffraction arcs.

8.3.3.1. Layer MTLP-50

This layer consists of cubic crystallites embedded in amorphous matrix (encircled in red), as seen from Figure 8.14. The amount of the amorphous matrix is less compared to layer LTLP-50. The overall chemical composition of the layer corresponds to $MoS_{1.00}$.

8.3.3.2. Layer MTLP-25

This layer is very similar to layer MTLP-50. A TEM image of layer MTLP-25 is shown on Figure 8.15. In this case, the amount of the amorphous phase is more significant and the size of the cubic crystals (encircled in red) is smaller than that in layer MTLP-50. The overall chemical composition of this layer corresponds to $MoS_{1.05}$.

8.3.3.3. Layer MTLP0

As seen from Figure 8.16, this layer consists of 2H crystals with type II orientation embedded in a small amount of amorphous phase. The overall composition of the layer is $MoS_{1.63}$.

8.3.3.4. Layer MTLP50

This layer also consists of type II 2H crystals as seen from Figure 8.17. It is difficult to estimate by imaging whether amorphous phase presents in this layer. The overall chemical composition of the layer corresponds to $MoS_{1.50}$.

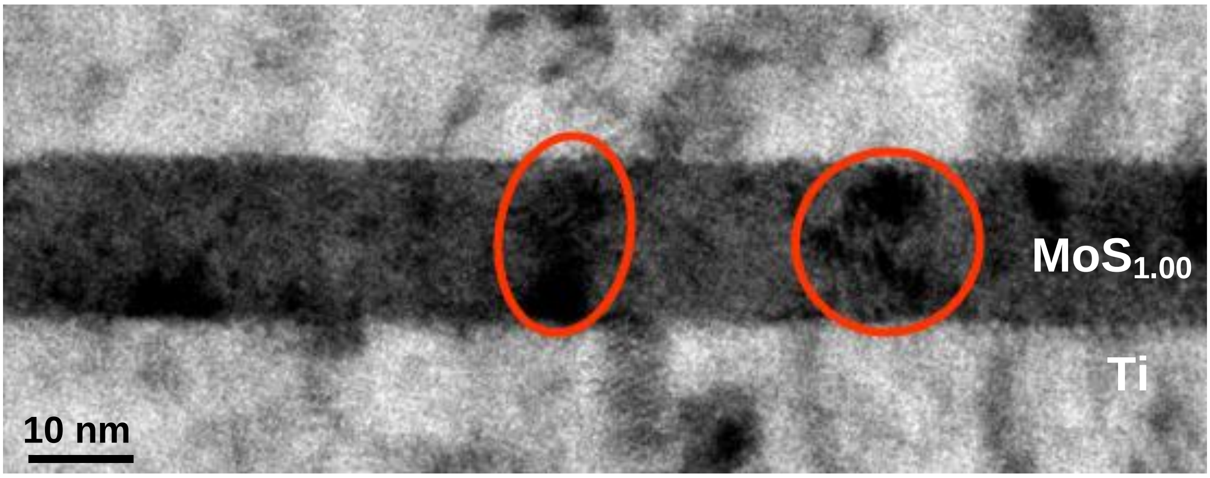

Fig. 8.14. TEM bright field image of layer MTLP-50. The red circles show some of the cubic crystals.

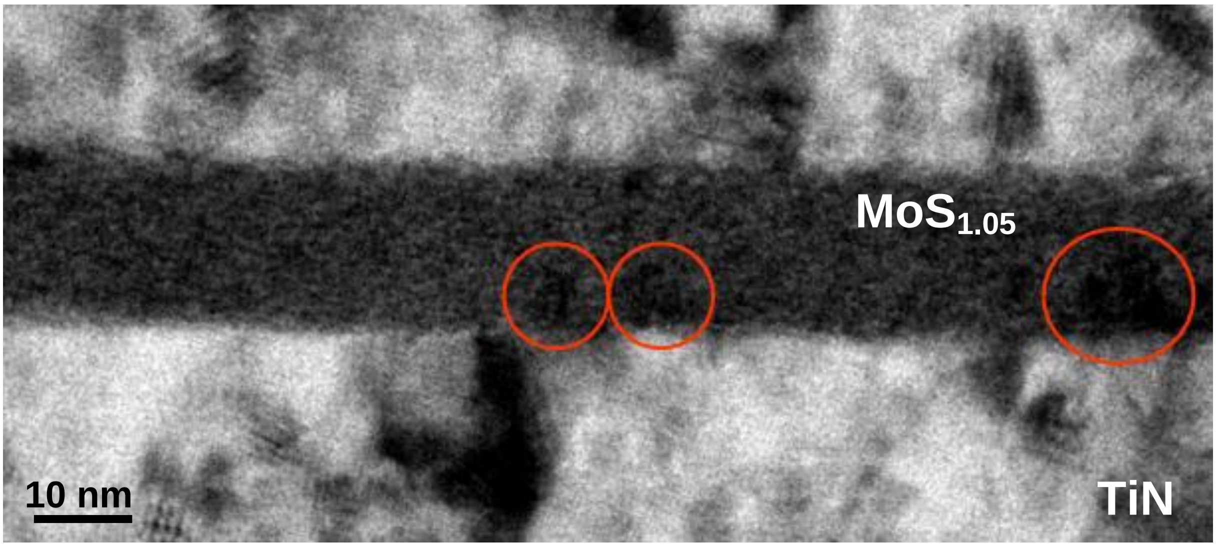

Fig. 8.15. TEM bright field image of layer MTLP-25. The red circles show some of the cubic crystals.

8.3.3.5. Layer MTLP100

The structure of this layer is very similar to that of layer MTLP50, as seen from Figure 8.18. The structure consists of type II 2H crystals and the chemical composition of the layer corresponds to $MoS_{1.53}$.

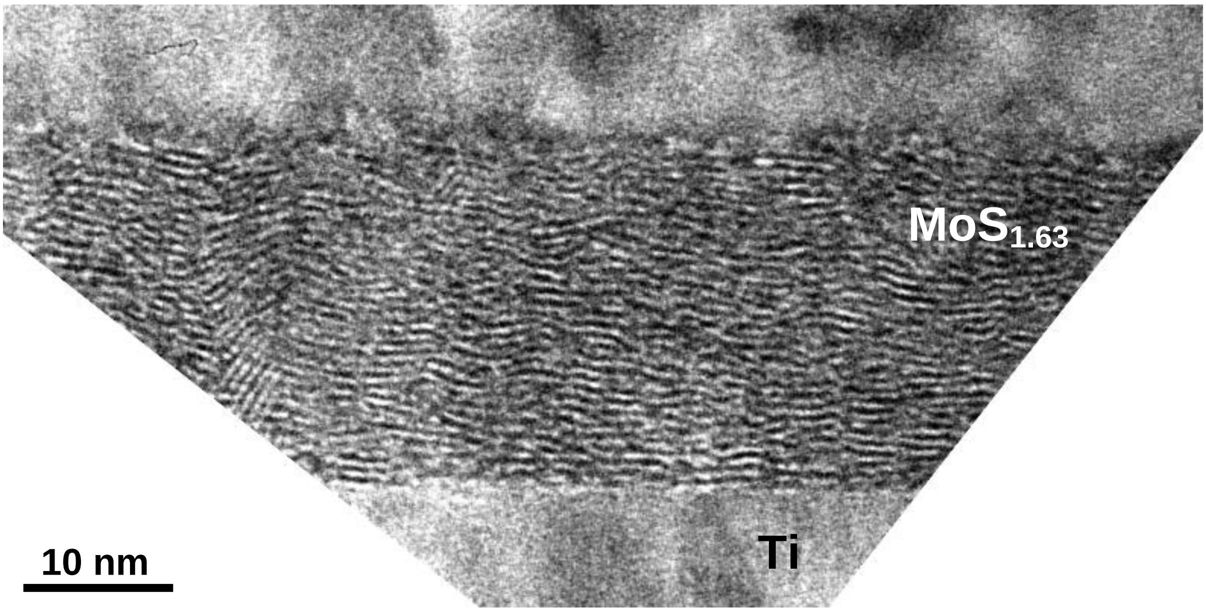

Fig. 8.16. TEM bright field image of layer MTLP0. The lattice fringes of the 2H MoS_x (001) planes are clearly seen.

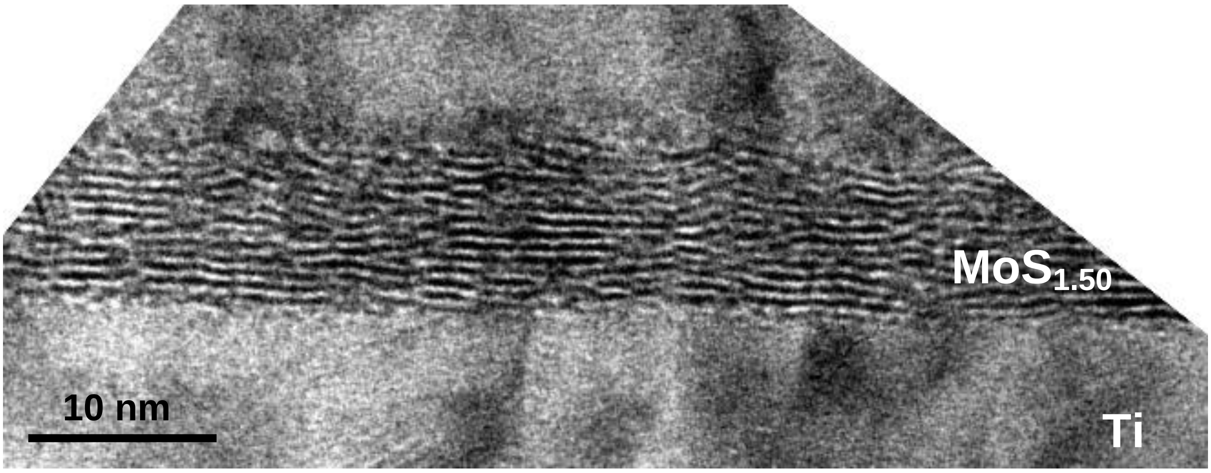

Fig. 8.17. TEM bright field image of layer MTLP50. The lattice fringes of the 2H MoS_x (001) planes are clearly seen.

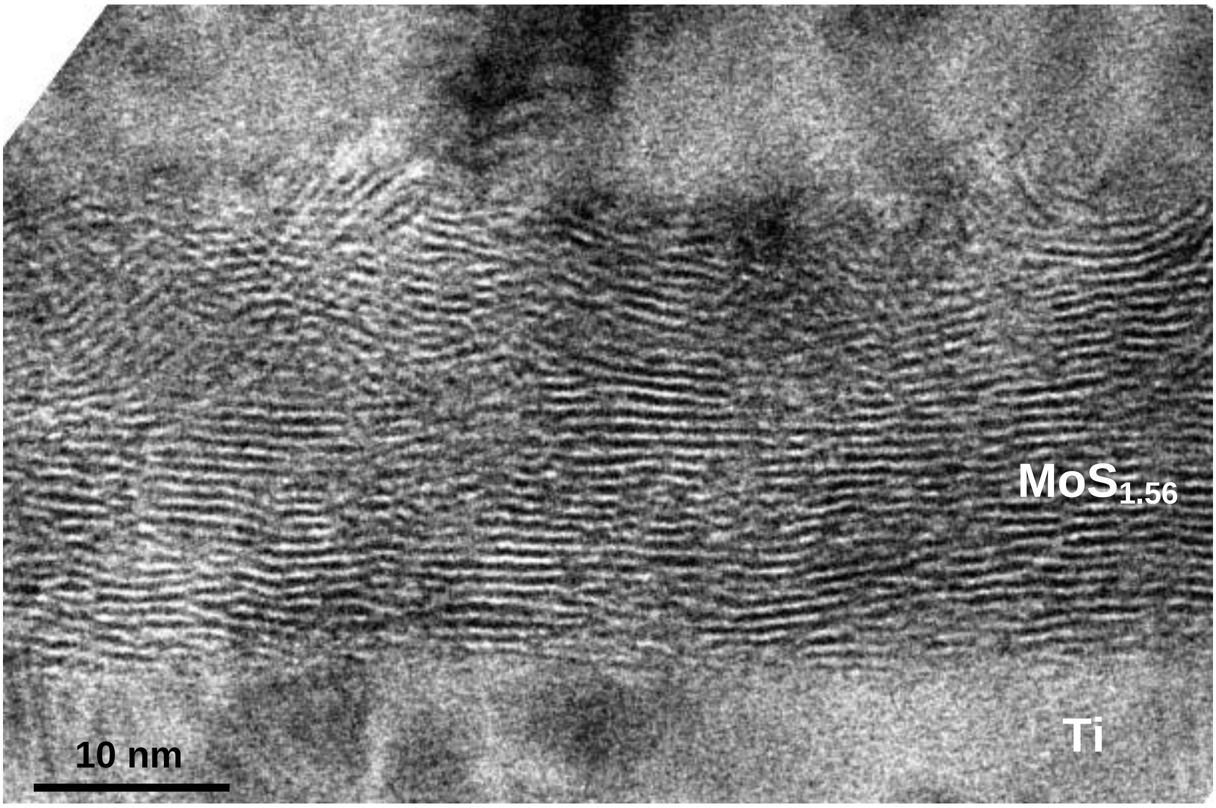

Fig. 8.18. TEM bright field image of layer MTLP100. The lattice fringes of the 2H MoS_x *(001) planes are clearly seen.*

8.3.4. MTHP multilayer coating

The SAED pattern of this coating is shown on Figure 8.19. Similarly to the SAED pattern of multilayer coating LTHP, diffraction arcs corresponding of both type I and type II 2H crystals are observed. The rest of the SAED pattern consists of diffraction rings corresponding to fcc TiN polycrystalline structure and the diffraction spots of the monocrystalline Si(100) substrate.

8.3.4.1. Layer MTHP-50

As seen from Figure 8.20, this layer consists of cubic crystals (encircled in red) embedded in an amorphous matrix. The overall chemical composition of the layer corresponds to $MoS_{1.00}$.

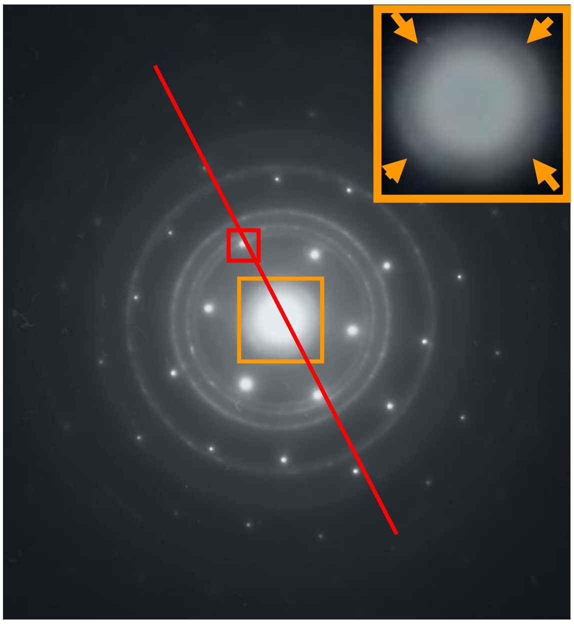

Fig. 8.19. SAED pattern of multilayer coating MTHP. The red line denotes the planes parallel to the surface of the Si(100) substrate. The red square shows the Si(100) diffraction spot. The orange arrows show the 2H MoS_2 (001) diffraction arcs.

8.3.4.2. Layer MTHP-25

This layer consists of type II 2H crystals embedded in an amorphous matrix, as evident from Figure 8.21. Sharp transition is observed from this structure to type I 2H crystals at certain points of the layer. The overall layer stoichiometry corresponds to $MoS_{1.17}$.

8.3.4.3. Layers MTHP0, MTHP50 and MTHP100

These 3 layers have very similar structures. It is difficult to estimate the presence of amorphous phase in the layers, as seen from Figures 8.22, 8.23 and 8.24, respectively. The first 3-5 nm of the layers consist of type II 2H crystals. After that a sharp transition to type I 2H structure is observed. The overall layer stoichiometry corresponds to $MoS_{1.78}$, $MoS_{2.10}$ and $MoS_{1.78}$ for layers MTHP0, MTHP50 and MTHP100, respectively.

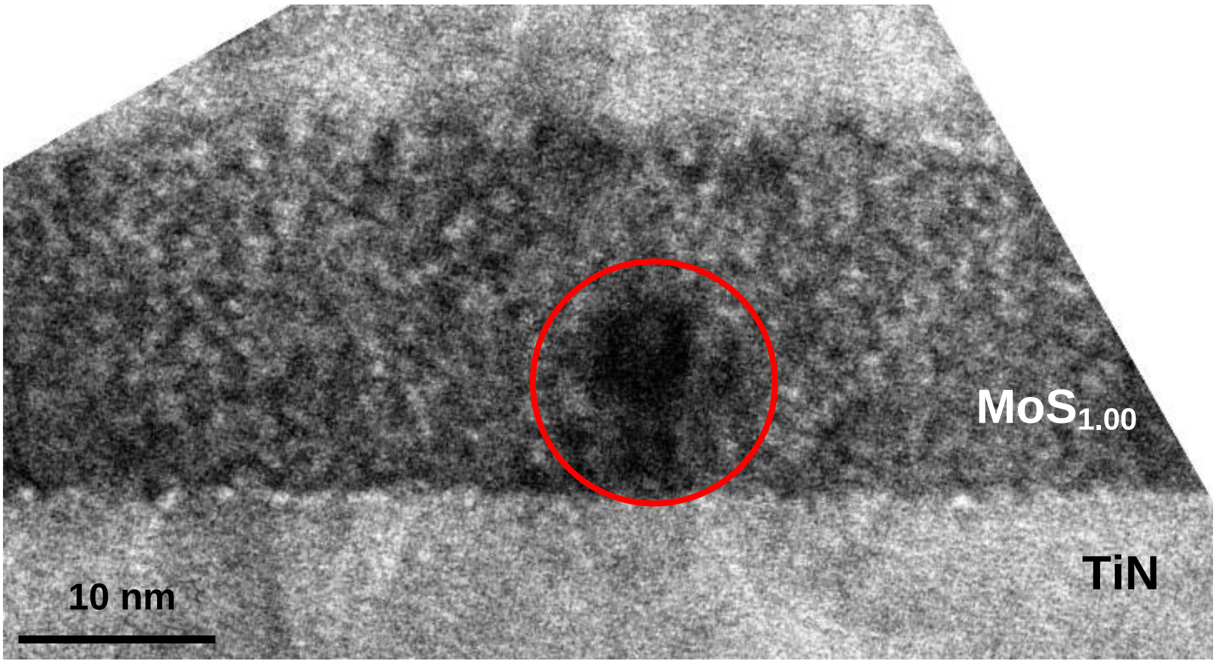

Fig. 8.20. TEM bright field image of layer MTHP-50. The red circle shows some of the cubic crystals.

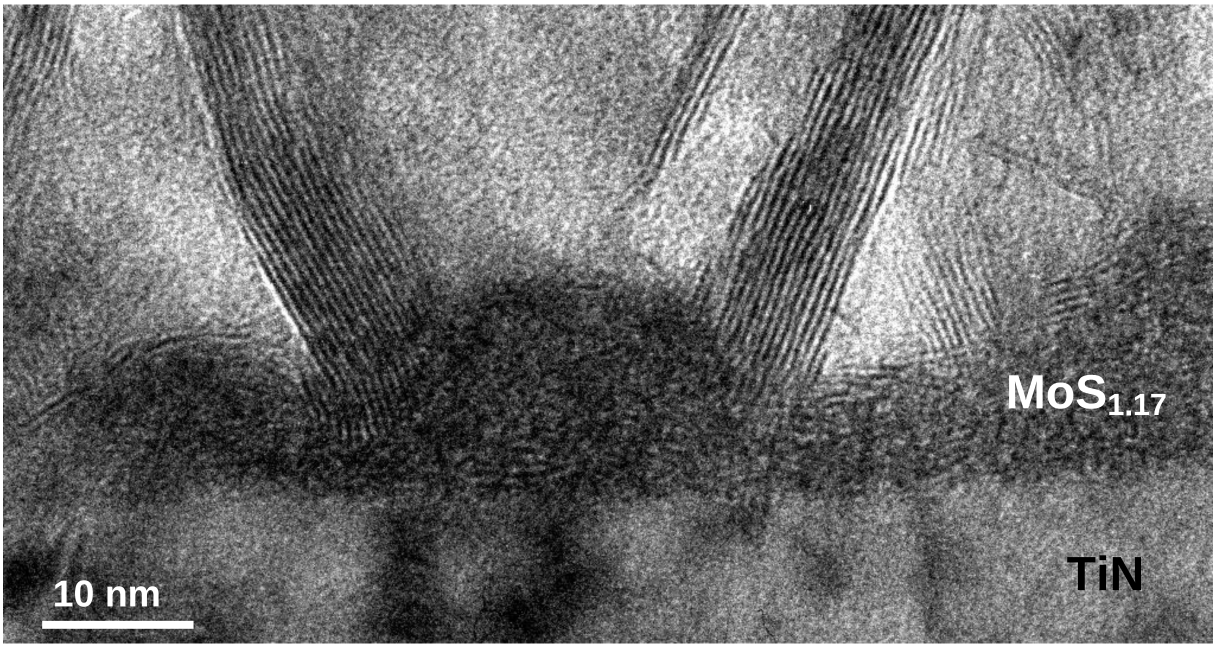

Fig. 8.21. TEM bright field image of layer MTHP-25. Note the type II 2h MoS_x *crystals*

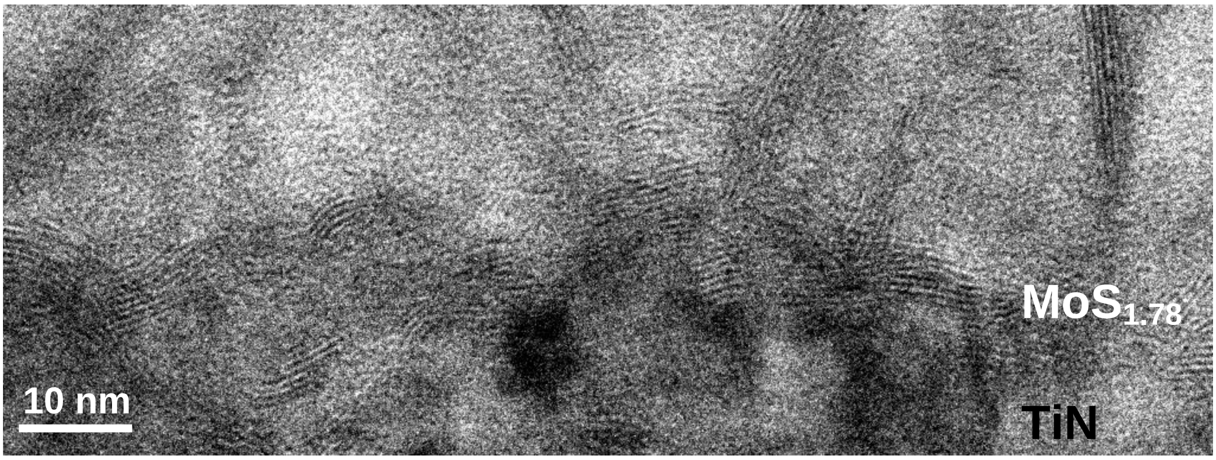

Fig. 8.22. TEM bright field image of layer MTHP0. Note the type II 2H MoS_x *crystals.*

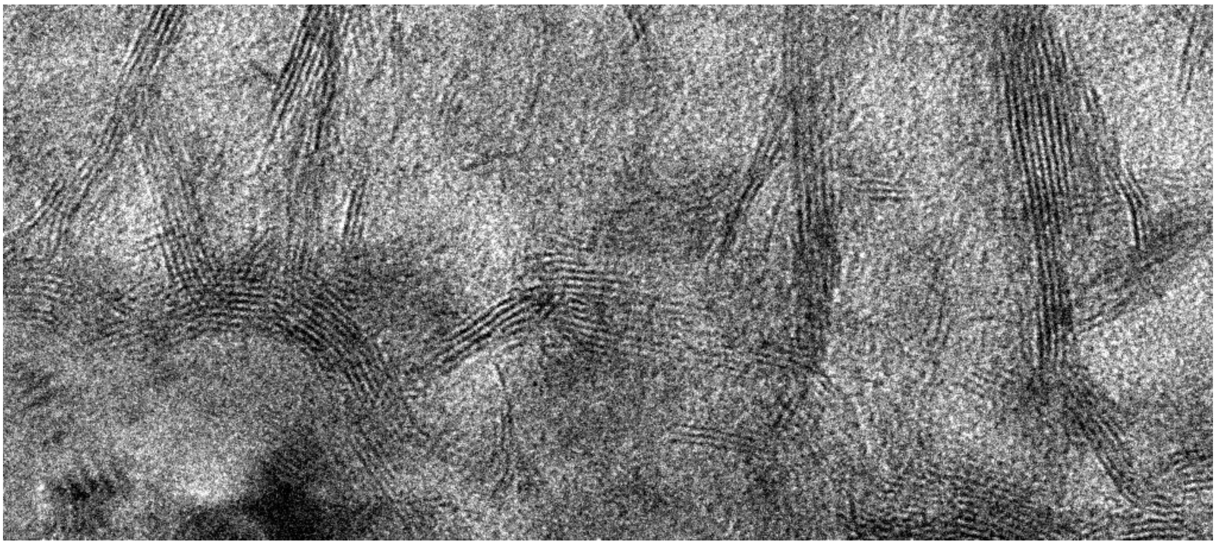

Fig. 8.23. TEM bright field image of layer MTHP50. Note the type II 2H MoS_x *crystals.*

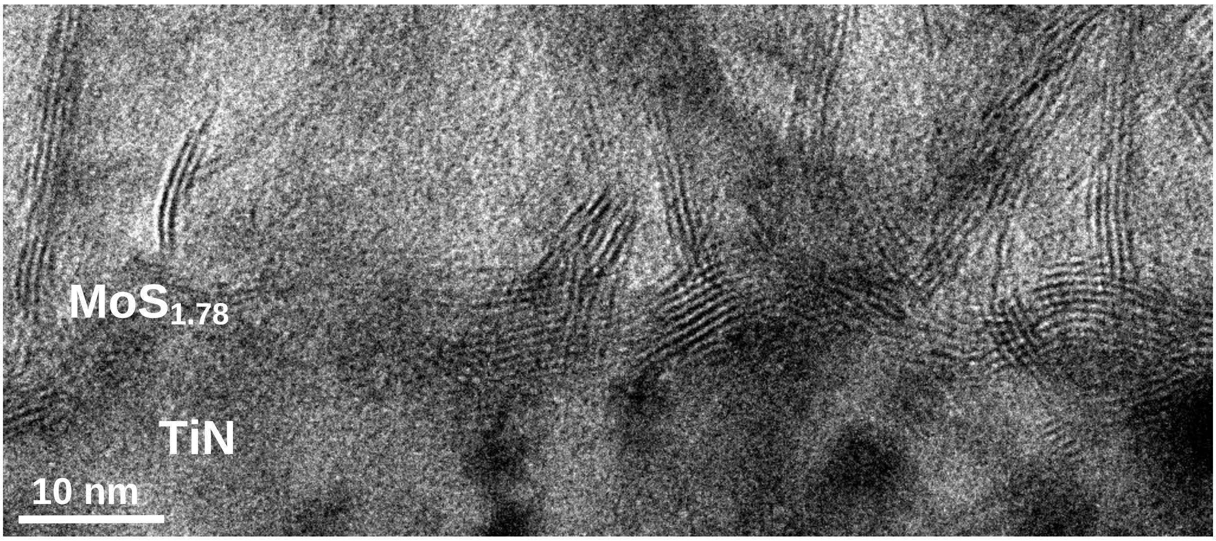

Fig. 8.24. TEM bright field image of layer MTHP100. Note the type II 2H MoS_x *crystals.*

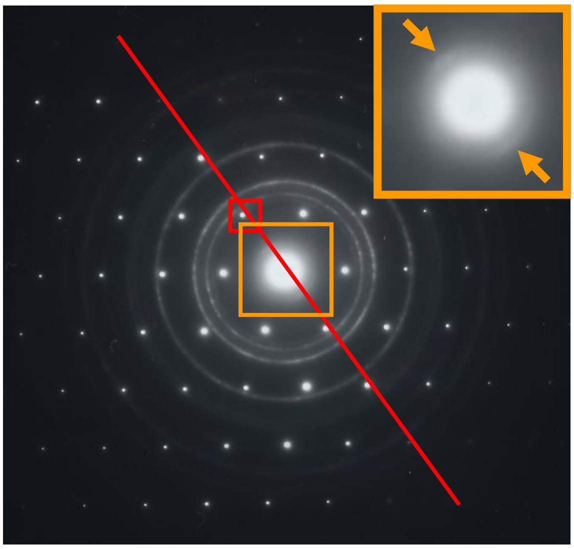

Fig. 8.25. SAED pattern of multilayer coating HTLP. The red line denotes the planes parallel to the surface of the Si(100) substrate. The red square shows the Si(100) diffraction spot. The orange arrows show the 2H MoS_2 *(001) diffraction arcs.*

8.3.5. HTLP multilayer coating

The SAED pattern of this multilayer is shown on Figure 8.25. Two weak diffraction arcs (as shown by arrows in the insert) suggest the presence of type II 2H crystals in the coating. The remaining phases that can be identified from the pattern are fcc TiN and the monocrystalline Si(100) substrate.

8.3.5.1. Layer HTLP-50

As seen from Figure 8.26, this layer consists of cubic crystals. Very little (if any) amorphous phase presents in the layer as evident from the strong contrast in the HTLP-50 layer on the dark-field image shown on Figure 8.26b. The chemical composition of the layer corresponds to $MoS_{0.88}$.

8.3.5.2. Layer HTLP-25

The structure of this layer, as seen from Figure 8.27, is very similar to that of layer HTLP-50. The chemical composition of layer HTLP-25 corresponds to $MoS_{0.82}$.

8.3.5.3. Layer HTLP0

In this layer 3 phases coexist: type II 2H (encircled in red) and cubic (encircled in blue) crystals are embedded in an amorphous matrix, as seen from Figure 8.28. The stoichiometry of the layer corresponds to $MoS_{1.22}$.

8.3.5.4. Layer HTLP50

This layer consists of type I and type II 2H crystals. Some amorphous phase is also evident from Figure 8.29. Initially the layer starts growing as type II 2H crystals embedded in the amorphous matrix. After the first 20-30 nm of the growth the structure of the layer starts switching to type I. The overall chemical composition of the layer corresponds to $MoS_{1.33}$.

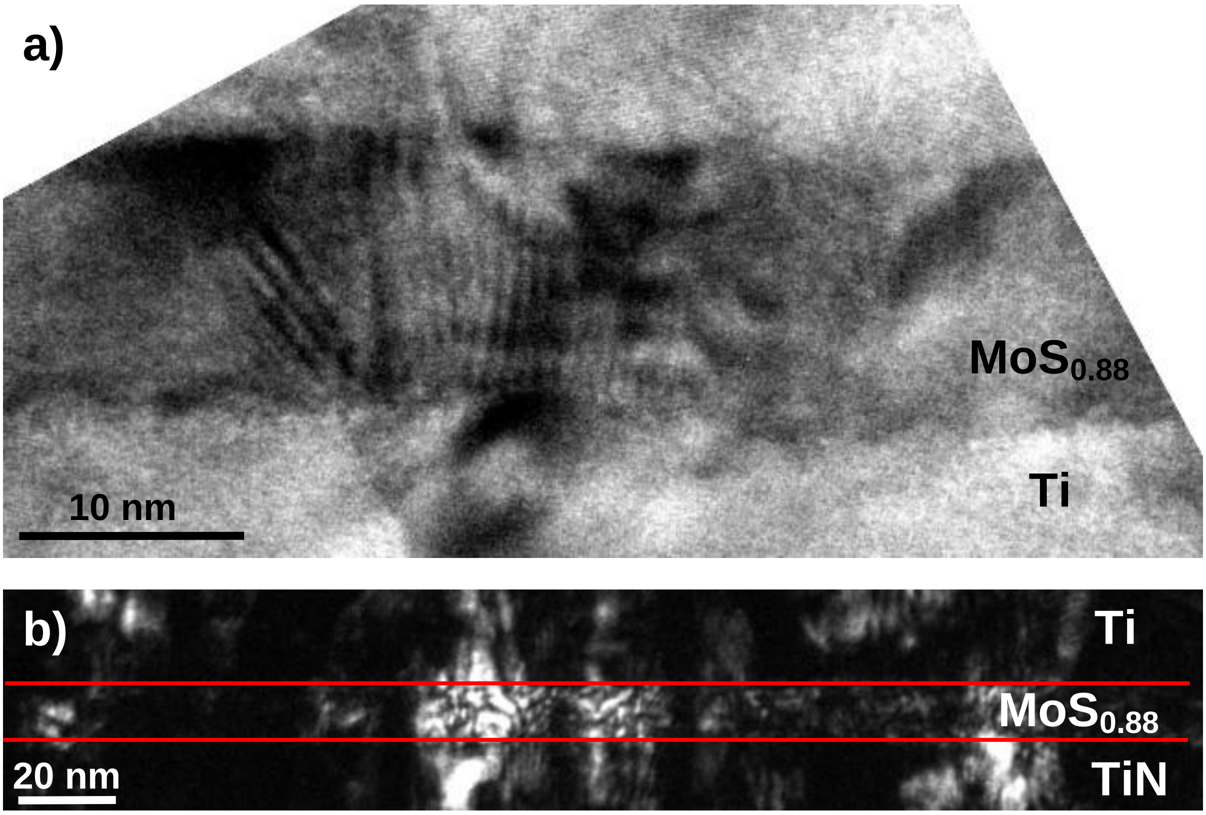

Fig. 8.26. a) TEM bright field image of layer HTLP-50; b) TEM dark field image of the same layer taken from the 111 diffraction rings of the fcc TiN crystalline pase. Note the local epitaxy.

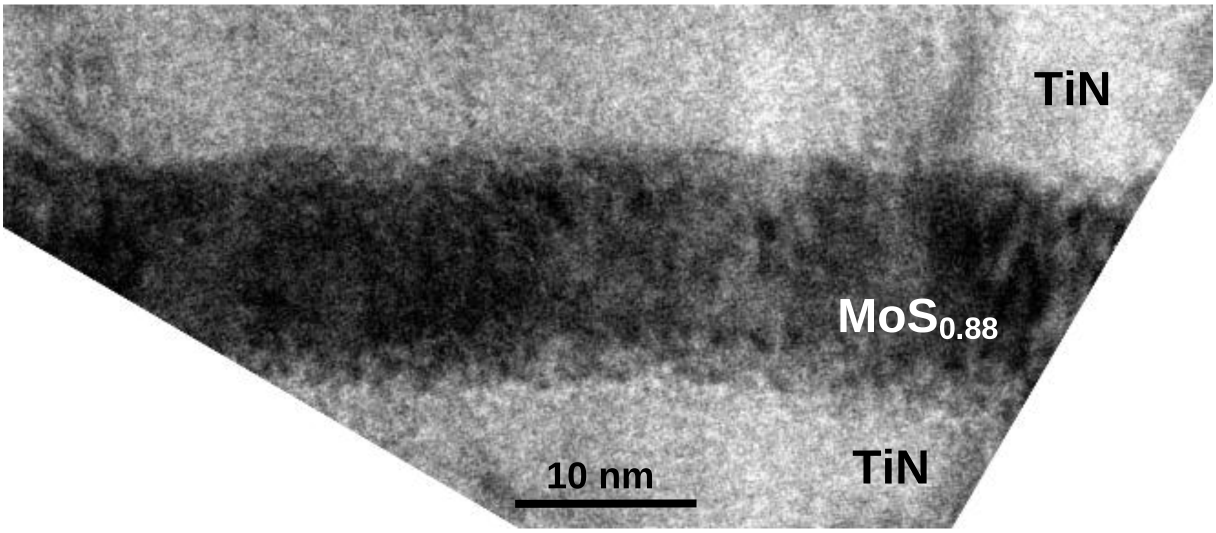

Fig. 8.27. TEM bright field image of layer HTLP-25.

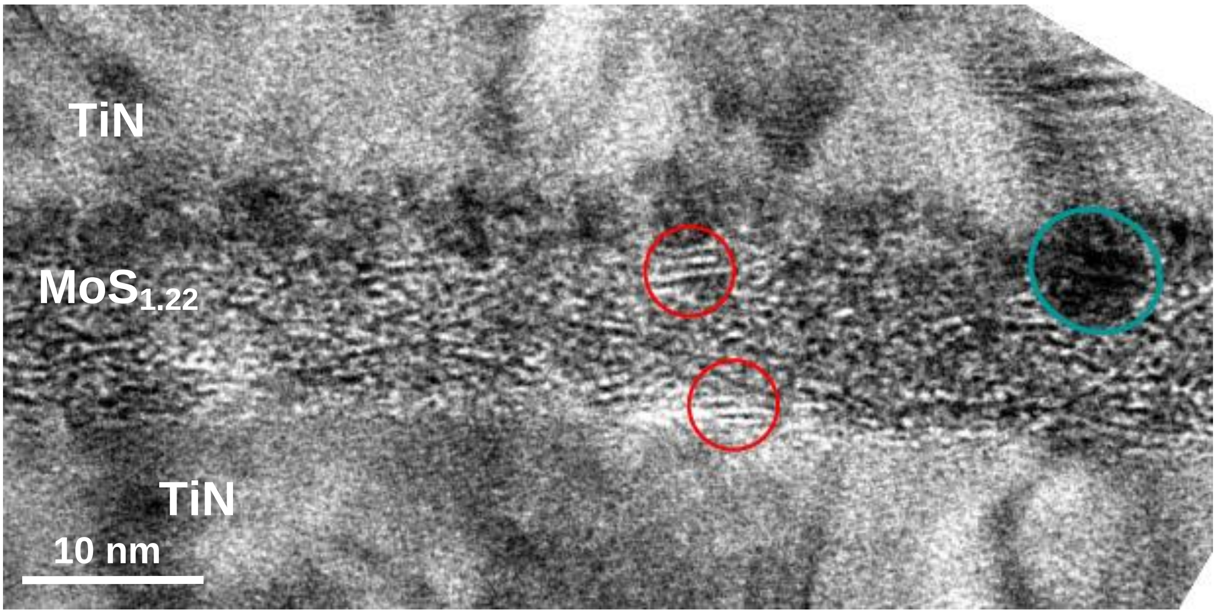

Fig. 8.28. TEM bright field image of layer HTLP0. The red circles show some of the 2H crystals and the blue circle shows a cubic crystal.

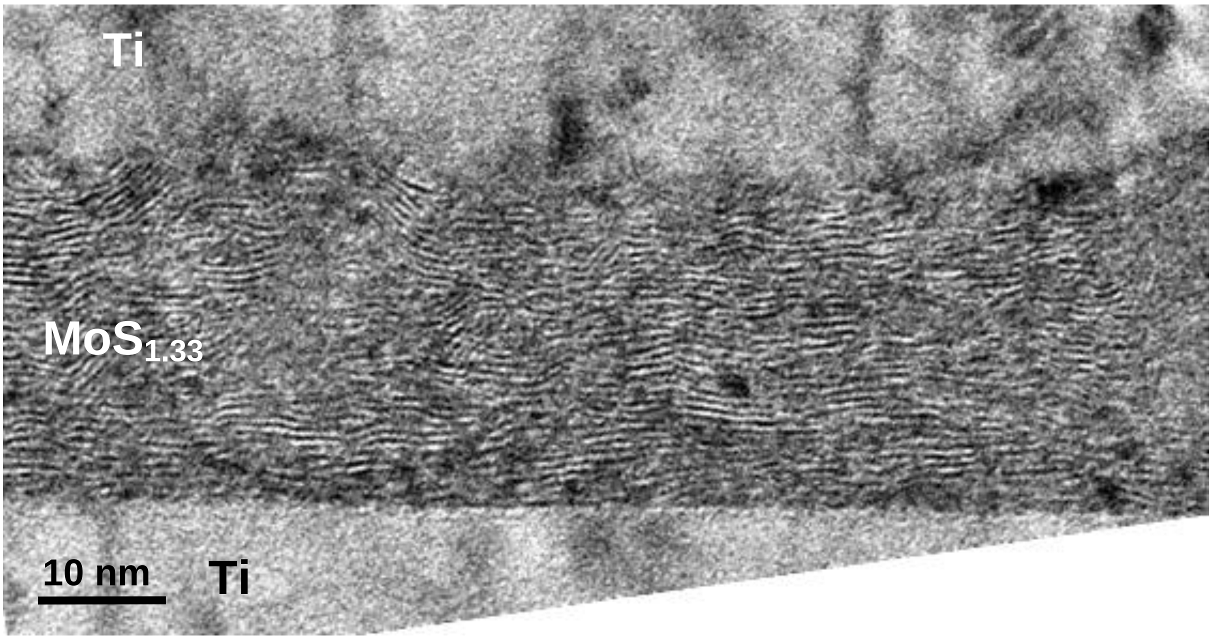

Fig. 8.29. TEM bright field image of layer HTLP50. The lattice fringes of the 2H MoS_x *(001) planes are clearly visible.*

8.3.5.5. Layer HTLP100

This layer has a structure very similar to that of layer HTLP50, as seen from Figure 8.30. The stoichiometry of the layer corresponds to $MoS_{1.22}$.

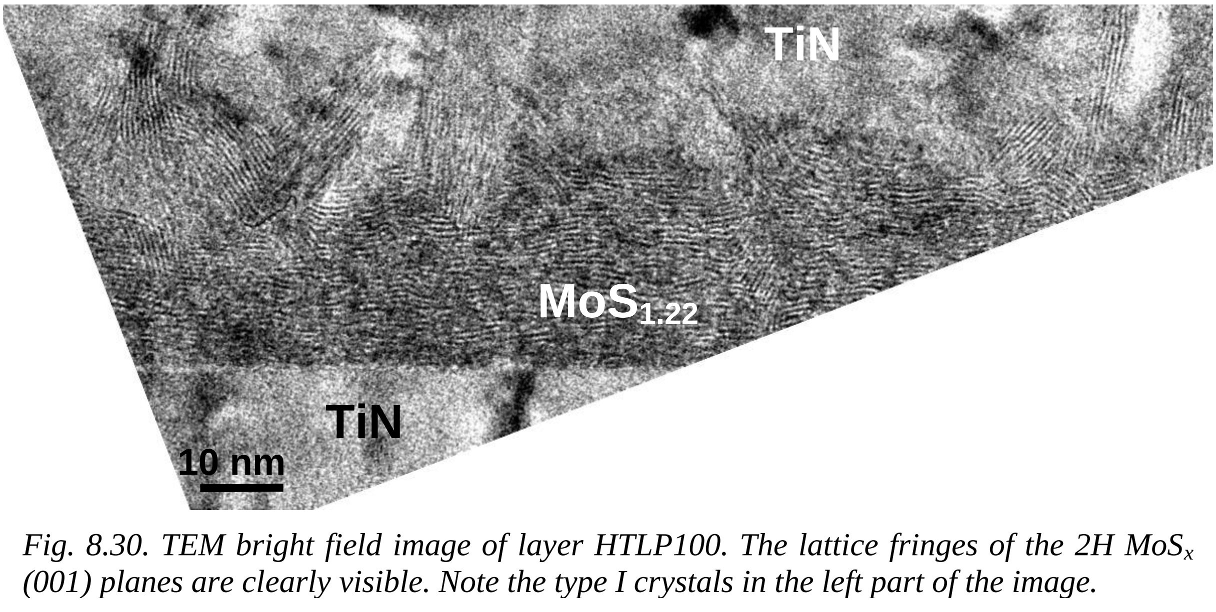

Fig. 8.30. TEM bright field image of layer HTLP100. The lattice fringes of the 2H MoS_x *(001) planes are clearly visible. Note the type I crystals in the left part of the image.*

8.3.6. HTHP multilayer coating

The SAED pattern of this multilayer coating reveals the existence of both type II and type I 2H crystals (as shown in the insert) and fcc TiN crystals, as seen from Figure 8.31.

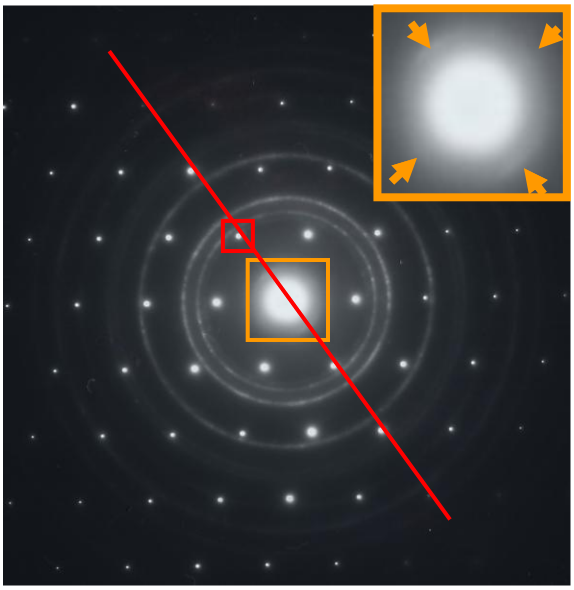

Fig. 8.31. SAED pattern of multilayer coating HTHP. The red line denotes the planes parallel to the surface of the Si(100) substrate. The red square shows the Si(100) diffraction spot. The orange arrows show the 2H MoS_2 *(001) diffraction arcs.*

8.3.6.1. Layer HTHP-50

As seen from Figure 8.32, this layer consists of cubic crystals. The stoichiometry of the layer corresponds to $MoS_{0.82}$.

8.3.6.2. Layer HTHP-25

This layer consists of 2H and cubic crystals embedded in an amorphous matrix, as evident from Figure 8.33. The chemical composition of the layer corresponds to $MoS_{1.17}$.

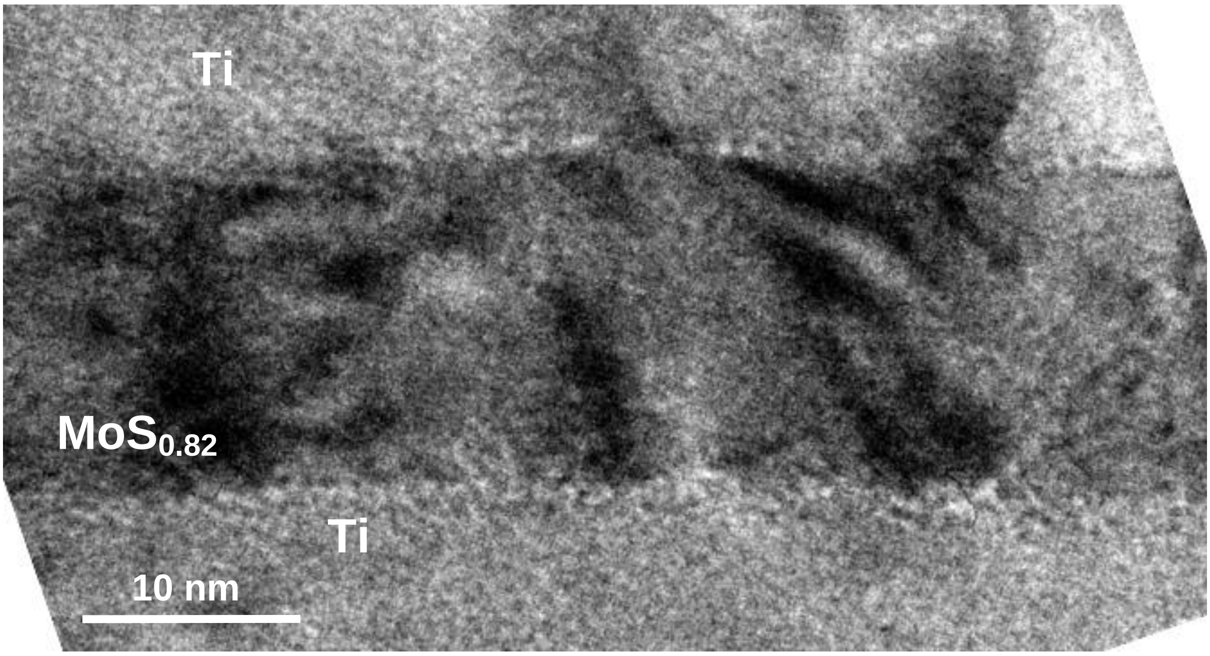

Fig. 8.32. TEM bright field image of layer HTHP-50.

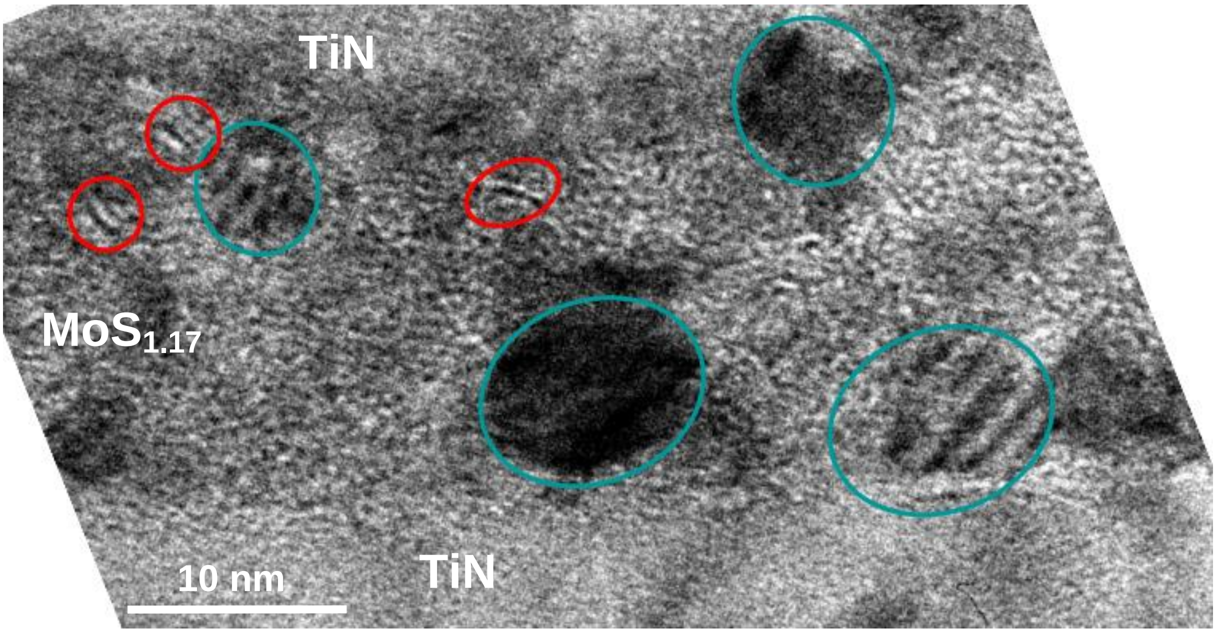

Fig. 8.33. TEM bright field image of layer HTHP-25. The red circles show some of the 2H crystals and the blue circles show some of the cubic crystals.

8.3.6.3. Layer HTHP0

In this layer, as seen from Figure 8.34, type II 2H crystals are embedded in an

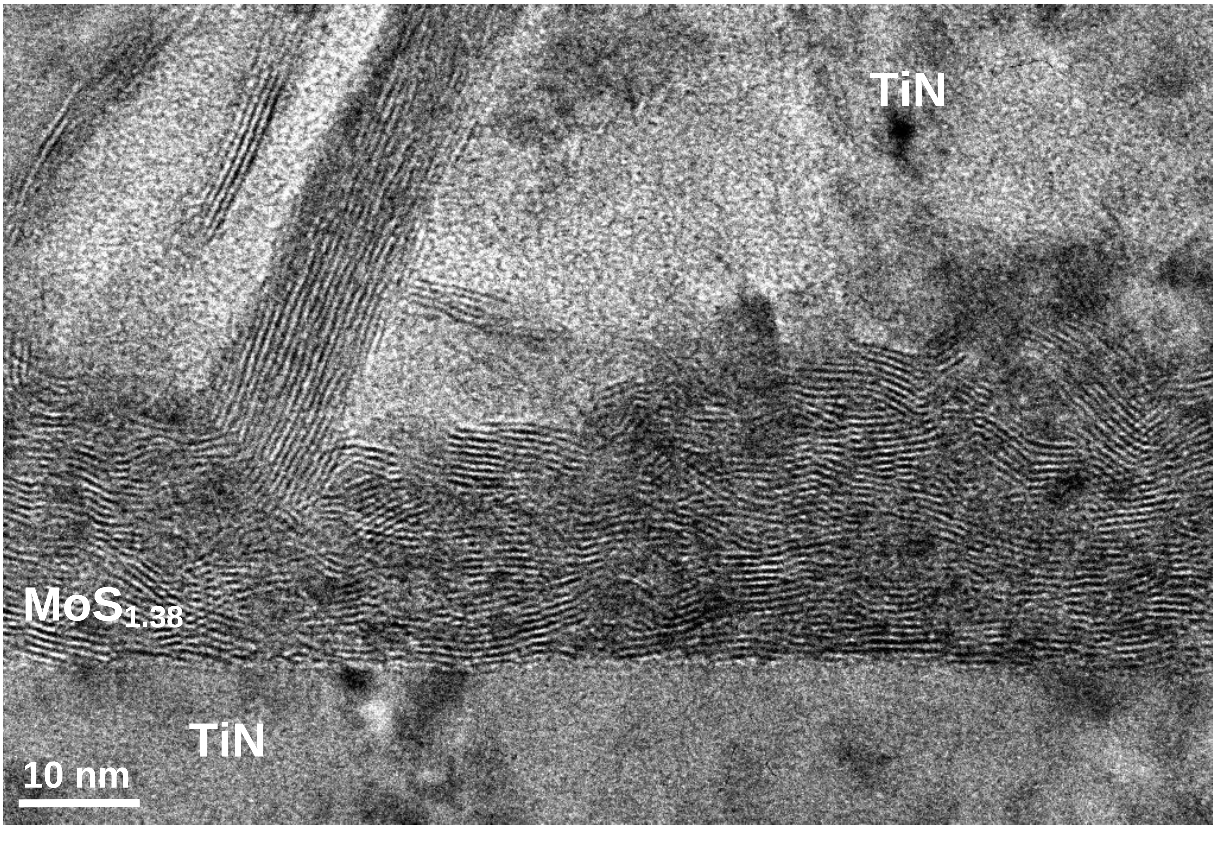

Fig. 8.34. TEM bright field image of layer HTHP0. Note the type I 2H MoS$_x$ crystals in the left part of the image.

amorphous matrix. At certain points after 20-30 nm of growth the structure switches to type II 2H crystals. The overall layer stoichiometry corresponds to $MoS_{1.38}$.

8.3.6.4. Layers HTHP50 and HTHP100

Layers HTHP50 and HTHP100 have very similar structures, shown on Figures 8.35

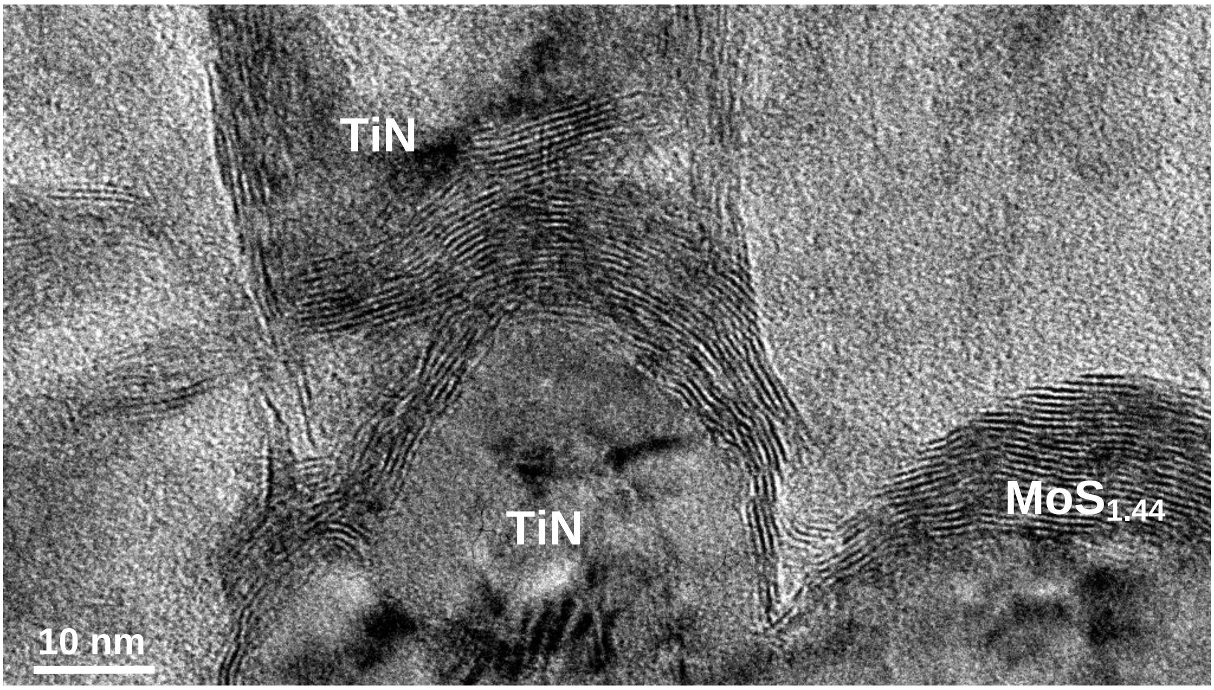

Fig. 8.35. TEM bright field image of layer HTHP50. The lattice fringes of the 2H MoS_x (001) planes are clearly visible.

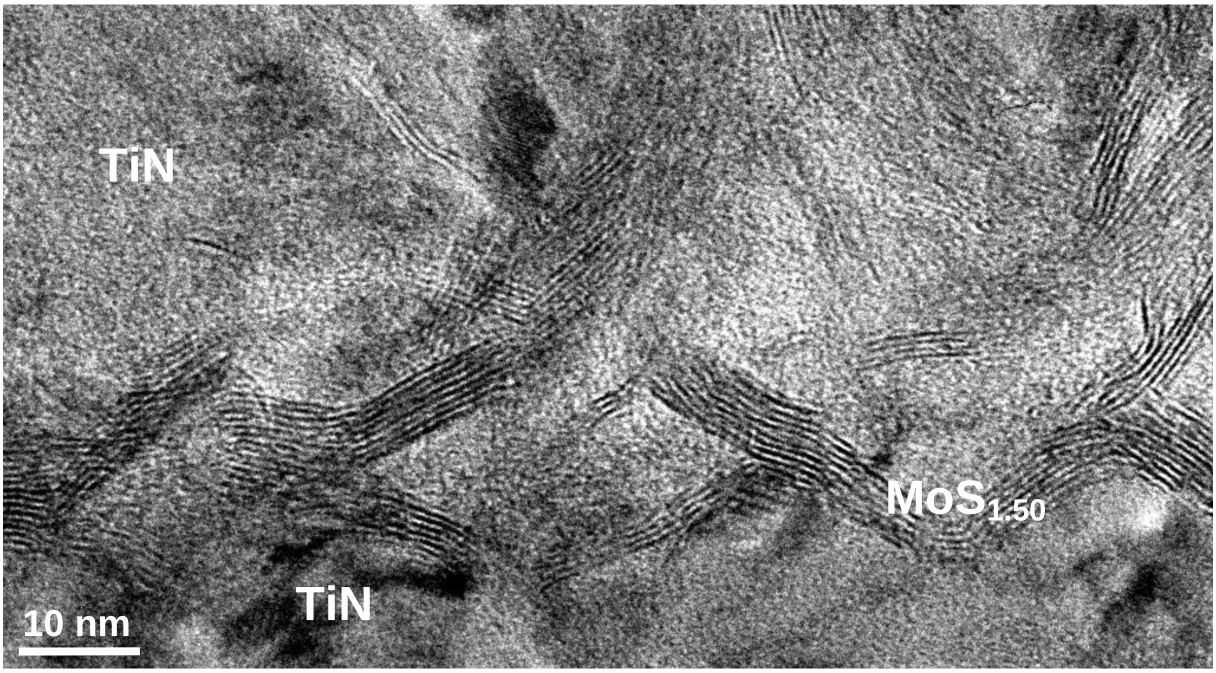

Fig. 8.36. TEM bright field image of layer HTHP100. The lattice fringes of the 2H MoS_x (001) planes are clearly visible.

and 8.36, respectively. In both cases in the initial 10-20 nm of layer growth the structure is crystalline, type II 2H. After that the structure switches to type I 2H. The chemical compositions of layers HTHP50 and HTHP100 are $MoS_{1.44}$ and $MoS_{1.50}$, respectively.

8.4. MoS_x layers and influence of the parameters: summary

For simplicity, the structure and chemical compositions of all MoS_x layers described so far are summarized on Figure 8.37 and Figure 8.38 for the low and high pressure depositions, respectively. The chemical compositions of the MoS_x layers are graphically represented on Figure 8.37 and 8.38, respectively. Based on these findings, the following conclusions about the initial stages of growth of MoS_x can be made:

8.4.1. Low pressure experiments:

At low pressure, temperature and bias voltage have very strong influence on the morphology and chemistry of the early-stage growth of MoS_x films. In general, negative bias voltages (-50 and -25 V) result in poorer S content compared to non-negative (0, 50 and 100 V) ones. This is clearly related to the resputtering of S by the Ar^+ from the plasma at negative bias voltages. Temperature, however, has a more complex influence. It influences the sticking coefficient of the S atoms at the surface of the growing film. Thus at higher temperature the probability of desorbtion of the S atom before it is bonded is greater than that at lower temperature. Crystallisation of 2H MoS_x apparently needs temperature higher than 150 ºC at zero bias voltage although the S content is sufficient for the crystallization of 2H phase to take place (comparing the films deposited at 150 ºC, 0 V bias and 380 ºC, 0 V bias – they have the same stoichiometry). Although with lower S content, the film deposited at 150 ºC, -25 V, is hexagonal because the energy needed for crystallization is supplied by Ar^+. At the same time, crystallization is an important factor for S “gettering” of the film. Vacancies at crystalline surfaces act as S bonding “traps” much better than the amorphous surfaces. Compare the rapid increase of S content of the films deposited at 150 ºC, (0 V and 50 V) (amorphous to crystalline) compared to the decrease in S content of the films deposited at 250 ºC (0V and 50 V) that are both crystalline.

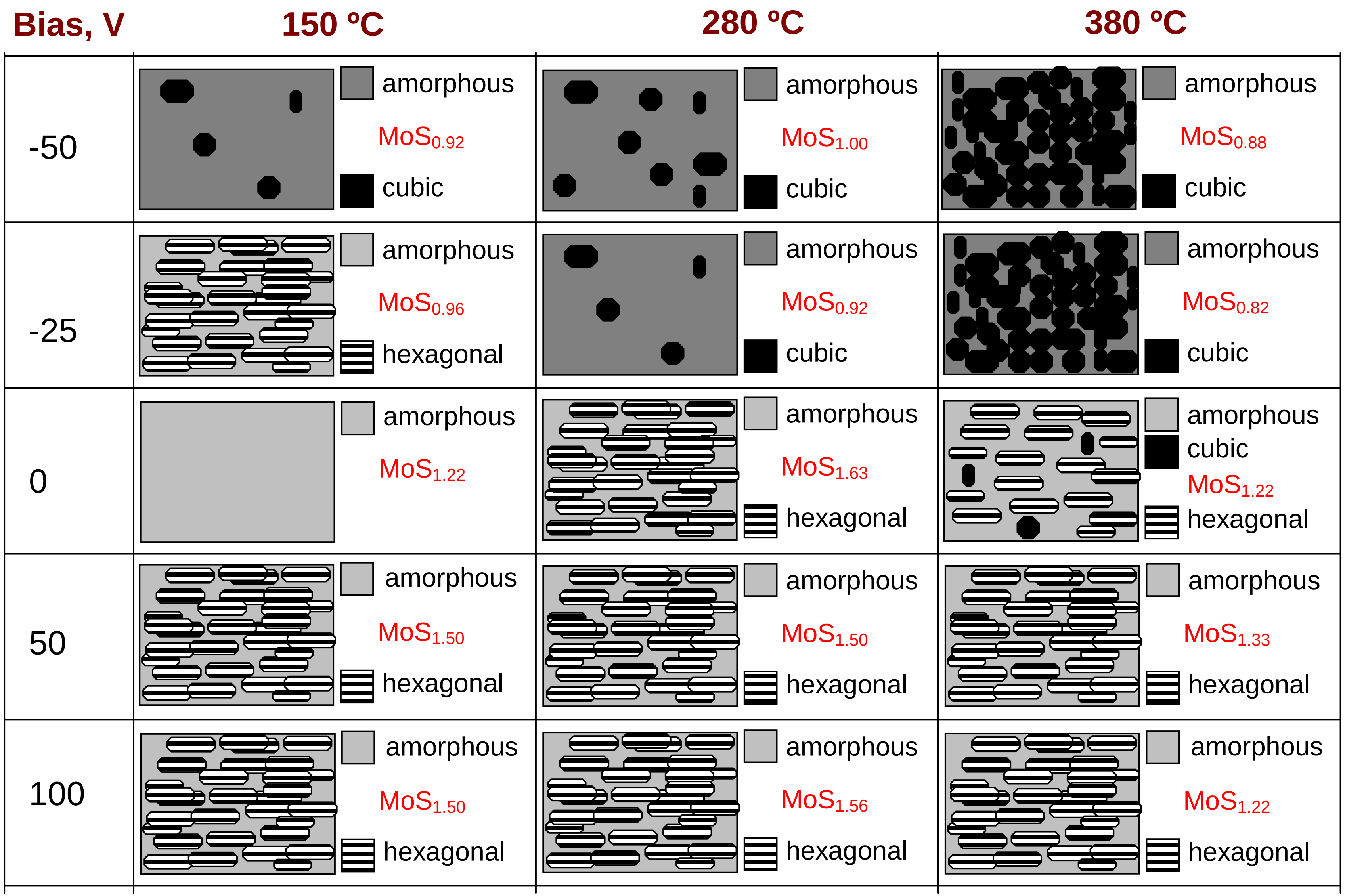

Bias, V	150 °C	280 °C	380 °C
-50	amorphous $MoS_{0.92}$ ■ cubic	amorphous $MoS_{1.00}$ ■ cubic	amorphous $MoS_{0.88}$ ■ cubic
-25	amorphous $MoS_{0.96}$ ▤ hexagonal	amorphous $MoS_{0.92}$ ■ cubic	amorphous $MoS_{0.82}$ ■ cubic
0	amorphous $MoS_{1.22}$	amorphous $MoS_{1.63}$ ▤ hexagonal	amorphous ■ cubic $MoS_{1.22}$ ▤ hexagonal
50	amorphous $MoS_{1.50}$ ▤ hexagonal	amorphous $MoS_{1.50}$ ▤ hexagonal	amorphous $MoS_{1.33}$ ▤ hexagonal
100	amorphous $MoS_{1.50}$ ▤ hexagonal	amorphous $MoS_{1.56}$ ▤ hexagonal	amorphous $MoS_{1.22}$ ▤ hexagonal

Fig. 8.37. Summary of the deposition conditions – structure and chemical composition relationship for MoS_x layers deposited at 0.4 Pa

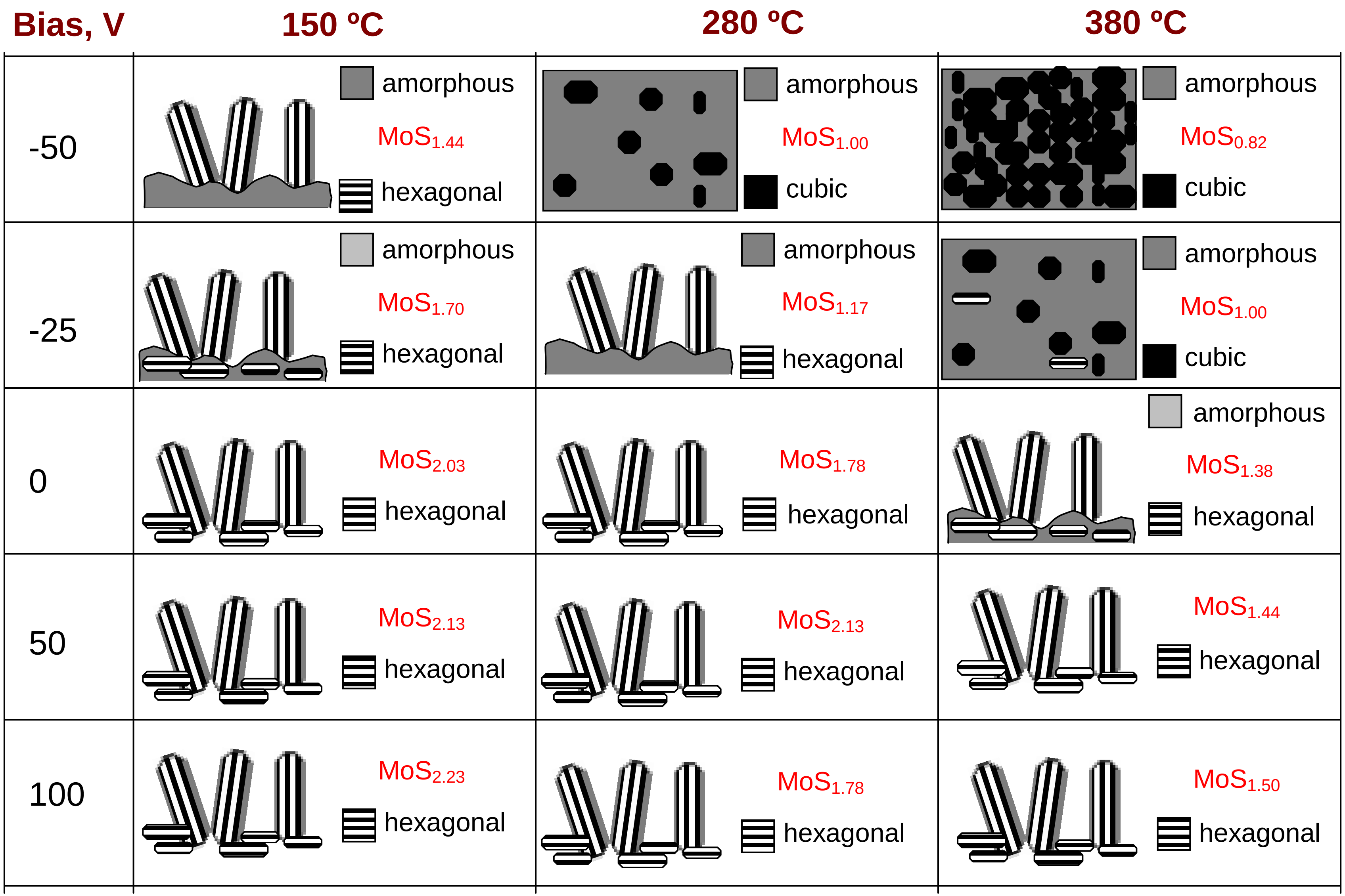

Bias, V	150 °C	280 °C	380 °C
-50	amorphous $MoS_{1.44}$ hexagonal	amorphous $MoS_{1.00}$ cubic	amorphous $MoS_{0.82}$ cubic
-25	amorphous $MoS_{1.70}$ hexagonal	amorphous $MoS_{1.17}$ hexagonal	amorphous $MoS_{1.00}$ cubic
0	$MoS_{2.03}$ hexagonal	$MoS_{1.78}$ hexagonal	amorphous $MoS_{1.38}$ hexagonal
50	$MoS_{2.13}$ hexagonal	$MoS_{2.13}$ hexagonal	$MoS_{1.44}$ hexagonal
100	$MoS_{2.23}$ hexagonal	$MoS_{1.78}$ hexagonal	$MoS_{1.50}$ hexagonal

Fig. 8.38. Summary of the deposition conditions – structure and chemical composition relationship for MoS_x layers deposited at 2.4 Pa

8.4.2. High pressure experiments:

The temperature and bias voltage play a very important role in controlling the chemistry and structure of the ealry stages of MoS_x growth also at higher deposition pressure. Whether one phase or another will present in the layers depends on the S content which, in turn, depends on both temperature and bias voltage. Negative bias voltages and high temperature result in lower S content which yields layers of cubic crystals distributed in amorphous MoS_x phase. In all the cases where hexagonal MoSx was present, edge-growth was triggered after a certain thickness of the underlayer. At high pressures, the arriving species have lower energy due to the increased number of thermalising collisions with the species present in the gas phase. This results in better adsorbtion of the S and less renucleation during film growth. Hence, the film grows closer to its thermodynamic equilibrium mode, which is type I [65].

8.5. Functional TiN/MoS_x coating

After studying the influence of the deposition conditions on the structure and the chemical composition of MoS_x layers deposited on TiN layers, appropriate structure of the MoS_x layers should be selected for deposition of a functional TiN/MoS_x multilayer coating and its structure and tribological properties are to be studied.

8.5.1. Introduction

As seen from the above findings, several possible choices for the structure of the MoS_x layers in a functional TiN/MoS_x multilayer coatings exist. Cubic structure is not promising since the S content in it is very low. MoS_x coatings with $x<1$ have no lubricating properties, as demonstrated by Dimigen et al. [34] and Moser et al [36]. MoS_x layers where transition to type II structures is observed are also not suitable since this orientation of the MoS_x crystals does not provide a dense structure. Besides, type II MoS_x coatings have been reported to have inferior friction and wear properties than type II coatings, as shown above. The same is valid for amorphous MoS_x coatings, Therefore, type II is obviously the best choice for the structure of MoS_x in TiN/MoS_x multilayer coatings. Best tribological performance was reported for MoS_x coatings with $x=1.5$ compared to coatings with other values of x [34], [18], [36]. Therefore, type II $MoS_{1.5}$ was chosen for the MoS_x layers in the functional TiN/MoS_x multilayer coating. The deposition conditions at which type II $MoS_{1.5}$ is obtained correspond to these of layer MTLP50 and MTLP100. To avoid possible intensive electron heating of the substrate, the lower bias voltage (50 V) was selected for the deposition of the $MoS_{1.5}$ layers.

8.5.2. Experimental details

The TiN layers were deposited at the same pressure and temperature (MTLP conditions) as the $MoS_{1.5}$ layers but at zero substrate bias (grounded substrate) based on previous laboratory experience. The thickness of the layers was selected to be 10 nm for the TiN layers and 5 nm for the $MoS_{1.5}$ layers so the expected coating structure is shown of Figure 8.39. The coating was deposited on substrates described in Section 6.

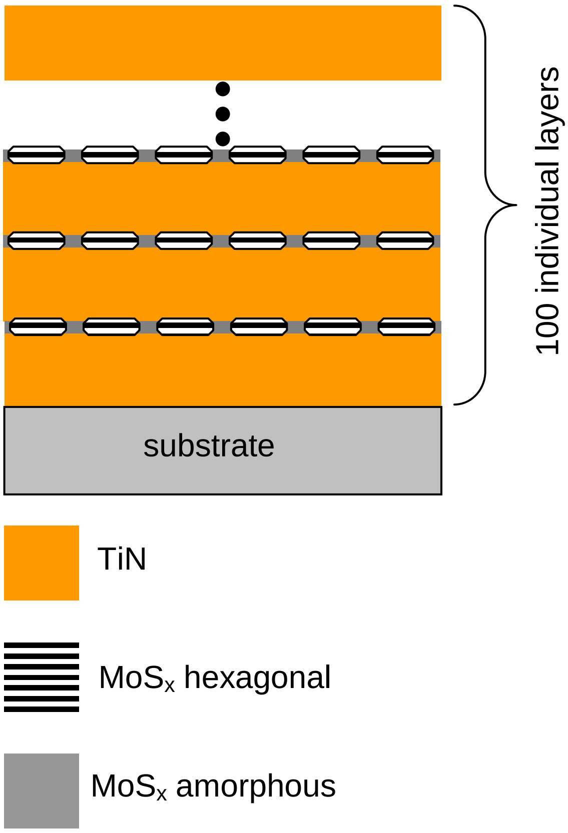

Fig. 8.39. Expected structure of the functional TiN/$MoS_{1.5}$ multilayer coating.

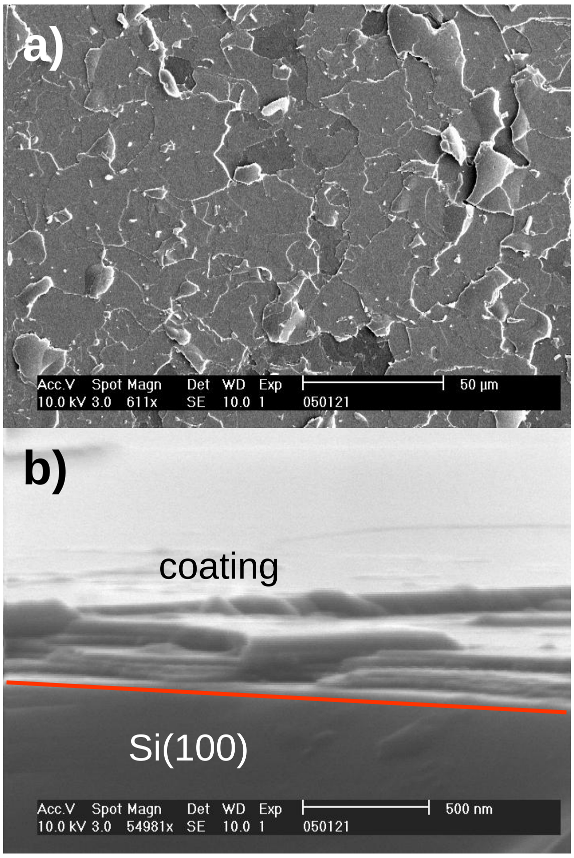

Fig. 8.40. SEM images of the functional TiN/$MoS_{1.5}$ functional multilayer coating: a) plain view; b) side view of a cleaved coated Si(100) wafer. The red line helps separating the coating from the substrate.

8.5.3. Structure

The films deposited this way have very low cohesive strength and delaminate as shown on Figure 8.40. Apparently, the cohesion of the $MoS_{1.5}$ layers and/or their adhesion to the TiN layers are too weak to withstand the residual stress in the multilayer coating. No TEM specimens were possible to prepare from this coating.

8.5.4. Complementary experiment – TiN/MoS_x-Ti multilaers

8.5.4.1. Introduction

Since the combination TiN/type II $MoS_{1.5}$ does not posses the mechanical strength needed for tribological applications, a MoS_x-based solid lubricant substitute for the type II $MoS_{1.5}$ is to be found. This substitute must to meet the following requirements:

- Good adhesion to TiN
- Higher hardness than 2H MoS_2
- No presence of 2H crystals in order to improve cohesion

A well-studied candidate meeting these requirements is the MoS_x-Ti coating used as a solid lubricant benchmark. Hard, wear-resistant solid lubricant MoS_x-Ti coating has been successfully deposited on a TiN layer at MTLP conditions and 50 V substrate bias. Its structure is summarized on Figure 8.41.

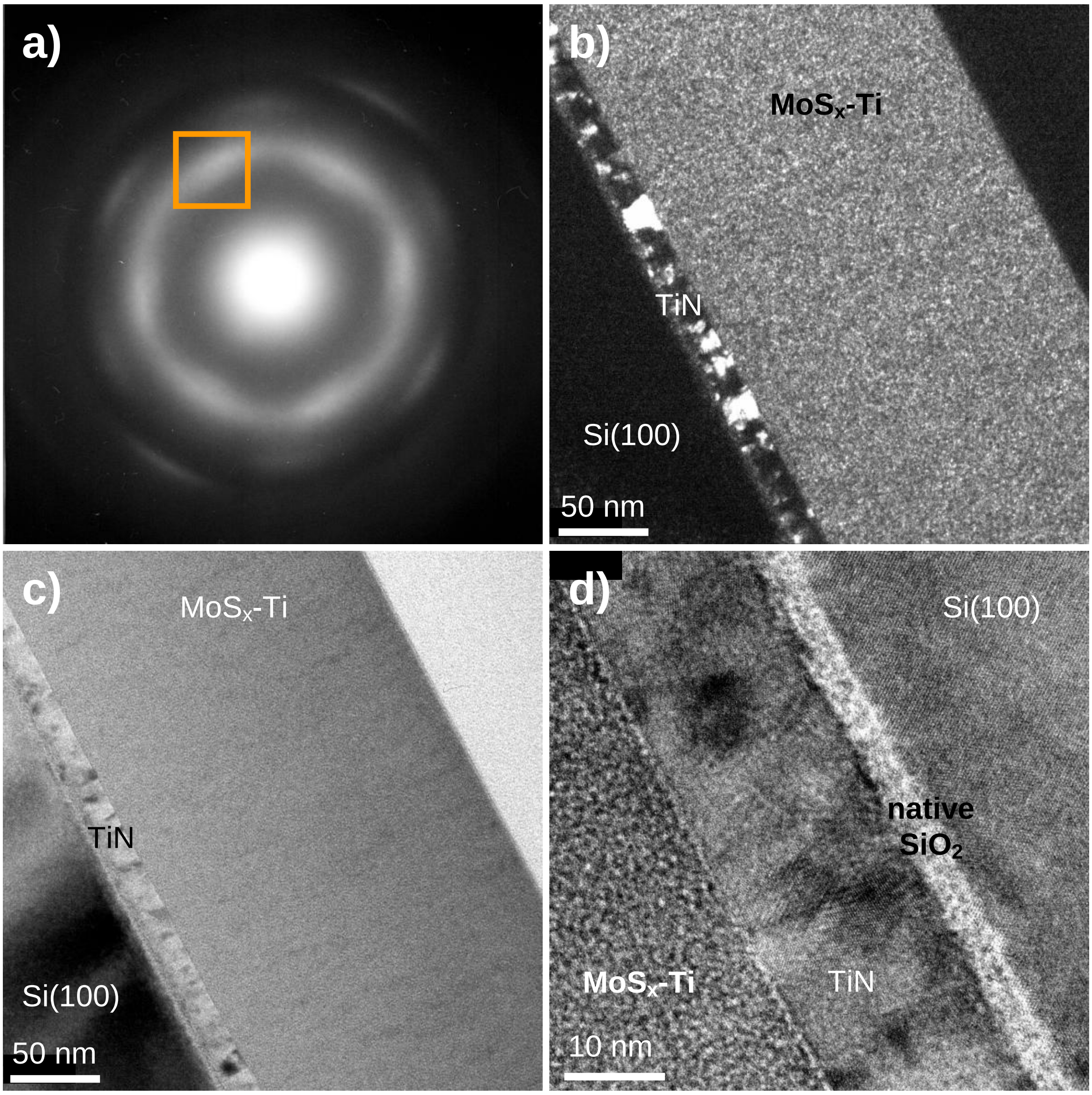

Fig. 8.41. TEM investigation of the structure of the MoS_x-Ti coating used as a substitute of the MoS1.5: a) SAED pattert; b) dark field image of the coating taken from the diffraction arc squared in orange; c, d) bright field images

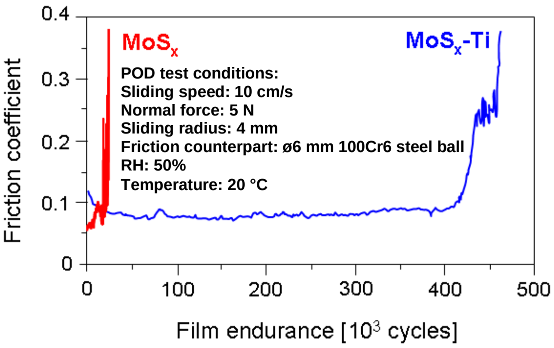

Fig. 8.42. Tribological properties of the MoS_x-Ti coating compared to a 2H MoS_x coating deposited in MTLP conditions (each 1.5 µm thick).

The coating consists of cubic crystals (as seen from the SAED pattern shown on Figure 8.41a. The size of these crystals is in the range of 2-3 nm as seen from the dark field image taken from the diffraction arc boxed in orange, as shown on Figure 8.41b. Some columns of these crystals, although not very well defined, are seen in the structure of the coating, as shown on Figure 8.41c. The interface of the coating with the TiN underlayer is sharp and no local epitaxy is observed as shown on Figure 8.41d. The coating has a wear life more than two orders of magnitude longer than that of a type II MoS_x coating deposited at the same conditions, as seen from Figure 8.42.

8.5.4.1. Experimental details

The MoS_x-Ti system described above was used for the deposition of a multilayer coating with structure shown previously on Figure 8.39. In this case, the MTLP50 layers were substituted by MoS_x-Ti layers with the same thickness of 5 nm. The thickness of the TiN layers was also kept the same as in the figure and they were deposited at 50 V substrate bias.

8.5.4.2. Structure

A TEM image of the resulting coating structure is shown on Figure 8.43. As seen from this figure, the structure of the coating has well defined layers of fcc TiN and quaiamorphous MoS_x-Ti with thickness of 10 and 5 nm, respectively. No local epitaxy is observed and the interfaces between the layers are sharp.

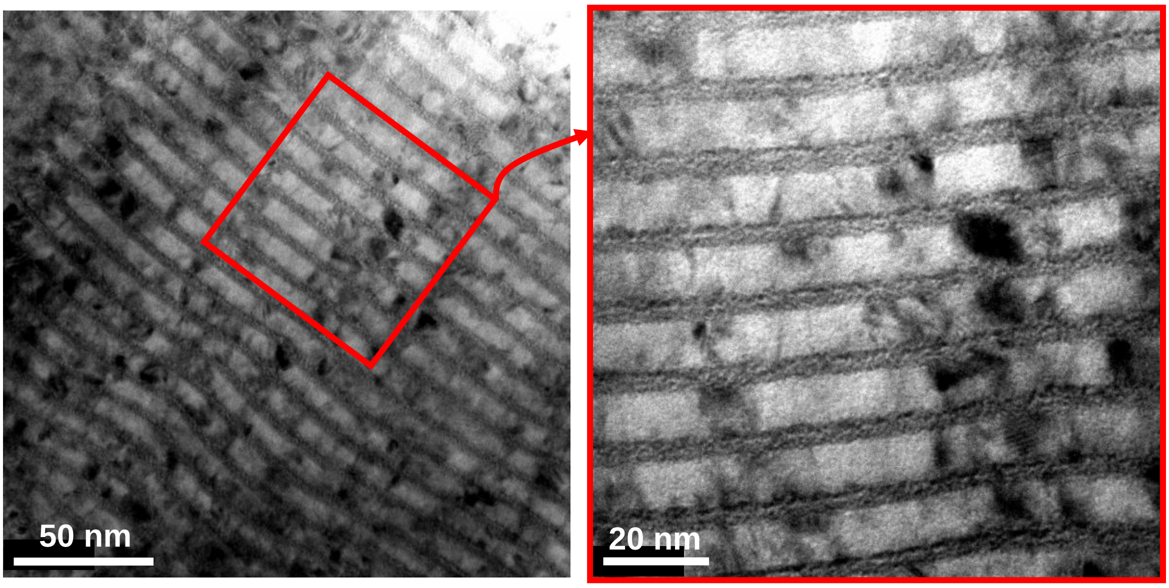

Fig. 8.43. TEM images of the functional TiN/MoS_x-Ti multilayer coating.

8.5.4.3. Tribological properties

The tribological properties of the TiN/MoS_x-Ti multilayer coating were studied with the POD method described in Section 5.1. The test conditions are also described there.

After the first few laps, however, total failure of the coating occurs as shown on Figure 8.44. The coating is immediately worn down to the substrate due to cohesive failure. Evidently, the superposition of the intrinsic coating stress with the stresses resulting from the friction test yields stress levels surpassing the cohesive strength of the coating. It is difficult to estimate whether the adhesion between the TiN and MoS_x-Ti layers or the strength of the MoS_x-Ti layers itself is responsible for the low cohesive strength of the coating.

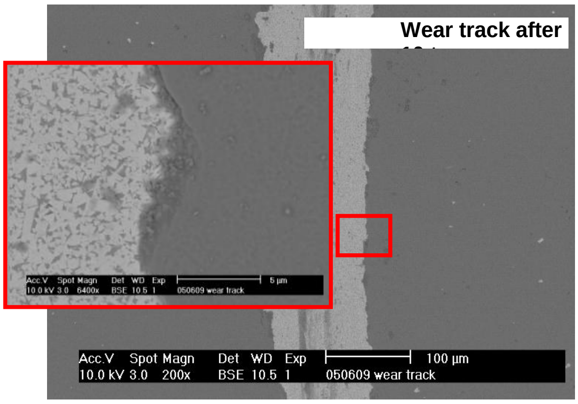

Fig. 8.44. SEM images of the wear track of the functional TiN/MoS_x-Ti multilayer coating after few laps in the POD test. The WC grains of the substrate are clearly seen in the insert.

8.5.4.4. Conclusions for section 8.5.

Combining layers of TiN with thickness of 10 nm and layers of 2H $MoS_{1.5}$ or MoS_x-Ti with thickness of 5 nm results in multilayer coatings with poor cohesive strength. The solid lubricant layers do not posses the strength and/or adhesion to the TiN layers sufficient to support the intrinsic stress of the coating and the stress posed by the friction in the given POD test conditions. It can be concluded that the TiN/MoS_x-based solid lubricant multilayer architecture is not suitable for combining the beneficial properties of a hard phase and a MoS_x-based solid lubricant.

Reference List to Section 8

1. Schintlmeister, W., Wallgram, W., Kanz, J., and Gigl, K. *Wear* 100 **1984** 153
2. Helmersson, U., Todorova, S., Barnett, S., Sundgren, J., Markert, L., and Greene, J. *J. Appl. Phys.* 62 **1987** 481
3. Koehler, J. *Physical Review B* 2 2 **1970** 547
4. Chu, X. and Barnett, S. *J. Appl. Phys.* 77 **1995** 4403
5. Anderson, P. and Li, C. *Nanostructured Materials* 5 3 **1995** 349

6. Lince, J. R., Hilton, M. R., and Bommannavar, A. S. *Journal of Materials Research* vol.10, no.8 **1995** 2091-2105

7. Jayaram, G., Marks, L. D., and Hilton, M. R. *Surface and Coatings Technology* 77 **1995** 393-399

8. Simmonds, M. C., Van Swygenhoven, H., Pflueger, E., Savan, A., Hauert, R., Knoblauch, L., and Mikhailov, S. *Surface and Coatings Technology* 94-95 **1997** 490-494

9. Da-YungWang, Chi-Lung Chang, Zie-Yih Chen, and Wei-Yu Ho *Surface and Coatings Technology* 120-121 **1999** 629-635

10. Savan, A, Pflueger, E, Goller, R, and Gissler, W *Surface and Coatings Technology* 126 **2000** 159-165

11. Phani, A, Krzanowski, J, and Nainaparampil, J *Mater. Res. Soc. Symposium Proceedings* 750 **2003** 291-296

12. Phani, A. R., Krzanowski, J. E., and Nainaparampil, J. J. *Surface Engineering 2002 - Synthesis, Characterization and Applications. Symposium (Mater. Res. Soc. Symposium Proceedings Vol. 750)* **2003** 291-296

13. Jiayi, Sun, Lijun, Weng, Deyang, Yu, and Qunji, Xue *Vacuum* vol.65, no.1 **2002** 51-58

14. Watanabe, S, Noshiro, J, and Miyake, S *Surface and Coatings Technology* 183 2-3 **2004** 347-351

15. Xiaoling, Zhang, Lauwerens, W., Stals, L., Jiawen, He, and Celis, J. P. *Journal of Materials Research* 16 **2001** 3567-3574

16. Spalvins, T. *ASLE Transactions* 19 4 **1976** 329-334

17. Fleischauer, P. D. *ASLE Transactions* 27 1 **1984** 82-88

18. Aubert, A., Nabot, J. Ph, Ernoult, J., and Renaux, Ph *Surface and Coatings Technology* 41 1 **1990** 127-134

19. Grosseau-Poussard, J. L., Moine, P., and Villain, J. P. *Thin Solid Films* vol.224, no.1 **1993** 52-57

20. Weise, G., Mattern, N., Hermann, H., Teresiak, A., Baecher, I., Brueckner, W., Bauer, H. D., Vinzelberg, H., Reiss, G., Kreissig, U., Maeder, M., and Markschlaeger, P. *Thin Solid Films* 298 1-2 **1997** 98-106

21. Nozhenkov, M. V., Avilov, A. S., Voronin, N. A., Semenov, A. P., and Semiletov, S. A. *Physics, Chemistry and Mechanics of Surfaces* 3 8 **1985** 2438-2450

22. Lince, J. R. and Fleischauer, P. D. *Journal of Materials Research* 2 6 **1987** 827-838

23. Spalvins, T. *Journal of Vacuum Science and Technology A* 5 2 **1987** 212-219

24. Spalvins, T. *Thin Solid Films* vol.96, no.1 **1982** 17-24

25. Spalvins, T. *Thin Solid Films* 73 **1980** 291-297

26. Nozhenkov, M. V., Voronin, N. A., Semenov, A. P., and Tovmasyan, Yu *Soviet Journal of Friction and Wear* 7 **1986** 14-18

27. Fleischauer, P. D. *Thin Solid Films* 154 1-2 **1987** 309-322

28. Moser, J. and Levy, F. *Thin Solid Films* 228 1-2 **1993** 257-260

29. Moser, J. and Levy, F. *Journal of Materials Research* 8 1 **1993** 206-213

30. Ito, T. and Nakajima, K. *Philosophical Magazine B* 37 6 **1978** 773-775

31. Reichelt, K. and Mair, G. *Journal of Applied Physics* 49 3, pt. 1 **1978** 1245-1247

32. Dimigen, H., Hubsch, H., and Willich, P. *Thin Solid Films* 64 2 **1979** 221-221

33. Christy, R. I. *Thin Solid Films* 73 2 **1980** 299-307

34. Dimigen, H., Hubsch, H., Willich, P., and Reichelt, K. *Thin Solid Films* 129 1-2 **1985** 79-91

35. Bolster, R. N., Singer, I. L., Wegand, J. C., Fayeulle, S., and Gossett, C. R. *Surface and Coatings Technology* 46 2 **1991** 207-216

36. Moser, J., Levy, F., and Bussy, F. *Journal of Vacuum Science and Technology A* 12 2 **1994** 494-500

37. Spalvins, T *ASLE Transactions* 17 4 **1974** 1-7

38. Kuwano, H. and Nagai, K. *Journal of Vacuum Science and Technology A* 3 **1985** 1809-1812

39. Moser, J. and Levy, F. *Journal of Materials Research* 7 3 **1992** 734-740

40. Bertrand, P. A. *Journal of Materials Research* 4 1 **1989** 180-184

41. Doyle, S. E., Mattern, N., Pitschke, W., Weise, G., Kraut, D., and Bauer, H. D. *Thin Solid Films* 245 **1994** 255-259

42. Gribi, P., Sun, Z. W., and Levy, F. *Journal of Physics D* 22 1 **1989** 238-240

43. Spalvins, T *ASLE Transactions* 12 1 **1969** 36-43

44. Spalvins, T *ASLE Transactions* 14 7 **1971** 267-274

45. Seitzman, L. E., Bolster, R. N., and Singer, I. L. *Thin Solid Films* 260 **1995** 143-147

46. Lauwerens, W., Jihui, Wang, Navratil, J., Wieers, E., D'haen, J., Stals, L. M., Celis, J. P., and Bruynseraede, Y. *Surface and Coatings Technology* 131 1-3 **2000** 216-221

47. Jihui, Wang, Lauwerens, W., Wieers, E., Stals, L. M., Jiawen, He, and Celis, J. P. *Surface and Coatings Technology* 139 2-3 **2001** 143-152

48. Bichsel, R., Buffat, P., and Levy, F. *Journal of Physics D* 19 8 **1986** 1575-1585

49. Buck, V. *Wear* 91 3 **1983** 281-288

50. Xiaoling, Zhang, Lauwerens, W., Jiawen, He, and Celis, J. P. *Journal of Vacuum Science and Technology A* 21 2 **2003** 416-421

51. Xiaoling, Zhang, Prakash, B., Lauwerens, W., Xiaodong, Zhu, Jiawen, He, and Celis, J. P. *Tribology Letters* 14 **2003** 131-135

52. Lince, J. and Fleischauer, P. *Journal of Vacuum Science and Technology A* 5 4, pt. 2 **1987** 1312-1313

53. Lince, J., Stewart, T., Hills, M., Fleischauer, P., Yarmoff, J., and Taleb-Ibrahimi, A. *Surface Science* 210 3 **1989** 387-405

54. Williams, R. H. and McGovern, I. T. *Japanese Journal of Applied Physics* suppl.2 2 **1974** 413-416

55. Baker, M. A., Gilmore, R., Lenardi, C., and Gissler, W. *Applied Surface Science* 150 1-4 **1999** 255-262

56. Feng, H and Chen, J *Journal of Physics C* 7 **1974** L75-L78

57. Xushou, Zhang, Pingyu, Zhang, Huiwen, Liu, Wei, Zhao, and Shiru, Xu *Thin Solid Films* 229 1 **1993** 58-62

58. Sun, Z. W., Gribi, P., and Levy, F. *Journal of Physics D* 22 8 **1989** 1210-1216

59. Kaye, S. P., Kheyrandish, H., Colligon, J. S., and Roberts, E. W. *Thin Solid Films* 228 1-2 **1993** 252-256

60. Moser, J., Liao, H., and Levy, F. *Journal of Physics D* vol.23, no.5 **1990** 624-626

61. Shimada, H *Ctalysis Today* 86 **2003** 17-29

62. Seitzman, L. E., Singer, I. L., Bolster, R. N., and Gossett, C. R. *Surface and Coatings Technology* 51 **1992** 232-236

63. Buck, V. *Thin Solid Films* 139 2 **1986** 157-168

64. Tavares, C. J., Rebouta, L., Ribeiro, E., Pacaud, J., and Denanot, M. F. *Surface and Coatings Technology* 174-175 **2003** 273-280

65. Jakovidis, G., Jamieson, I. M., and Singh, A. *Surface Review and Letters* 10 2-3 **2003** 443-448

Section 9. Deposition, structural and tribological characterization of co-deposited TiN+MoS_x coatings

9.1. Introduction

The idea of including lubricant into the structure of a hard, wear resistant coating is not completely new. Small oil droplets were included in an electrochemically deposited Ni-P matrix in 1985 [1]. A decade later Bae et al. reported a successful attempt to include MoS_2 into the structure of TiN by thermal CVD at 800 °C [2]. The authors report hexagonal 2H MoS_2 clusters with their (002) planes parallel to the substrate surface and embedded in fcc TiN hard matrix. The friction coefficient of this coating was 0.2 against 440C type stainless steel and was twofold lower than the friction coefficient of their TiN benchmark coatings measured in the same conditions. This work was the first report on a combination of MoS_2 and a hard phase by means of co-deposition. A very similar study was reported by the same authors [3] where they mention friction coefficients of about 0.07 to 0.3 against Si_3N_4 ball. In a third publication on the topic from the same group, the authors varied the TiN/MoS_2 ratio and reported that with increasing MoS_2 content the phase composition of the coatings changes from fcc TiN through fcc TiN + 2H MoS_2 to 2H MoS_2 [4]. The same results were published also elsewhere [5]. The first self-lubricating hard coatings deposited by PVD were the TiB_2-MoS_2 coatings reported by Gilmore et al. [6]. The authors used magnetron sputtering from a composite target consisting of two halves for the deposition of the coatings. One half was made of TiB_2 and the other half was made of MoS_2. Even at small MoS_2 contents a significant reduction of the friction coefficient of the TiB_2-MoS_2 coatings against a steel ball was observed compared to the relatively high friction coefficient for pure TiB_2 benchmark coating. No simultaneous existence of TiB_2 and 2H MoS_2 phases was reported. Later the same group reported similar results using the same approach for the deposition of TiN+MoS_2 self-lubricating hard coatings [7]. They obtained coatings in which no simultaneous existence of fcc TiN and 2H MoS_2 could be detected. With increasing MoS_2 content the structure of the coatings changed from fcc TiN through quasiamorphous to 2H MoS_2. It is supposed by the authors that Mo and S atoms dissolve in the fcc TiN matrix at low MoS_2 content. The friction coefficient against a steel ball was close to 0.1 for the coatings deposited at -100 V substrate bias. Goller et al. [8] used cathodic arc evaporation as a source of TiN and magnetron sputtering as a source of MoS_2 to deposit TiN+MoS_2 coatings containing 8 mol% MoS_2 with friction coefficient of 0.1-0.2 against Al_2O_3 ball. The coatings obtained had typical fcc TiN structure that supports the assumption that the Mo and S atoms are dissolved in the fcc TiN matrix thus yielding a metastable solid solution. Heinisch et al. doped (Ti,Al)N with MoS_2 to obtain amorphous coatings [9]. Unfortunately no friction and wear results were reported for these coatings. Electron evaporation of Ti and magnetron sputtering of MoS_2 were used by Cosemans et al. to deposit TiN+MoS_2 coatings with gradient of the MoS_2 concentration over its thickness. The friction coefficient of this coating against Al_20_3 was reported to be 0.4 while the friction coefficient of pure TiN deposited in the same conditions was reported to be approximately 0.9. Spassov et al. deposited a (Ti,Al)(C,N)+MoS_2 coating by means of magnetron sputtering of TiAl, C and MoS_2 target in Ar+N_2 reactive gas [10]. Friction coefficients of 0.09 and 0.8 against 100Cr6 ball bearing steel were reported for the (Ti,Al)(C,N)+MoS_2 and pure (Ti,Al)(C,N) coatings, respectively. The (Ti,Al)(C,N)+MoS_2 coating consisted of nanocrystalline fcc (Ti,Al)(C,N)-based phase embedded in amorphous matrix as demonstrated by TEM imaging and SAED. Audronis et al. studied CrB_2+MoS_2 coatings deposited by magnetron sputtering of targets consisting of mixture of Cr, B and MoS_2 [11]. The friction coefficients of the resulting coatings against chromium steel ball were measured with a scratch-tester and varied in the range 0.14-0.19. No co-existing of the MoS_2 with the CrB_2 phase was observed. Efeoglu et al. have deposited a (Ti,B)(C,N)+MoS_2 coating with friction coefficient against WC-6%Co ball in the range of 0.04. Crystalline TiB_2, TiC and 2H MoS_2 phases were reported to co-exist in this coating. Haider et al. used magnetron sputtering from Ti and MoS_2 targets in Ar+N_2 reactive atmosphere in order to deposit TiN+MoS_2 coatings [12]. By varying the power supplied to the MoS_2 target the authors varied the MoS_2 content in the coatings. All coatings consisted of nanocrystalline fcc TiN and the size of the crystallites decreased with the MoS_2 content increasing. The friction coefficient of the coatings against WC-Co hardmetal ball was about 0.35 while the friction coefficient of a pure TiN coating deposited at the same conditions was 0.80. Rahman et al. deposited TiN+7wt%MoS_2 coatings by means of magnetron sputtering from a Ti and a MoS_2 target in Ar+N_2 reactive atmosphere [13]. The coatings had a fcc TiN structure and friction coefficient against WC ball of 0.4-0.5. The friction coefficient of a pure TiN coating deposited in the same conditions was reported to be 0.8. Ding et al [14] reported a (Ti,Si)N+MoS_2 coatings deposited by magnetron sputtering from a Ti, Si and MoS_2 targets in Ar+N_2 reactive atmosphere with Mo content from 0 mol.% to 13.5 mol.%. The coatings had fcc TiN structure and exhibited friction coefficient of 0.4-0.5 against Al_2O_3 ball. A summary of the main results reported in the studies mentioned so far is given in Table 9.1.

Reference	**System**	**Deposition method**	**MoS_2 content**	**Phase composition**	**Friction coefficient**	**Friction counterpart**	**Wear rate, $mm^3/(Nm)$**
[2]	$TiN+MoS_2$	Thermal CVD	54-80 mol%	mixed fcc TiN + 2H MoS_2	0.20	440C steel ball	n/a
[3]	$TiN+MoS_2$	Thermal CVD	Varied but no values given	mixed fcc TiN + 2H MoS_2 at high MoS_2 content and single-phase fcc TiN at lower MoS_2 content	0.07-0.30 depending on the MoS_2 content	Si_3N_4 ball	n/a
[5]	$TiN+MoS_2$	Thermal CVD	Varied but no values given	mixed fcc TiN + 2H MoS_2 at high MoS_2 content and single-phase fcc TiN at lower MoS_2 content	0.07-0.30 depending on the MoS_2 content	Si_3N_4 ball	n/a
[6]	TiB_2+MoS_2	Magnetron sputtering from a composite TiB_2+MoS_2 target	11-62 mol%	nanocrystalline hexagonal TiB_2 at low MoS_2 content and quasiamorphous at high MoS_2 content	0.09-0.60 depending on the MoS_2 content	steel ball	n/a
[7]	$TiN+MoS_2$	Magnetron sputtering from a composite $TiN+MoS_2$ target	20-66 mol%	nanocrystalline fcc TiN	0.1-0.2 depending on the Mos_2 content	steel ball	n/a

Reference	**System**	**Deposition method**	**MoS_2 content**	**Phase composition**	**Friction coefficient**	**Friction counterpart**	**Wear rate, $mm^3/(Nm)$**
[8]	$TiN+MoS_2$	PVD, cathodic arc evaporation of Ti and magnetron sputtering of MoS_2 in $Ar+N_2$ reactive atmosphere	8 mol%	fcc TiN	0.1-0.2	Al_2O_3 ball	
[9]	$(Ti,Al)N+MoS_2$	Magnetron sputtering of TiAl and MoS_2 targets in $Ar+N_2$ reactive atmosphere	16mol%	amorphous	n/a	n/a	n/a
[15]	$TiN+MoS_2$	Electron beam evaporation of Ti and magnetron sputtering of MoS_2 in $Ar+N_2$ reactive atmosphere	8 wt%	fcc TiN	0.4	Al_2O_3 ball	$1.5.10^{-6}$
[10]	(Ti,Al)(C,N)	Magnetron sputtering of TiAl, C and MoS_2 in $Ar+N_2$ reactive atmosphere	30 vol%	fcc TiN in amorphous matrix	0.09	100Cr6 ball	
[11]	CrB_2+MoS_2	Magnetron sputtering from lose mixtures of Cr, B and MoS_2 powders	15-27 mol%	nanocrystalline CrB_2-type structure	0.14-0.19	Cr-steel ball	n/a

Reference	**System**	**Deposition method**	**MoS_2 content**	**Phase composition**	**Friction coefficient**	**Friction counterpart**	**Wear rate, $mm^3/(Nm)$**
[16]	$Ti(B,C)_2$+MoS_2	Magnetron sputtering from TiB_2, Ti, C and MoS_2 targets	n/a	nanocrystalline hexagonal TiB_2, fcc TiC and 2H MoS_2	0.04-0.09 depending on the normal force	WC-6%Co ball	n/a
[12]	TiN+MoS_2	Magnetron sputtering of Ti and MoS_2 targets in Ar+N_2 reactive atmosphere	3-11 wt%	fcc TiN at lower MoS_2 content and amorphous at higher MoS_2 content	0.35	WC ball	$6.0.10^{-7}$
[13]	TiN+MoS_2	Magnetron sputtering of Ti and MoS_2 targets in Ar+N_2 reactive atmosphere	7 wt%	fcc TiN	0.40-0.50	WC ball	n/a
[14]	(Ti,Si)N+MoS_2	Magnetron sputtering of Ti, Si and MoS_2 targets in Ar+N_2 reactive atmosphere	0-13.5 mol%	fcc TiN	0.40-0.50	Al_2O_3 ball	$5.0.10^{-7}$- $2.0.10^{-6}$

Table 9.1. Summary of the found published effort devoted on co-deposited hard phase + MoS_x coatings

From these results it is obvious that addition of MoS_2 to a hard phase leads to markedly lower friction coefficient and (where reported) wear coefficient of the resulting coatings compared to the “pure” hard phase coating. However, the following questions still remain unanswered:

- How does the structure of a hard phase coating change with the addition of increasing amount of MoS_2 added to it?
- What is the state of the MoS_2 in case no 2H MoS_2 is detected as a separate phase in the resulting coatings?

Systematic variation of the MoS_2 content while keeping all other deposition parameters constant, combined with TEM study of the structure of the resulting coatings, is the approach adopted in the current work for answering the above questions. As mentioned in Section 1, TiN was chosen as a hard phase.

9.2. Experimental details

The coatings were deposited in the PVD system described in Section 3. Co-deposition from two sources, as shown on Figure 2.2a, has the following serious disadvantages:

- Lateral variation of the chemical composition
- Too low deposition rates due to too great a substrate-to-target distance

To avoid these unwanted effects, deposition from a mixed target was chosen as shown on Figure 2.2b. To obtain TiN+MoS_2 coatings, sputtering of Ti and MoS_2 in a reactive atmosphere of Ar+N_2 can be used. However, this requires a good control of the N_2 flow rate which was not feasible with the deposition system available. As mentioned in Section 7, TiN coatings can also be obtained by sputtering of a TiN target in Ar atmosphere. Therefore, non-reactive sputtering was selected as a source of TiN also for the co-deposition of the TiN+MoS_2 coatings. The mixed target had a cake-like design consisting of 24 exchangeable segments as shown on Figure 9.1. The MoS_2 content of the coating can be varied by varying the number of MoS_2 segments in the target. The segments were arranged in the desired configuration and bonded to a copper plate by soldering with indium. Care was always taken to distribute all segment uniformly across the target in order to avoid lateral variation of the chemical composition of the coatings.

The deposition rates of TiN and MoS_x deposited in the same conditions by sputtering of TiN and MoS_2 targets were measured to be 6.05 nm/min and 18.36 nm/min, respectively. The

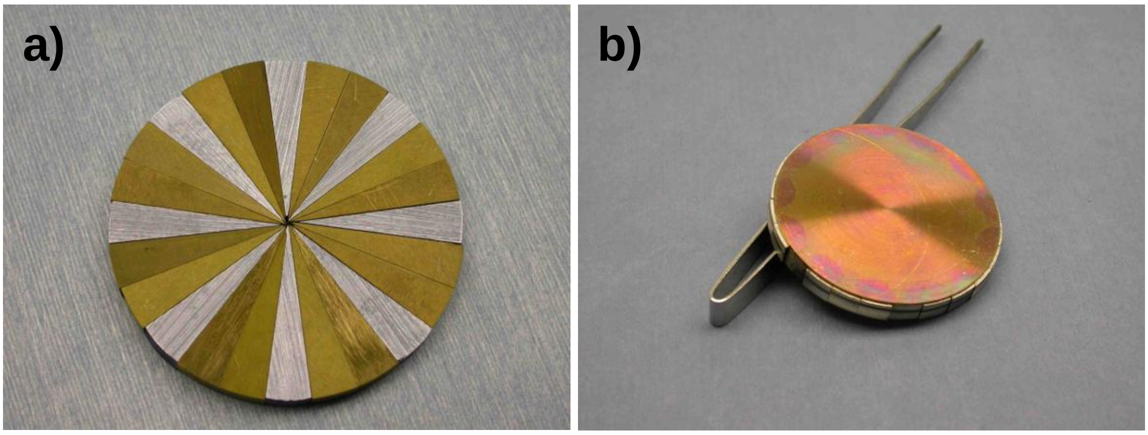

Fig. 9.1. a) TiN-MoS_2 segmented target. The orange segments are TiN and the grey ones are MoS_2; b) the target bonded to a Cu backing plate

Coating No.	MoS_2 segments	Mo, at. %	S, at. %	(TiN_y), mol. %	MoS_x, mol.%
C1	2	14	20	66	17.5
C2	3	17	34	49	25.8
C3	4	25	38	37	40.3
C4	5	25	46	29	46.3
C5	6	30	48	23	56.6
C6	8	28	54	18	60.9

Table 9.2. Coating labeling, target composition and coating chemical composition.

MoS_x content in the coatings was chosen to vary from the possible minimum to about 50 vol%. For assembling of a symmetrical target, a minimum of 2 MoS_2 segments can be used and in order to achieve about 50 vol.% MoS_2 in the coating, 8 MoS_2 segments should be used in the target. Therefore, depositions from targets with 2, 3, 4, 5, 6 and 8 MoS_2 segments were made and the resulting coatings were labeled C1, C2, C3, C4, C5 and C6, respectively. A layer of Ti with thickness of approx. 170 nm was deposited under each coating in order to improve the adhesion to the substrate so the coating architecture is as shown on Figure 9.2. The coating labeling, target composition and chemical composition as measured by EDX are shown on Table 9.2. The coatings were deposited on the substrates defined in Section 6. The deposition conditions were exactly the same as for the TiN benchmark coating deposited at 280 °C. The coatings structure and chemical composition were studied with TEM and EDX, respectively, as described in Section 4. The tribological and mechanical properties of the coatings were investigated with the methods described in Section 5.

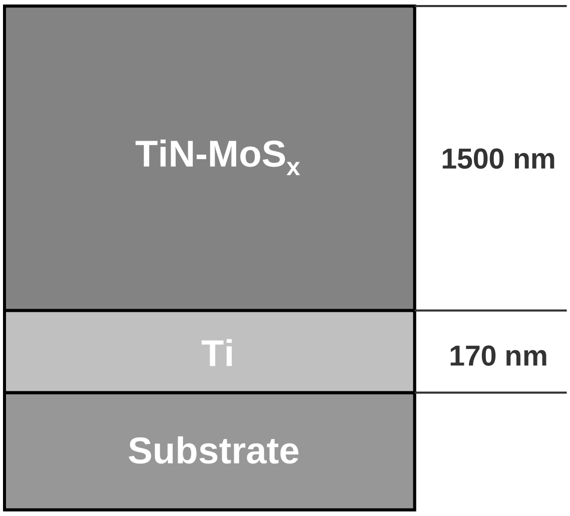

Fig. 9.2. Architecture of coatings C1-C6

9.3. Results: structure

9.3.1. Coating C1

The structure of the coatings is summarized on Figure 9.3. It is a typical columnar structure of type Zone T as defined by the model of Thornton [17]. The coating is monophase and consists of fcc TiN crystals as seen from the SAED pattern. No amorphous phase was identified in the coating. Local epitaxy of this solid solution from the Ti adhesion layer is observed, as seen from the bright field images and especially from the dark field image where columns starting from the Si(100) substrate and growing through the whole coating thickness are observed.

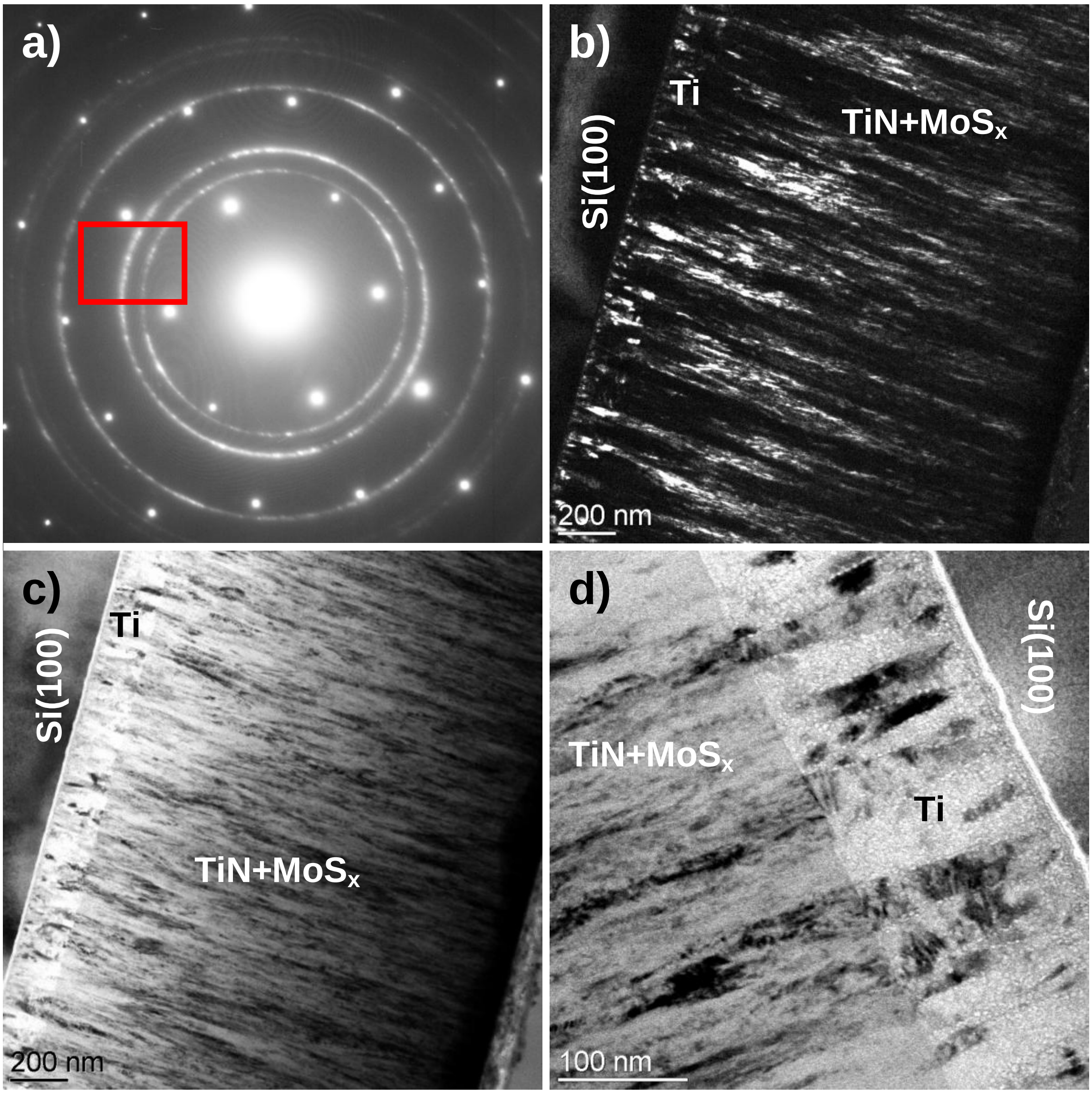

Fig. 9.3. TEM study of the structure of coating C1: a) SAED pattern. The red rectangle shows the part of the rings from which the dark field image was taken; b) dark field image; c), d) bright field images

9.3.2. Coating C2

The structure of coating C2 is shown on Figure 9.4. The columns are shorter and less well defined than these of coating C1. The crystalline phase was identified as fcc TiN. Some amorphous phase also exists as seen from the SAED pattern and the dark field image. It is difficult to determine whether local epitaxy with the Ti adhesion layer takes place in the case of coating C2.

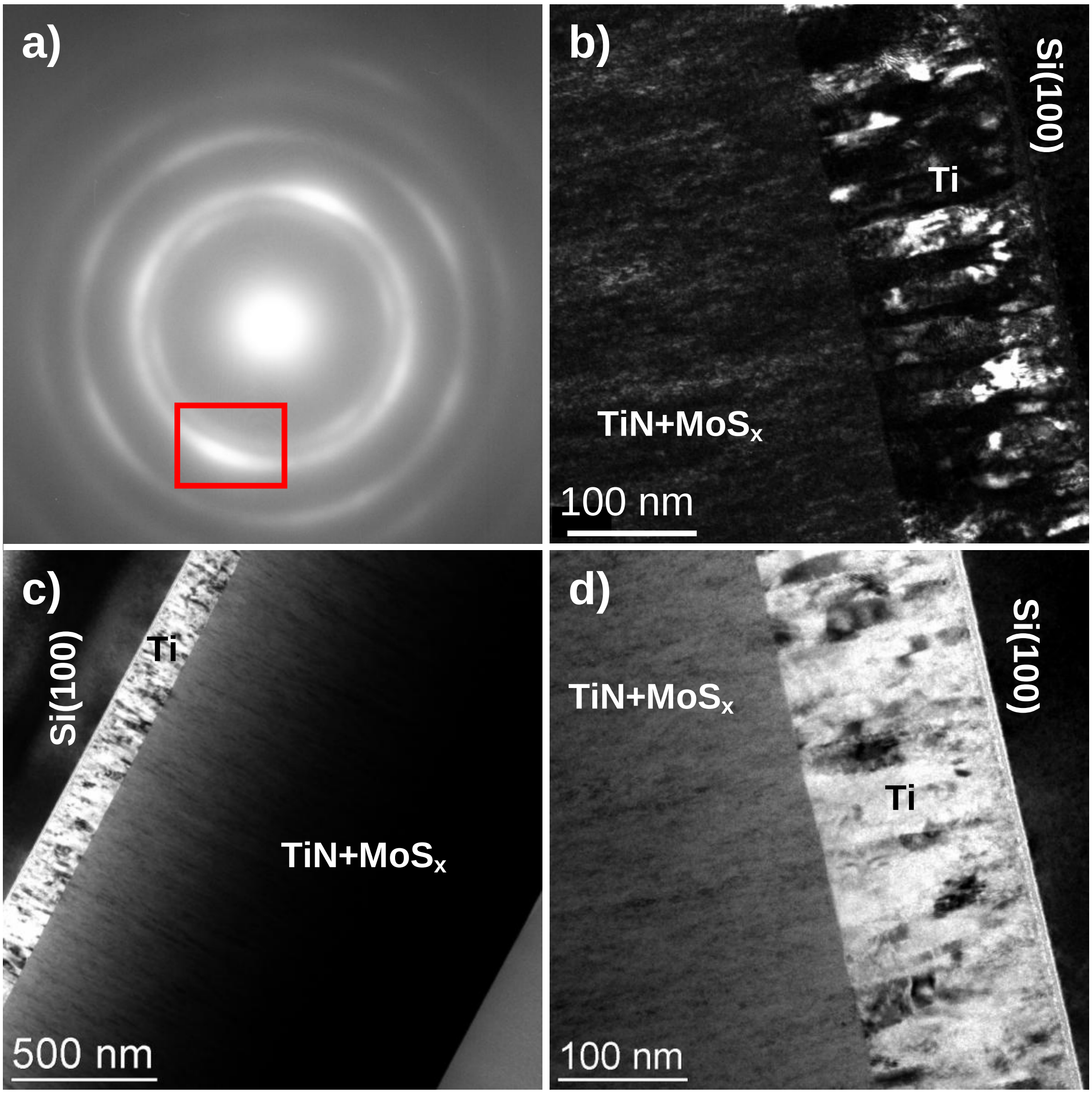

Fig. 9.4. TEM study of the structure of coating C2: a) SAED pattern. The red rectangle shows the part of the rings from which the dark field image was taken; b) dark field image; c), d) bright field images

9.3.3. Coating C3

The structure of this coating is summarized on Figure 9.5. As seen from the figure, the coating consists of isometric crystals with size of approx. 7 nm. These crystals are fcc TiN, as determined from the SAED pattern, and are embedded in amorphous matrix. Similarly to the case of coating C2, it is difficult to determine whether local epitaxy with the Ti adhesion layer exists.

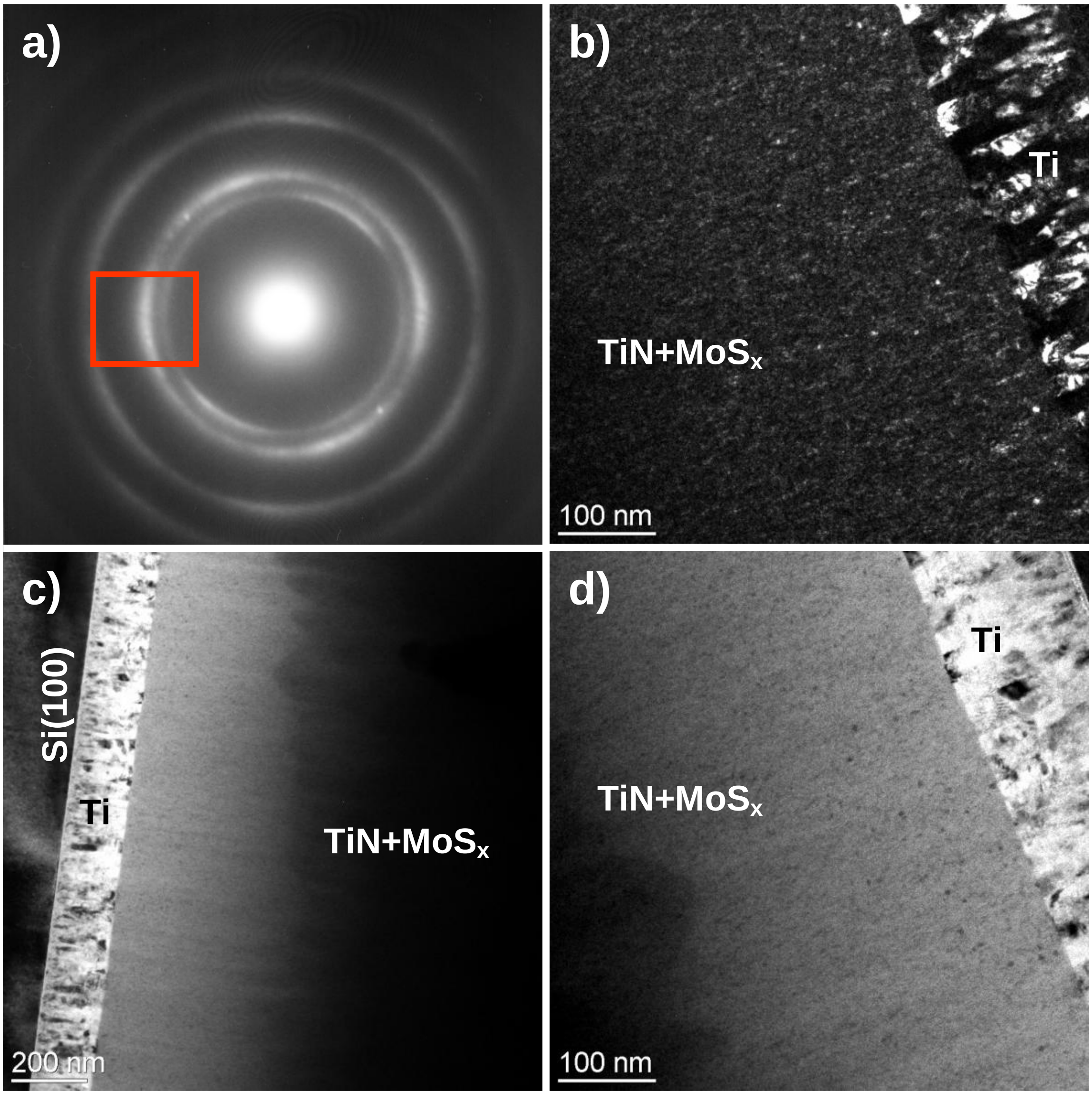

Fig. 9.5. TEM study of the structure of coating C3: a) SAED pattern. The red rectangle shows the part of the rings from which the dark field image was taken; b) dark field image; c), d) bright field images

9.3.4. Coating C4

The structure of this coating is represented on Figure 9.6. In this case, for TEM study a coating with a thinner Ti adhesion layer and a smaller overall thickness compared to the other coatings was deposited in the same conditions as the functional coating C4. The functional C4 coating has the same architecture and thickness as the other coatings described in this chapter. It is seen from the SAED pattern that the coating consists of fcc TiN crystals. Their size is extremely small, typically 4-5 nm and they are embedded in an amorphous matrix.

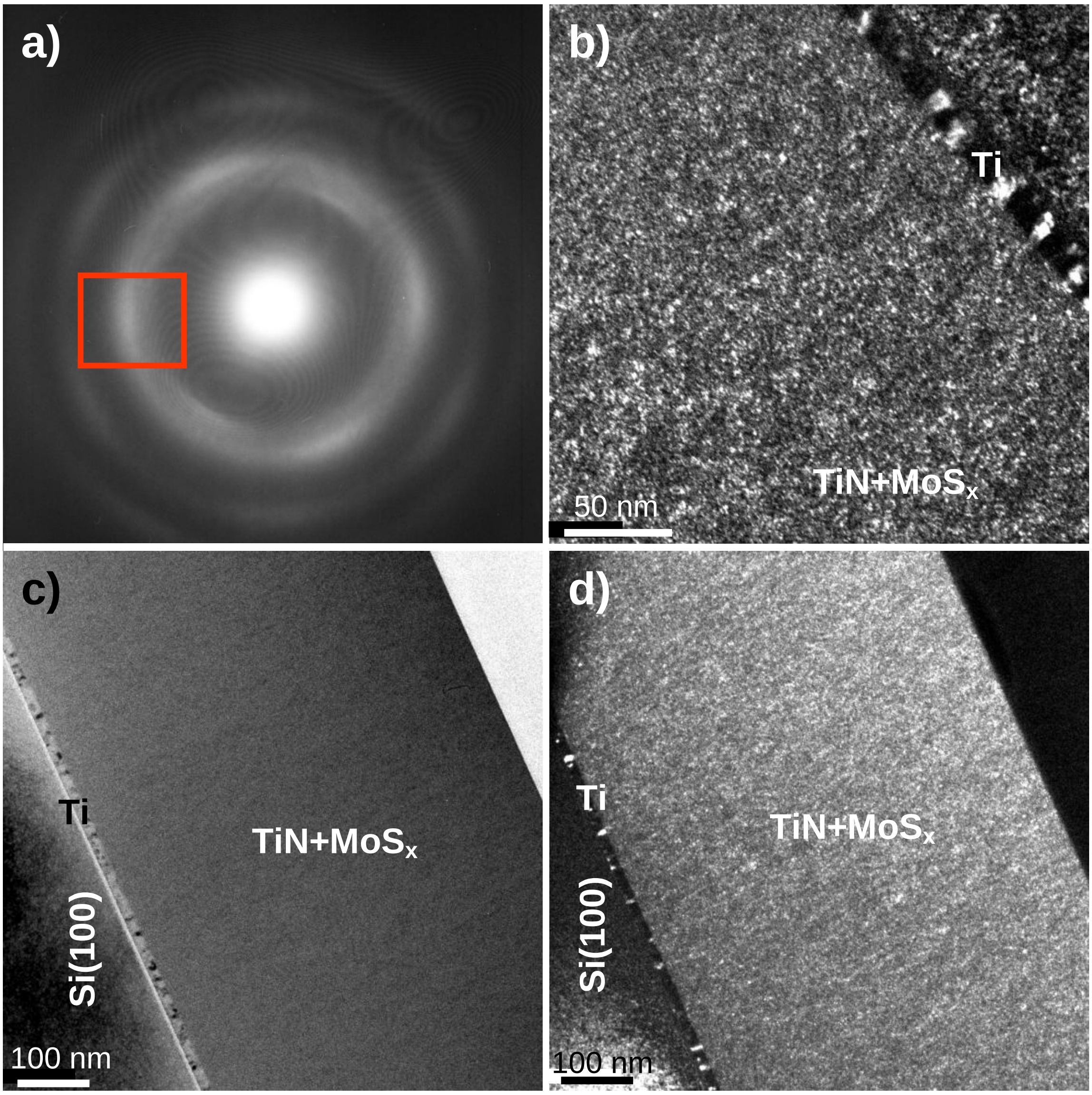

Fig. 9.6. TEM study of the structure of coating C4: a) SAED pattern. The red rectangle shows the part of the rings from which the dark field image was taken; b) dark field image; c), d) bright field images

9.3.5. Coating C5

The structure of this coating is shown on Figure 9.7. Similarly to coating C4, it consists of very small fcc TiN crystals embedded in an amorphous matrix. The size of the crystals is approximately 3 nm and the amount of the amorphous phase is greater compared to the case of coating C4.

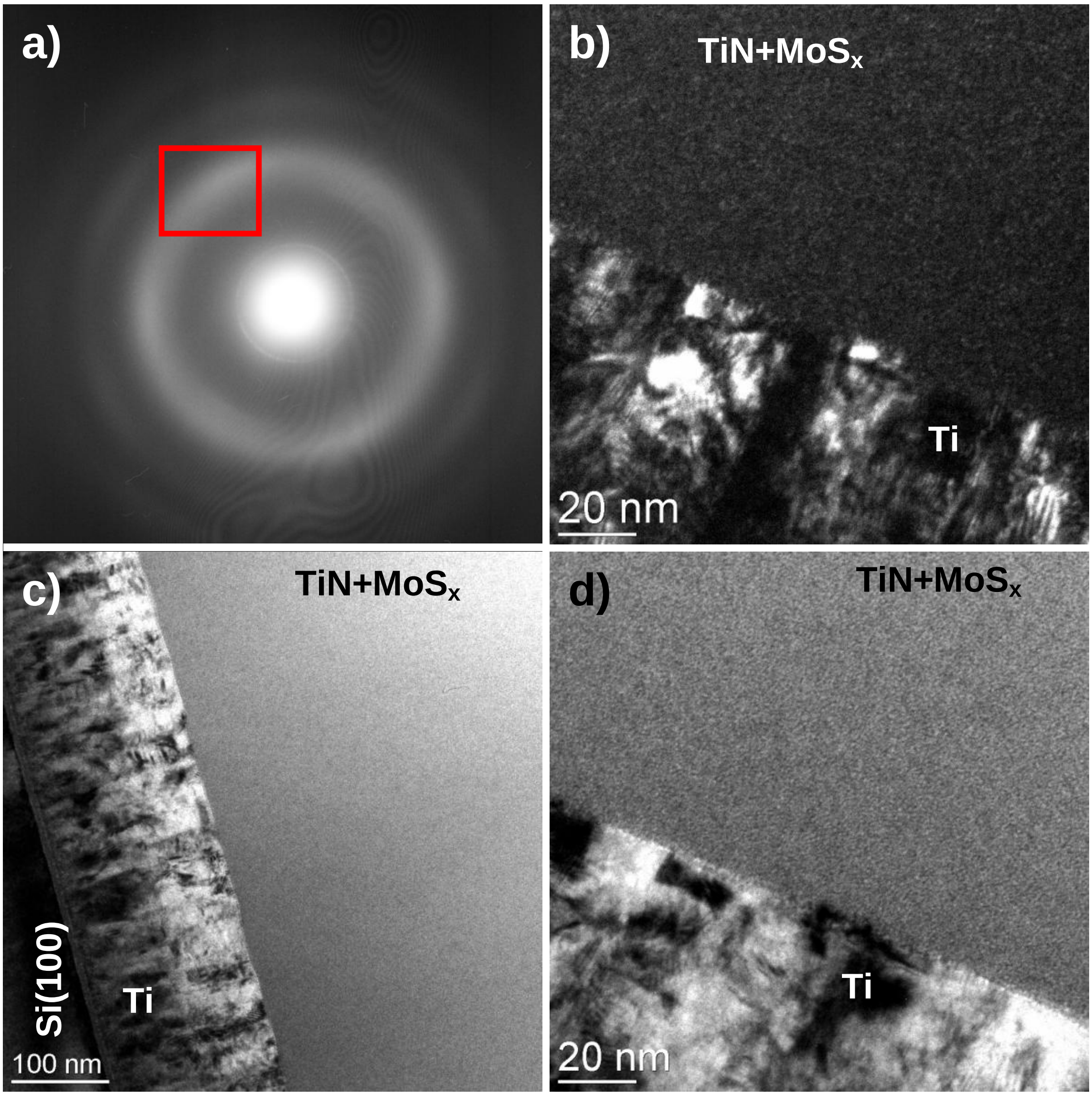

Fig. 9.7. TEM study of the structure of coating C5: a) SAED pattern. The red rectangle shows the part of the rings from which the dark field image was taken; b) dark field image; c), d) bright field images

9.3.6. Coating C6

The structure of this coating is shown on Figure 9.8. The same conclusions can be made for this coating as for coating C5. However, more amorphous phase presents in coating C6 compared to coating C5.

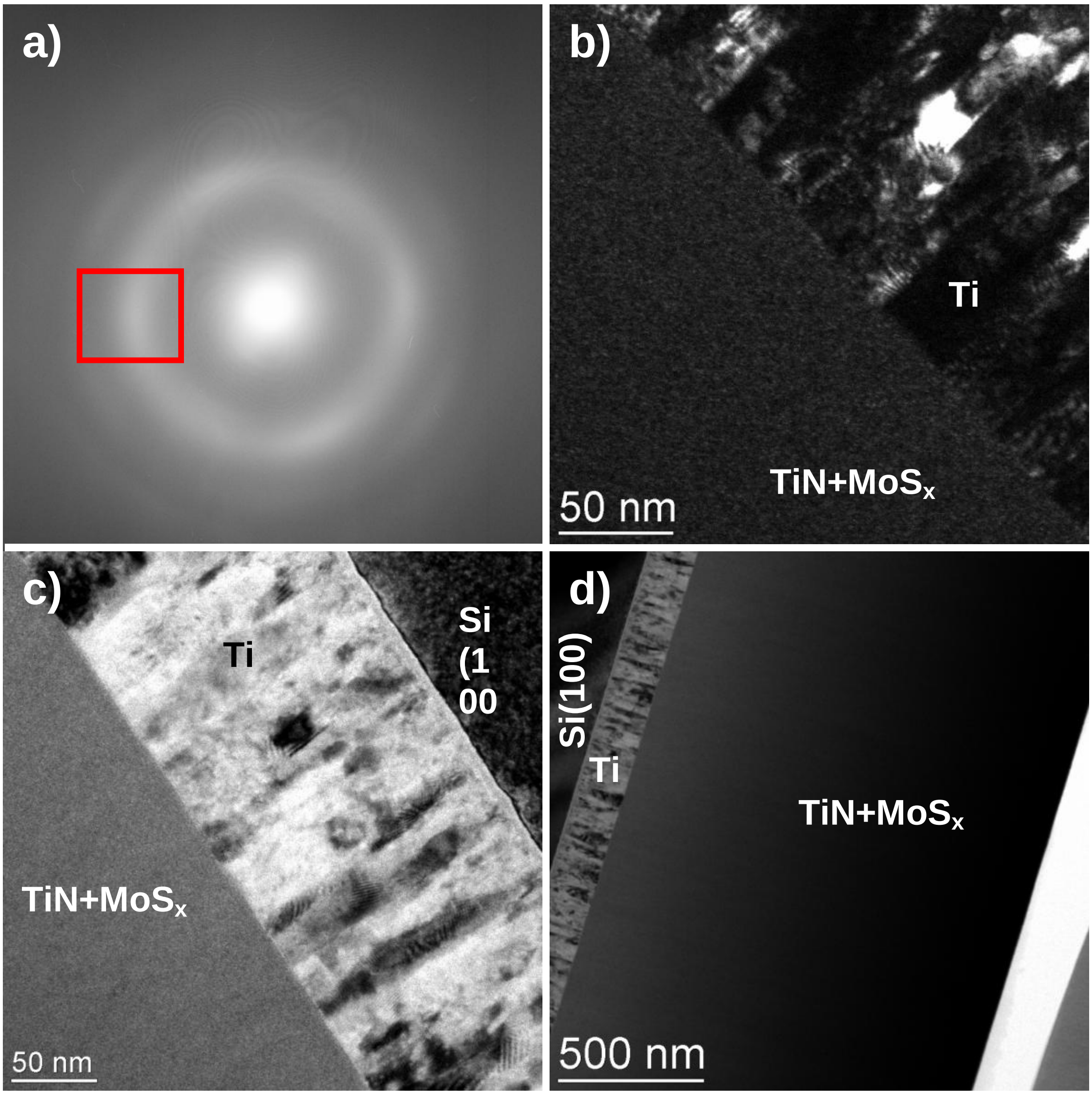

Fig. 9.8. TEM study of the structure of coating C6: a) SAED pattern. The red rectangle shows the part of the rings from which the dark field image was taken; b) dark field image; c), d) bright field images

9.4. Results: mechanical and tribological properties of the coatings

The hardness of coatings C1 - C6 is compared on Figure 9.9. For comparison, the hardness of the TiN and MoS$_x$-Ti benchmark coatings is also shown on the figure. It is seen that there is practically no decrease in hardness when small amount of MoS$_x$ is added to TiN,

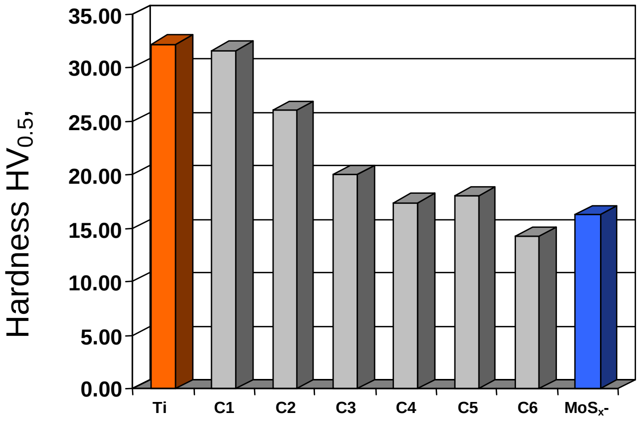

Fig. 9.9. The hardness of coatings C1 – C6 compared to these of the TiN and MoS_x-Ti benchmarks

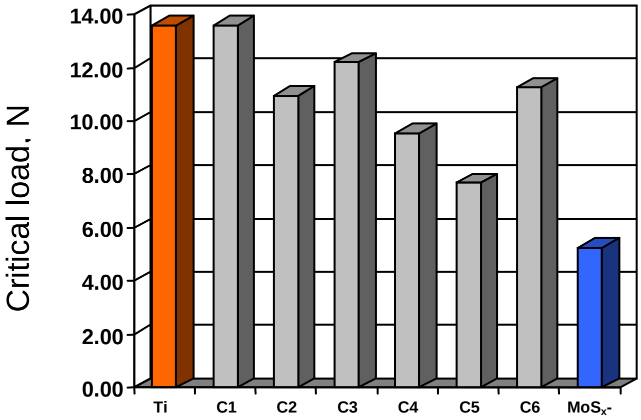

Fig. 9.10. The crytical loads of coatings C1 – C6 compared to these of the TiN and MoS_x-Ti benchmarks

as it is the case for coating C1. With the amount of MoS_x in the coating increases, the hardness decreases almost monotonically.

The crytical loads of the coatings are summarized on Figure 9.10. In all cases a cohesive spallation was the coating failure event, as shown on Figure 9.11. The critical load tends to decrease with increasing MoS_x content of the coating. Some deviation from this rule is observed, however.

The friction curves of coatings C1 – C5 and the benchmark coatings are summarized on Figure 9.12. It is apparent from that figure that all coatings exhibit friction coefficients approximately an order of magnitude lower than that of the TiN benchmark and comparable to that of the MoS_x-Ti benchmark. This result is of critical importance for this work and proves that the co-deposited coatings have self-lubricating properties. The stable friction coefficients of all coatings studied are summarized on Figure 9.13. The stable friction coefficients were calculated as an average of all measured values over which the variation is less than 20 %.

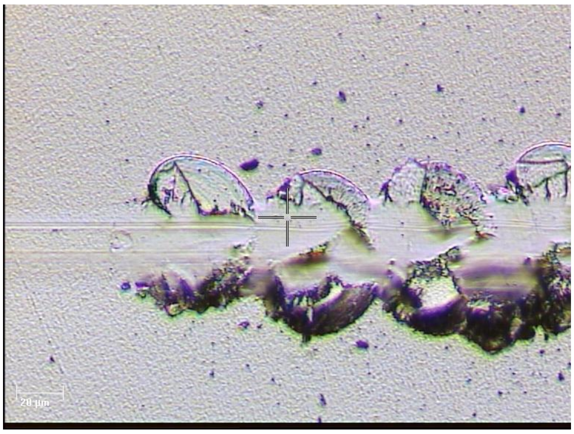

Fig. 9.11. The cohesive failure observed in coatings C1 – C6 and the TiN and MoS_x-Ti benchmarks

The wear coefficients of the coatings studied are summarized on Figure 9.14. The values of the wear coefficients of the co-deposited coatings are much lower (up to an order of magnitude for the case of coating C1) than that of the TiN benchmark coating which is another proof of concept for this work.

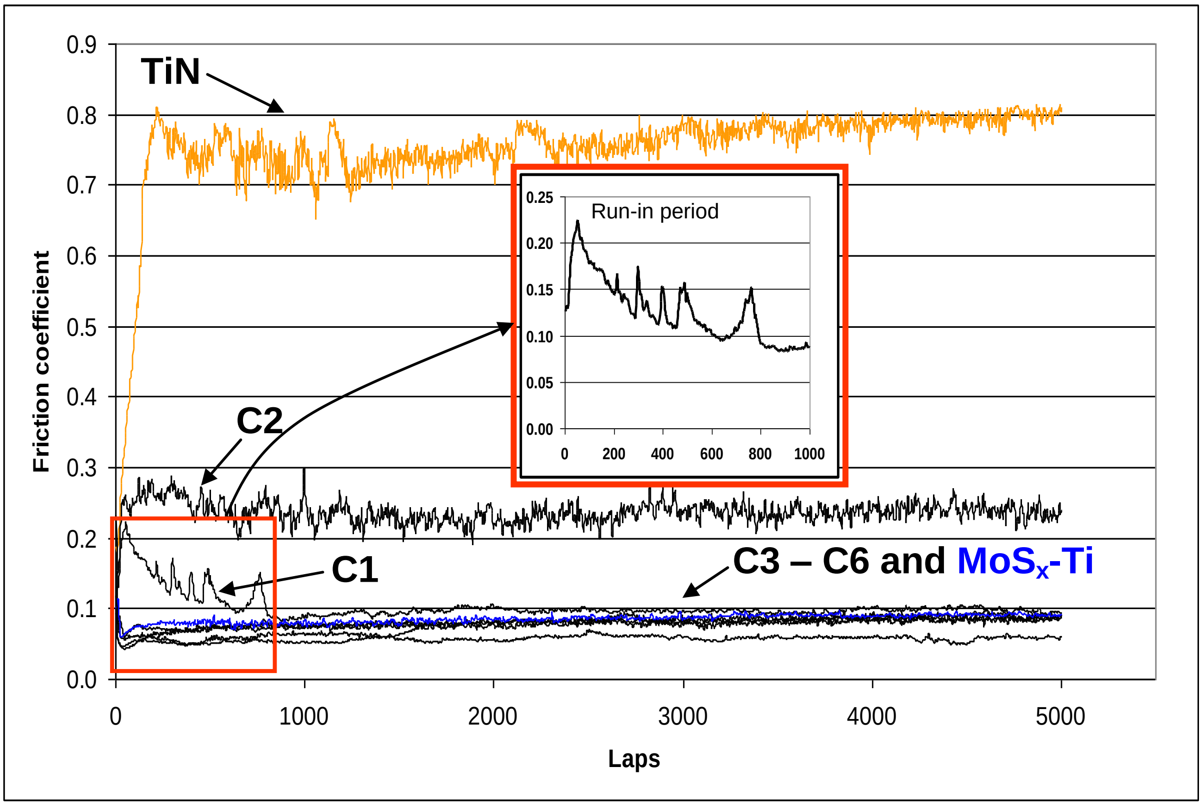

Fig. 9.12. The friction curves of coatings C1 – C6 compared to these of the TiN and MoS_x*-Ti benchmarks. The latter is shown in blue. Note the run-in period observed in coating C1 as shown in the insert*

9.5. Discussion

There is an obvious trend for decreasing the crystalline size of the fcc TiN with increasing amount of the MoS_x present in coatings C1 – C6. Coating C1 has a monophase crystalline structure but contains a significant amount of MoS_x (17.5 mol.%). No amorphous phase (if any) that corresponds to this MoS_x content was identified in the coating. This strongly supports the assumption that the Mo and S atoms are dissolved in the TiN lattice to yield a (Ti, Mo)(N,S) metastable solid solution. The existence of fcc TiN even of large concentration of both Ti and N sub-lattice vacancies is a good basis for incorporation of foreign atoms in its structure. It can be concluded that at least 17.5 mol.% of MoS_x can be dissolved in the fcc TiN lattice at the conditions used for the deposition of coating C1. Monophase crystalline co-deposited coatings at low MoS_x content have been reported by some authors, as seen from Table 9.1. The question whether amorphous phase presents or not along with the crystalline phase, however, was not clarified by the authors. It is clear from the TEM study of coating C1 that amorphous phase does not present at the given MoS_x content and deposition conditions. With increasing MoS_x content, however, the columnar structure begins to break and the size of the fcc (Ti, Mo)(N,S) crystals decreases. Amorphous phase appears and its concentration increases with increasing MoS_x content. Such amorphization with increasing MoSx content has also been reported by some authors listed in Table 9.1 however no information was provided about the presence or not of crystalline phase along with the amorphous phase. Obviously, at MoS_x content between 17.5 and 25.8 mol.% saturation of the (Ti, Mo)(N, S) solid solution in MoS_x takes place and the excess of MoS_x is present as an amorphous phase. It is difficult to figure out whether the amorphous phase contains Ti and N or it is pure MoS_x and all Ti and N present in the fcc (Ti,Mo)(N,S) phase. As seen from Section 8, pure MoS_x deposited at similar conditions has crystalline 2H structure. It is therefore logical to expect that if the MoS_x phase in coatings C2-C6 is pure, it would not be amorphous. Another argument that supports the assumption of the presence of Ti and N atoms in the MoS_x amorphous phase is the fact that MoS_x-Ti co-deposited coatings tend to be amorphous [18]. Doping WS_x, which is very similar to MoS_x, with N has also been reported to yield amorphous coatings [19], [20], [21]. Therefore it can be concluded that it is very likely to expect presence of Ti and N in the amorphous phase of coatings C2-C6. The reduction of the crystalline size of the fcc crystals with the MoSx content increasing (i.e. with the amount of the amorphous phase also increasing) can be

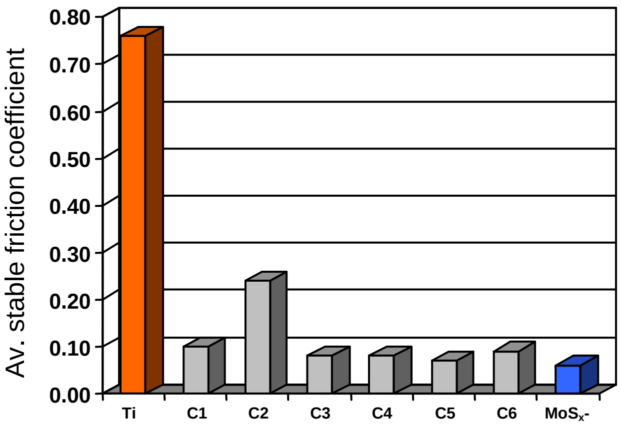

Fig. 9.13. The average stable friction coefficients of coatings C1 – C6 compared to these of the TiN and MoS_x-Ti benchmarks

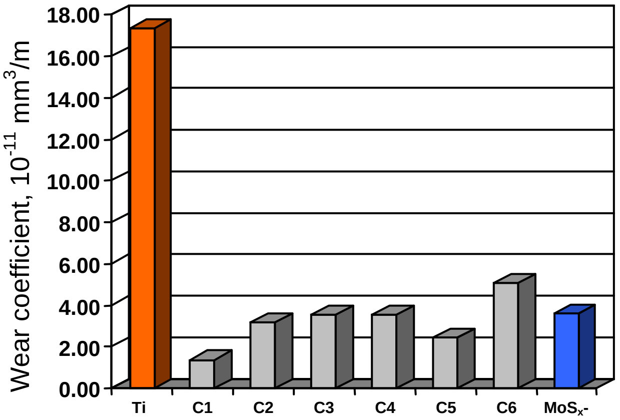

Fig. 9.14. The wear coefficients of coatings C1 – C6 compared to these of the TiN and MoS_x-Ti benchmarks

explained with hindering the crystal growth of the crystalline nuclei by the amorphous phase around them. The structures of coatings C1 – C6 are summarized on Figure 9.15.

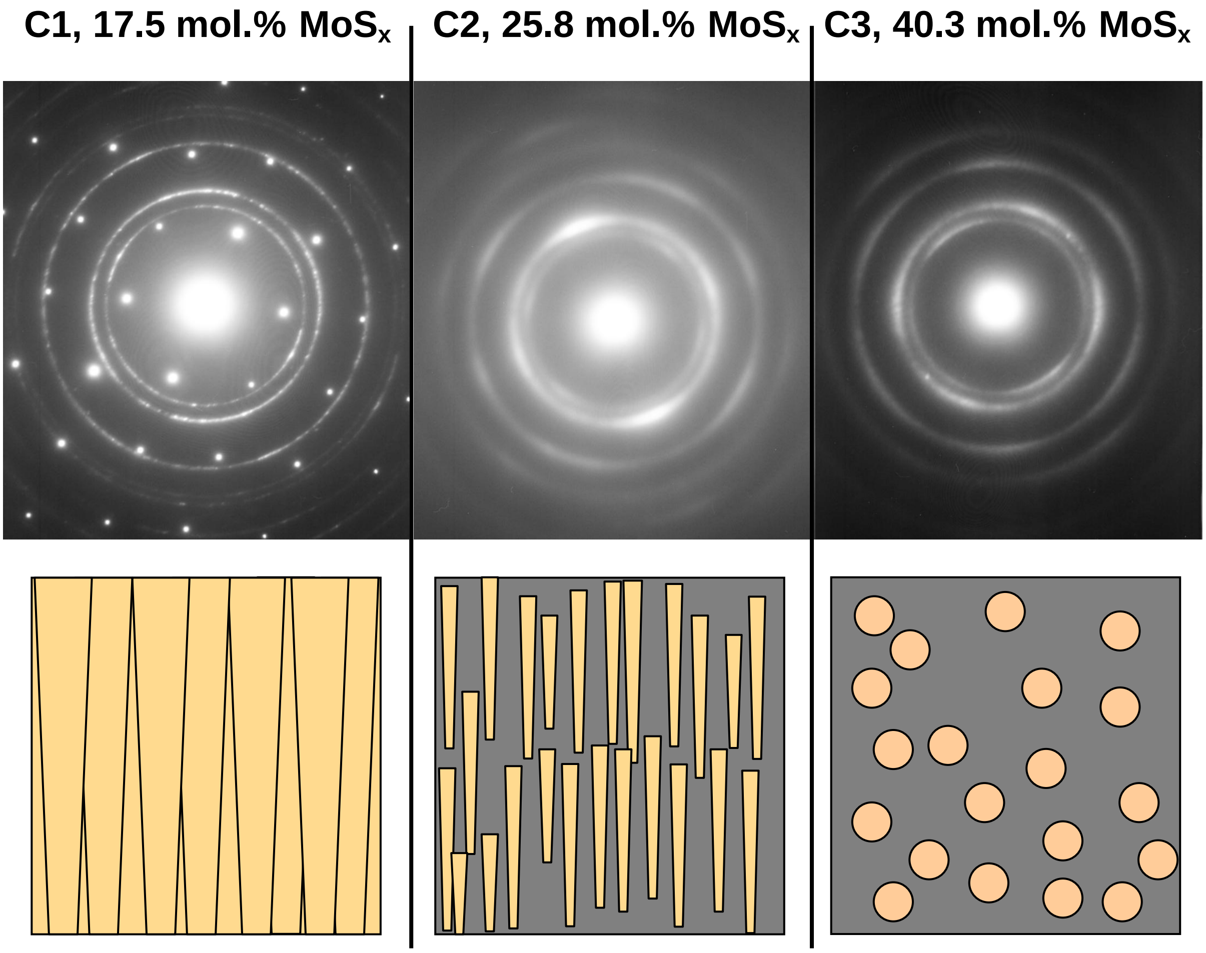

Fig. 9.15. Chematical summary of the structure of coatings C1 – C6.

In the case of coating C1, an initial period of higher friction coefficient is observed. This period is referred to as “run-in period” and the part of the tribological curve that represents it is shown magnified in the insert of Figure 9.12. Such a behaviour was observed by Gilmore [7] for TiN+MoS_x coatings. The lubrication in amorphous MoS_x-based coating is provided via mechanically-induced formation and/or reorientation of 2H MoS_x in the contact zone [22]. While this process is very fast in amorphous MoS_x-based coatings, it is apparently slower in coating C1 where no amorphous MoS_x-containing phase is present. Crystallisation of 2H MoS_x in the contact zone is the only step that an amorphous MoS_x-based coating needs to pass in order to provide solid lubrication. In contrast, in coating 1 the MoS_x needs first to be leached out from the fcc TiN-based solid solution at the contact zone and then to crystallise. The process of leaching apparently takes some time (during which the run-

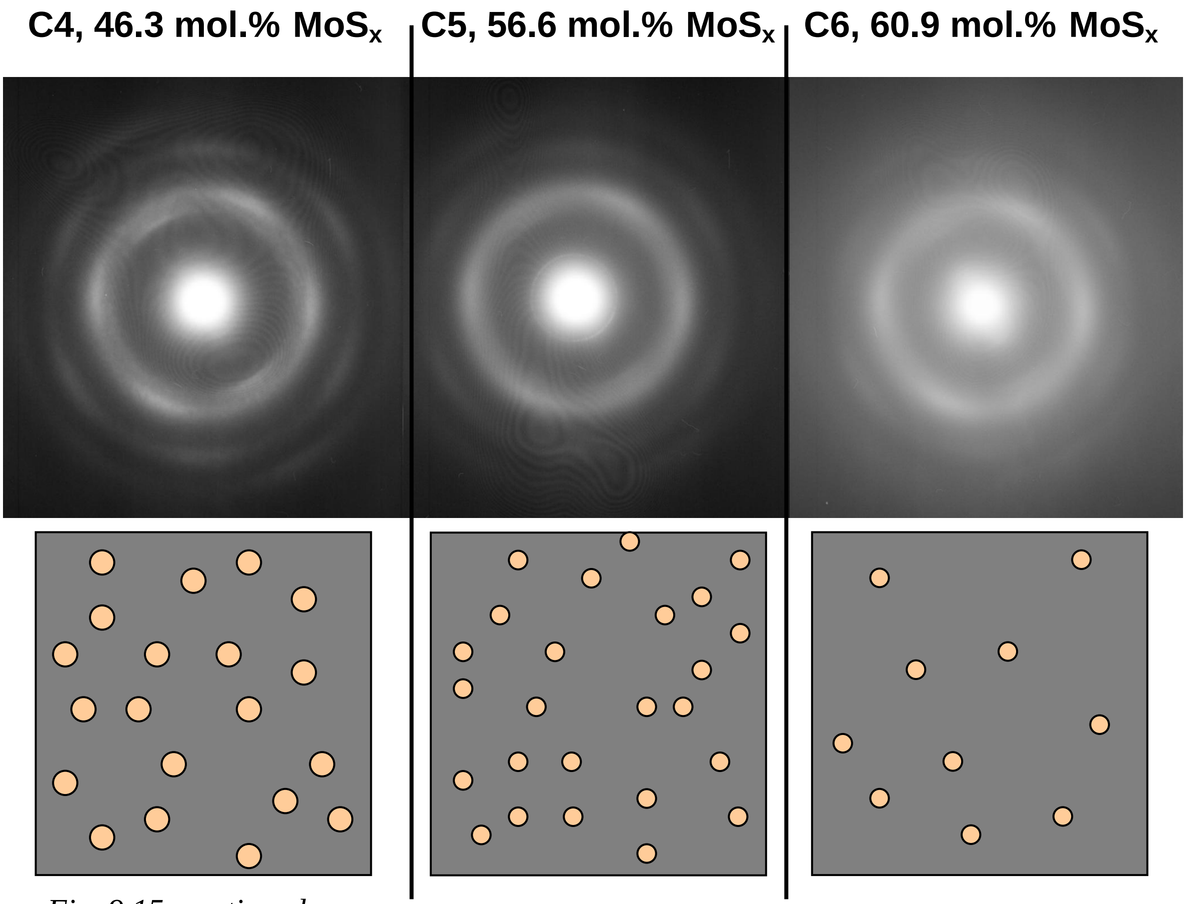

Fig. 9.15. continued

in period is observed) and its mechanism is not understood. In all the other 5 coatings amorphous phase exists and therefore no run-in period is observed. Another factor that can potentially affect the duration of the run-in period is the formation of a transfer layer on the Al_2O_3 counterpart. Being the hardest one, coating C1 would yield such a transfer layer slower than coatings C1 - C5. However, the influence of this phenomenon on the existence of a run-in period in coating C1 is unlikely since the difference in hardness between coatings C1 and C2 is only approximately 10%. Hence it is logical to predict that some run-in period will still be observed in coating C2, which is not the case. Surface roughness can strongly influence the presence and duration of a run-in period as reported in [23]. This factor, however, can also be excluded since the surface roughness of all coatings was measured to be less than R_a=0.01. Two additional POD tests were carried out with coating C1 in humid air. In the first, the test was stopped after 1000 laps which is just after the end of the run-in period. In the second, the test was extended to 10000 laps. In all tree tests (1000, 5000 and 10000 laps) the wear track of the coating had almost the same cross section area being 10.2, 10.7 and 11.7 μm^2, respectively. This is a clear indication that most wear takes place during the run-in period. Surprisingly, coating C2 shows higher friction coefficient than coating C1. For this reason the deposition was repeated. The tribilogical curve of the second coating was very similar to that of the first one. So far the author has not found explanation for this “anomalous” tribological behavior. The tribological behaviour of coatings C3 - C6 including the benchmark MoS_x-Ti coating are very similar as seen from the tribological curves. Therefore, no distinction between them is made on the graph.

9.6. Conclusions

Incorporation of small amount of MoS_x (up to 17.5 %. mol in the reported series of depositions) in a TiN coating by co-sputtering does not promote the appearance of amorphous phase in the structure of the coating. Practically all MoS_x is dissolved in the fcc lattice of the TiN. Hence, the structure can be referred to as an fcc TiN-based (Ti, Mo)(N, S) solid solution. The resulting coating retains the high hardness and good adhesion of the TiN while it exhibits low friction coefficient in both humid air, being an order of magnitude lower than that of the pure TiN benchmark and only two times higher than that of a typical MoS_x-Ti solid lubricant. The wear resistance of the TiN-MoS_x coating is an order of magnitude higher than that of the pure TiN benchmark coating. Higher MoS_x concentrations promote the formation of amorphous phase with fcc (Ti, Mo)(N, S) crystallites dispersed in it. The size of the crystallites decreases and the amount of the amorphous phase increases with increasing MoS_x concentration in the coating. The hardness and cohesion follow the same trend while the wear rate remains almost constant. No decrease in adhesion compared to the TiN benchmark was found. The excellent tribological performance of all the MoS_x-containing coatings C1 - C6 in humid air suggests that they can be successfully used as wear protective coatings in a very wide range of environments.

Reference List to Section 9

1. Maillat, M. **1985** Ch. 1-3.4.

2. Bae, Y. W., Lee, W. Y., Besmann, T. M., Blau, P. J., More, K. L., and Braski, D. N. *Chemical Vapor Deposition of Refractory Metals and Ceramics III. Symposium* **1995** 231-236

3. Bae, Y. W., Lee, W. Y., Besmann, T. M., Yust, C. S., and Blau, P. J. *Materials Science & Engineering A (Structural Materials: Properties, Microstructure and Processing)* A209 1-2 **1996** 369-373

4. Bae, Y. W., Lee, W. Y., Yust, C. S., Blau, P. J., and Besmann, T. M. *Journal of the American Ceramic Society* 79 4 **1996** 819-824

5. Lee, W. Y. *Proceedings of the Thirteenth International Conference on Chemical Vapor Deposition* **1996** 629-636

6. Gilmore, R., Baker, M. A., Gibson, P. N., and Gissler, W. *Surface and Coatings Technology* 105 1-2 **1998** 45-50

7. Gilmore, R., Baker, M. A., Gibson, P. N., Gissler, W., Stoiber, M., Losbichler, P., and Mitterer, C. *Surface and Coatings Technology* 108-109 1-3 **1998** 345-351

8. Goller, R., Torri, P., Baker, M. A., Gilmore, R., and Gissler, W. *Surface and Coatings Technology* 120-121 **1999** 453-457

9. Heinisch, C., Piplits, K., Kubel, F., Schintlmeister, A., Pfluger, E., and Hutter, H. *Applied Surface Science* 179 1-4 **2001** 269-274

10. Spassov, V., Savan, A., Phani, A. R., Stueber, M., and Haefke, H. *Continuous Nanophase and Nanostructured Materials Symposium (Mater. Res. Soc. Symposium Proceedings Vol. 788)* **2004** 309-314

11. Audronis, M., Kelly, P., Arnell, R., Leyland, A., and Matthews, A. *Surface and Coatings Technology* 200 **2005** 1616-1623

12. Haider, J., Rahman, M., Corcoran, B., and Hashmi, M. S. J. *Surface and Coatings Technology* 200 **2005** 1080-1083

13. Rahman, M., Haider, J., Dowling, D. P., Duggan, P., and Hashmi, M. S. J. *Surface and Coatings Technology* 200 **2005** 1071-1075

14. Xing-zhao, Ding, Zeng, X. T., and Goto, T. *Surface and Coatings Technology* 198 **2005** 432-436

15. Cosemans, P., Zhu, X., Celis, J. P., and Van Stappen, M. *Surface and Coatings Technology* 174-175 **2003** 416-420

16. Efeoglu, I. *Surface and Coatings Technology* 200 **2005** 1724-1730

17. Thornton, J. *Annual Review for Materials Science* **1977** 239-260

18. Fox, V., Renevier, N., Teer, D., Hampshire, J., and Rigato, V. *Surface and Coatings Technology* 116-119 **1999** 492-497

19. Nossa, A. and Cavaleiro, A. *Surface and Coatings Technology* 142-144 984 **2001** 991

20. Nossa, A. and Cavaleiro, A. *Surface and Coatings Technology* 163-164 **2003** 552-560

21. Nossa, A. and Cavaleiro, A. *Journal of Materials Research* 19 8 **2004** 2356-2365

22. Moser, J. and Levy, F. *Journal of Materials Research* 8 1 **1993** 206-213

23. de Barros, M., Vandenbulcke, L., Fontaine, J., Farges, G., Vayer, M., and Erre, R. *Surface and Coatings Technology* 127 2-3 **2000** 193-202

Section 10. Concluding remarks and recommendations for further studies

10.1. Concluding remarks

In this work, the possibility for combining a hard wear resistant coating with a solid lubricant was studied. As a result, a coating that combines the high hardness and wear resistance of the hard phase and the low friction coefficient of the solid lubricant is expected to be deposited, denoted as a self-lubricating hard coating. For the scope of this work TiN was chosen as a hard phase and MoS_2 was chosen as a solid lubricant. Two possible architectures of the self-lubricating hard coating were explored: a multilayer structure where a number of alternating hard phase and solid lubricant layers are deposited one after another and co-deposited coatings where the hard phase and the solid lubricant were deposited simultaneously. The tribological and mechanical properties of these coating architectures were compared with these of a TiN and MoS_x-Ti benchmark coatings. The conclusions from the investigation of the structural, mechanical and tribological properties of the self-lubricating hard coatings are as follows:

- Multilayer structures have poor cohesive strength due to the low shear strength of the solid lubricant layers and/or their insufficient adhesion to the TiN layers. Such structures are advised not to be used for tribological applications.
- The structure of the co-deposited coatings consists of fcc crystals of (Ti,Mo)(N,S) metastable solid solution. At low MoS_x content (17.5 mol.%) the crystals form columns and no amorphous phase is identified. With increasing MoS_x content the columns break into fcc (Ti,Mo)(N,S) metastable solid solution crystals embedded in an amorphous matrix. The size of the crystals decreases and the amount of the amorphous phase increases with increasing MoS_x content which is related to the saturation of the fcc (Ti,Mo)(N,S) solid solution in MoS_x. Co-deposited coatings have friction coefficients depending on their MoS_x content. In all cases their friction coefficients are much lower than that of the TiN benchmark and in most cases are very close to that of the MoS_x-Ti benchmark. At the same time their wear coefficients are also much lower than that of the TiN benchmark, in some case over an order of magnitude. The addition of MoS_x to the TiN hard phase was not found to have any detrimental effect on the adhesion of the coatings to the substrate. The cohesive strength of the coatings was found to decrease with the increasing MoS_x content. The same trend was observed for the hardness of the

coatings. However, no decrease in either cohesive strength or hardness compared to that of the TiN benchmark was observed for small MoS_x content (17.5 mol.%). At this case, however, both friction coefficient and wear coefficient are an order of magnitude lower than these of the TiN benchmark. Thus the concept was proved and the goal of this work was fulfilled.

10.2. Recommendations for further studies

Once the concept has been proved, there is a lot of room for further optimization and studies of the self-lubricating hard coatings in the system TiN-MoS_x. The following scheme can be proposed in this field:

- Study of the influence of temperature on the structure and properties of the coatings
- Broadening the range of chemical complexity of the coatings by including Al and C in the structure to obtain (Ti,Al)(N,C)-MoS_x coatings
- Investigation of the tribological behavior in vacuum and at elevated temperatures
- Investigation of the chemical resistance of the coatings in aggressive media and at high temperature in air.

Table of contents